2005

This is to certify that the
dissertation entitled

APPLICATION OF THE WAVEFIELD TRANSFORM TO
NONDESTRUCTIVE EVALUATION

presented by

YONG TIAN

has been accepted towards fulfillment
of the requirements for the

Doctoral degree in Electrical Engineering

Satish Udpa, Antonello Tamburrino
Major Professor's Signature

May 11, 2005
Date

APPLICATIONS OF THE WAVEFIELD TRANSFORM TO NONDESTRUCTIVE EVALUATION

By

Yong Tian

A DISSERTATION

Submitted to
Michigan State University
in partial fulfillment of the requirements
for the degree of

DOCTOR OF PHILOSOPHY

Department of Electrical and Computer Engineering

2005

ABSTRACT

APPLICATIONS OF THE WAVEFIELD TRANSFORM TO NONDESTRUCTIVE EVALUATION

By

Yong Tian

Eddy current nondestructive techniques offer many attractive benefits such as reduced inspection time, low cost and reproducibility. Nevertheless, they are not used in many industrial applications, primarily due to the difficulty associated with the lack of simple and physically meaningful interpretation techniques. In contrast, wave propagation phenomena based non-destructive evaluation (NDE) techniques employ a host of physical intuitive concepts, among which a prominent one is time-of-flight (TOF), i.e. the time duration between the excitation pulse and its response. TOF not only provides position and other information relating to the flaw in an "explicit" way, but also enables the use of mapping algorithms based on wave propagation. There is thus a clear need to study means in which techniques for analyzing wave propagation based NDE data can be applied to eddy current testing (ECT) data. This research aims at inverting ECT data from the perspective of wave propagation phenomena and presenting the inversion results in the same format as that obtained from wave propagation based testings, thereby facilitating possible future data fusion processes.

Towards this goal, it is necessary to obtain a comprehensive understanding of the distinct physical characteristics, incompatible test data formats, and different mathematical tools required for analysis and data processing. To this end, we employ a

wavefield transform, also called the Q-transform, a mapping relating wave fields to diffusive fields, to retrieve TOF information from ECT data. In this research, the TOF information is extracted directly from ECT data. Thus, we overcome the instability associated with numerical inversion of the Q-transform, which is widely adopted in traditional Q-transform based TOF extraction methods. In order to demonstrate the effectiveness of the proposed Q-transform approach, we estimate the TOF for a host of canonical examples, in both the time and frequency domain. In addition to demonstrating the merit of these models through numerical simulations, an experimental set-up was built for validating the concept. The measured data shows excellent agreement with theoretical predictions. The experimental data was also used to estimate the source position successfully.

The Q-transform based TOF extraction methods presented in this work demonstrates the potential for retrieving the TOF information from test objects with complex geometries. The extracted TOF data possesses the same format as that measured from wave propagation based NDE techniques. This makes it possible to fuse these measurements together for improving inspection accuracy and reliability. In a broader context, the successful development of the Q-transform approach may inspire and encourage future research on methods for addressing ECT conductivity imaging problems.

To my parents, sister and wife.

ACKNOWLEDGMENTS

Foremost, I would like to express my gratitude to my major advisor, Dr. Satish Udpa, for his consistent support in the past few years. He offered not only his keen insight and guidance in my research area, but also his generous encouragement. I have no doubt that I wouldn't reach this point without his help. I would like to thank Dr. Antonello Tamburrino, who also has been my major advisor, for his great contribution to this study. His guidance and inspiration have been a key source of motivation. I would like to thank all my committee members, Dr. Richard C. York, Dr. Lalita Udpa, Dr. Shanker Balasubramaniam, Dr. Leo Kempel and Dr. Edward Rothwell for taking the time to serve on my committee and for providing invaluable comments and suggestions to enhance the quality of this dissertation.

I am grateful to my colleagues. Mr. Naveen Nair contributed to both my theoretical and experimental work in the final stage of this work, Mr. Robert Clifford, Mr. Michael Chan and Mr. Brian Wright provided significant support for my experimental work.

TABLE OF CONTENTS

LIST OF TABLES

LIST OF FIGURES

CHAPTER 1

INTRODUCTION

1.1 Nondestructive Evaluation

NDE techniques are used very widely in a number of industrial areas to control product quality, identify component failures, monitor manufacturing processes, etc. A key aspect of NDE lies in the fact that inspections are performed in a manner that does not affect the future usefulness of the object or material. As such, NDE provides balance between quality control and cost effectiveness. Some of the major applications can be found in aerospace industry, gas transmission pipeline industry and nuclear power plants, where the detection of defects prior to device failure often translates to enormous savings in terms of both economical costs and human lives.

A NDE technique usually introduces some form of physical energy, such as X-rays, elastic waves, or electromagnetic fields, into the test specimen. The nature of the interaction between the energy and the test specimen is a function of several variables, including the energy type, material properties, defects and inhomogeneities in the material and so on. The interaction is sampled through a transducer and the response of the transducer is analyzed to characterize the material properties of the specimen. As shown in Figure 1.1, a typical NDE system employs an input transducer with an excitation source to expose the test specimen to the physical field. The response of the test object is then sampled by a measurement transducer and passed on to a computing unit for signal/image processing, recognition, and fusion. Common NDT techniques include radiography testing (RT), ultrasonic testing (UT),

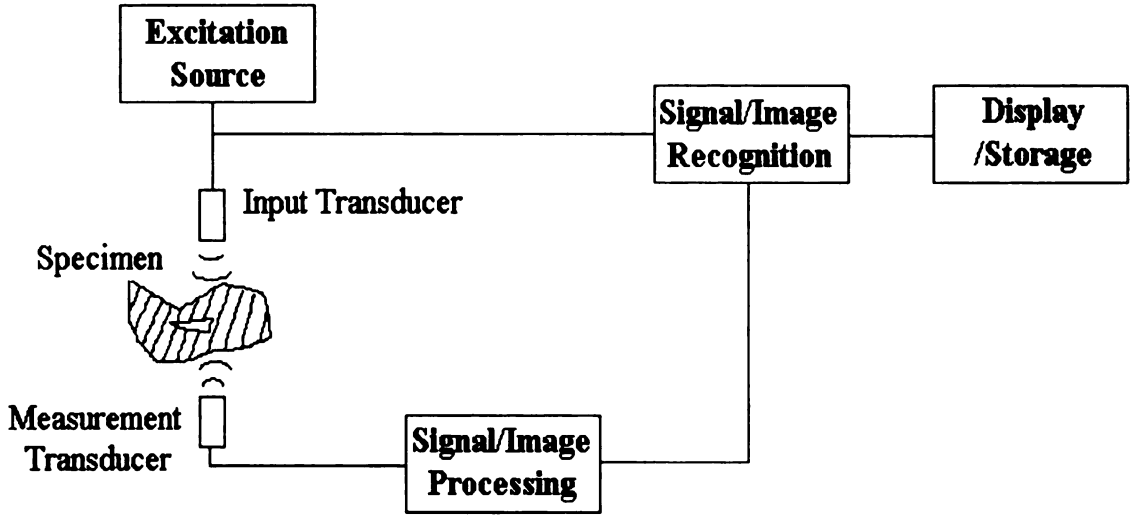

Figure 1.1: A typical NDE system

electromagnetic testing (ET) and acoustic emission testing (AE) [1].

Since a single technique may not be capable of providing all the necessary NDE information, the idea of judiciously combining measurements from multiple NDE techniques, or from the same kind of sensors with different parameters has been proposed as a means for garnering additional information [2]. We can benefit from the enlarged pool of complementary information regarding the test specimen, thus offering great improvement in the detectability and reliability of NDE inspections. For example, in ECT testing, fields from eddy current probes are limited to the surface of a conductive specimen. For a given set of material parameters, the depth of energy penetration is inversely proportional to the square root of the excitation frequency used. We employ low excitation frequencies for detecting deep flaws. Shallow flaws can be detected with greater sensitivity by using a high excitation frequency. If shallow as well as deep flaws are to be detected, it may be necessary to employ a wide

range of frequencies. The complexity and cost of such multi-mode NDE inspections can be substantially reduced with advances in automated data fusion tools [3].

1.2 Eddy Current Testing and Time-of-Flight

ECT is an important NDE technique employing low-frequency electromagnetic fields where the magnetoquasi-static approximation holds, i.e., the displacement current is negligible. Therefore, the governing Maxwell's equations are in the form of vector diffusion equations.

ECT applications find widespread adoption in industry. ECT provides nearly instantaneous measurements with great reproducibility for metallic materials. Moreover, modern ECT offers a low-cost method for high-speed and large-scale inspections, even in extreme environmental situations, such as under high pressure and in high temperature conditions.

The basic idea underlying ECT is to use a time varying magnetic field (excitation source) to induce electrical currents in the conductive test sample. The induced currents, known as eddy currents, generate a time varying magnetic field which interacts with the original field. According to Lenz's law, the magnetic field generated by eddy currents always opposes a change in the net magnetic flux. The intensity of the eddy current reaches its largest value at the surface of the specimen and decays exponentially with the depth below the surface, giving rise to the so-called skin effect. This effect constrains the usage of ECT to surface or subsurface inspections. Eddy current techniques are sensitive to magnetic permeability and geometric properties of the specimen.

The excitation sources (typically coils) associated with conventional ECT systems are time harmonic in nature. The measurement employs sensors which are usually either coils or magnetic field transducers. In swept-frequency eddy current (SFEC) testing, a number of different frequencies are used to excite the probing coil. Since the diffusion of the eddy currents into metals is governed by the skin effect, the responses at different frequencies reflect the internal structure at different depths. Therefore, SFEC can be used to obtain the "depth profile" of the specimen. Another prominent form of ECT is pulsed eddy current (PEC) testing, which is a time-domain method that uses a step-function as the excitation signal. Compared with other methods, the PEC method offers the potential advantages of greater penetration and also serves as a ready means of multi-frequency measurement.

When wave propagation NDE methods are used, the term time-of-flight (TOF) refers to the time interval between the transmission of an excitation pulse and the arrival of its echo. In ultrasonic testing, for example, the TOF is used as a basis for locating the scatterer. Based on the knowledge of TOF, it is possible to determine the location of the defects and generate reflectivity images about the subsurface structure of the specimen. The TOF measuring techniques also offer intuitive physical interpretation of the measured data and are simple to implement.

Unfortunately, TOF measurements are not physically meaningful in the case of methods that generate a diffusive field, such as ECT [4], since no definition of pulse travel-time and no concepts of wave propagation exist therein. Alternatively, the size and location information of the defects are often obtained through complex decision-

making algorithms (such as so-called model-based methods) for ECT measurements. For the same reason, well-developed ultrasonic imaging methods cannot be employed for analyzing ECT data. This suggests that one stands to benefit by exploring the possibility of extracting information such as TOF that are traditionally associated with wave propagation based NDE methods from diffusion based (such as eddy current) NDE methods.

1.3 Preliminaries

This work aims at developing time-of-flight extraction methods from eddy current measurements. The fundamental mathematical tool exploited in this research is the wavefield transform, which is an integral operator that is capable of transforming solutions of wave equation problems to solutions of diffusion equation problems. The wavefield transform [5] is also called the Q-transform [6], or diffusion-to-wave transform [7]. For the sake of simplicity, we choose to call it the Q-transform throughout this work.

Suppose $v(\mathbf{x}, t)$ is the solution of the diffusion equation [8, 9]:

$$\nabla^2 v(\mathbf{x}, t) - c(\mathbf{x})\, \partial_t v(\mathbf{x}, t) = F(\mathbf{x}, t) \quad \text{in } \Omega, \text{ for } t \geq 0 \tag{1.1}$$

$$\alpha(\mathbf{x})\, v(\mathbf{x}, t) + \beta(\mathbf{x})\, \partial_n v(\mathbf{x}, t) = G(\mathbf{x}, t) \quad \text{on } \partial\Omega, \text{ for } t \geq 0 \tag{1.2}$$

$$v(\mathbf{x}, 0) = h(\mathbf{x}) \quad \text{in } \Omega \tag{1.3}$$

and $u(\mathbf{x}, q)$ is the solution of the wave equation:

$$\nabla^2 u(\mathbf{x}, q) - c(\mathbf{x})\, \partial_{qq} u(\mathbf{x}, q) = f(\mathbf{x}, q) \quad \text{in } \Omega, \text{ for } q \geq 0 \tag{1.4}$$

$$\alpha(\mathbf{x})\, u(\mathbf{x}, q) + \beta(\mathbf{x})\, \partial_n u(\mathbf{x}, q) = g(\mathbf{x}, q) \quad \text{on } \partial\Omega, \text{ for } q \geq 0 \tag{1.5}$$

$$u(\mathbf{x}, 0) = 0 \quad \text{in } \Omega \tag{1.6}$$

$$\partial_q u(\mathbf{x}, 0) = h(\mathbf{x}) \quad \text{in } \Omega, \tag{1.7}$$

where $\mathbf{x}$ is a spatial variable, Ω is the domain of $\Re^N$ $(N \geq 1)$ with a smooth boundary $\partial\Omega$, $c(\mathbf{x})$ is a real and nonnegative function depending on the material properties, ∂_n denotes the normal derivative on $\partial\Omega$, and α and β are two known scalar functions. The Q-transform operator, denoted by $\mathcal{Q}$, is defined as [6, 8, 9, 10]:

$$\mathcal{Q} : u(\mathbf{x}, q) \to v(\mathbf{x}, t) \equiv \frac{1}{2\sqrt{\pi t^3}} \int_0^{+\infty} q \exp\left(-\frac{q^2}{4t}\right) u(\mathbf{x}, q)\, dq. \tag{1.8}$$

One can show that

$$v(\mathbf{x}, t) = \mathcal{Q}\{u(\mathbf{x}, q)\}(t) \tag{1.9}$$

provided that

$$F(\mathbf{x}, t) = \mathcal{Q}\{f(\mathbf{x}, q)\}(t) \text{ and } G(\mathbf{x}, t) = \mathcal{Q}\{g(\mathbf{x}, q)\}(t).$$

It is evident from (1.8) that the Q-transform serves a bridge between the wave phenomenon $u(\mathbf{x}, q)$ and the diffusion phenomenon $v(\mathbf{x}, t)$. Taking Fourier transform on both sides of Eq. (1.8) [11], we obtained the Q-transform in the frequency (ω)

domain:

$$\mathcal{FQ} : u(\mathbf{x}, q) \rightarrow V(\omega) \equiv \int_0^{+\infty} \exp\left(-\sqrt{j\omega q}\right) u(\mathbf{x}, q)\, dq \tag{1.10}$$

With the help of Q-transform, we will demonstrate that the time-of-flight can be calculated from diffusive fields. In another words, measurements of the diffusive field established by the eddy current probe can be interpreted from the perspective of wave propagation phenomena.

The major benefits we stand to accrue include:

- Interpretation of ECT data in a clear and intuitive manner.
- Ability to estimate TOF from diffusive field measurements that correspond to those that are typically obtained from wave propagation based NDE techniques, for data fusion.
- Ability to apply a wide variety of image reconstruction techniques that are typically applied to wave propagation measurements.

In this work, the basic strategy of extracting the time-of-flight from transient ECT measurements is described:

- With respect to every diffusive field $v(\mathbf{x}, t)$ of interest, a fictitious wave field $u(\mathbf{x}, q)$ is established analytically using the Q-transform.
- Although the time-of-flight term appears explicitly in the fictitious wave field, we wish to associate the TOF with certain distinct features of the time domain response. To this end, manipulations of the form of excitation signal are carefully investigated.

- Parametric forms of diffusive field responses containing the TOF information, are derived by transforming the fictitious wave response using Q-transform, which, unlike inverse Q-transform, is not ill-posed. Extraction methods are then developed to recover the TOF that is treated as a parameter.

In case of harmonic fields, material discontinuities could significantly increase the complexity of the TOF retrieval process. To overcome this difficulty, a two-step procedure is followed:

- A linear filter is constructed to transform the field in presence of material discontinuities to a field excited in an infinite homogeneous background medium. This filter is typically independent of the nature of the excitation source.

- Based on knowledge of the field inside a homogeneous background, which is much easier to handle with than fields resulting from the presence of material discontinuities, we describe a technique for retriving TOF information. The TOF information can be fused or combined with equivalent estimates from wave propagation based NDE methods such as ultrasoninc or microwave nondestructive testing techniques to improve the TOF estimate. This is an example of a phenomenological approach to data fusion.

1.4 Literature Review

NDE techniques are governed by different partial differential equations. It is important to recognize the mathematical connections among these partial differential equations [10]. In particular, the linkage between hyperbolic and parabolic equations,

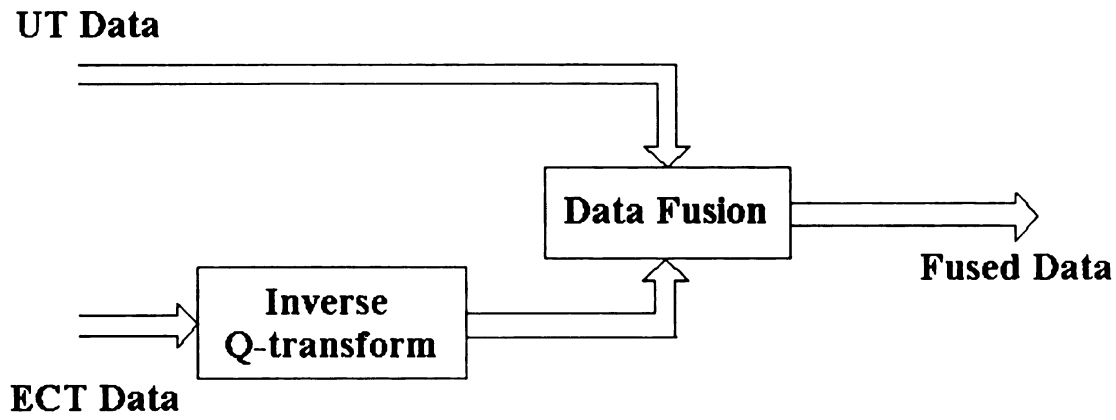

Figure 1.2: Data fusion approach using the Q-transform

i.e. wave propagation and diffusion equations, is of special interest here. Bragg and Dettman [8, 9, 12, 13] were among the earliest to build these connections through the Laplace transform. Other mathematical works addressing this issue were pursued by Reznitskaya [14], Lavrent'ev [15] and Romanov [10]. Specifically, they developed an integral transformation, that are called Q-transform later [6], that are capable of mapping solutions of hyperbolic problems into solutions of parabolic problems.

Some authors, encouraged by developments in ultrasonic imaging techniques, such as holographic methods and diffraction tomography methods, have attempted to extend these imaging methods to eddy current testing [17, 18, 19, 20, 21]. A systematic way to treat diffusive measurements by using wave propagation based imaging methods has been made possible through the use of the Q-transform. The underlying idea is to invert the Q-Transform (this requires the solution of a first kind Fredholm integral equation) to cast eddy current data into the framework of a wave propagation problem. The philosophy of this approach is illustrated in Figure 1.2. Such attempts were made for the purpose of analyzing petroleum reservoir exploration

data [22] and magnetotelluric soundings over a stratified earth [23, 24]. The two last references do not make use of the Q-Transform directly but refer to the underlying connection between wave propagation and diffusion equations. The primary obstacle for these methods arises from the ill-posedness of the inversion of the Q-Transform (the Q-transform is a compact operator). This ill-posed problem has been addressed [7, 25, 26] along with a discussion on regularization algorithms.

The Q-transform was extended to vector diffusion problems by Lee et al. [6], where the term Q-transform was coined. Details about how to implement the Q-transform for electromagnetic imaging in conductive media were elaborated by Gershenson [27, 28]. Experimental work was carried out to validate the time domain (diffusive fields) to fictitious wave domain (fictitious wave fields) transform and investigate the constraints on bandwidth and signal-to-noise ratio [29].

Among recent developments, a nonlinear tomographic inversion scheme was applied to reconstruct the two-dimensional spatial distribution of the conductivity starting from the TOF information associated to the fictitious wave propagation data, using the inverse Q-Transform on eddy current measurements [5].

In [26], Gibert and others approximate the frequency domain eddy current response through the Q-Transform. Specifically, they postulate that the response for the fictitious field consists mainly of weighted and delayed replica of the driving (fictitious) waveform. Each term in this sequence can be regarded as a reflection, or multiple reflection, from certain discontinuities. Then, they obtain the approximate frequency domain eddy current response by applying the Q-transform to the fictitious wave propagation response. The values of TOF's and weights involved in the

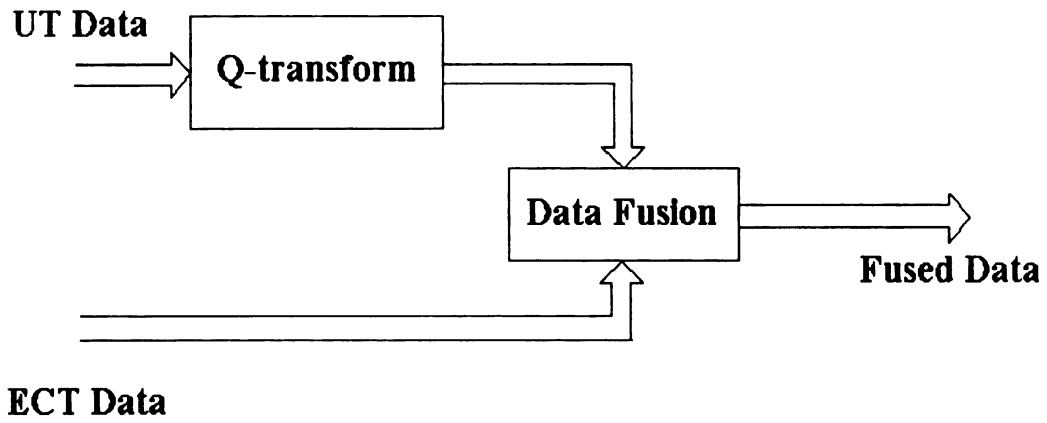

Figure 1.3: Alternative data fusion approach using the Q-transform

approximated response can be estimated numerically from ECT measurements. Levy et al. [30] indicate that this method works well if the desired response is a spike train signal, which is often the case for wave reflection in layered structures.

An alternative is to represent the fictitious wave field either with a ray series or its leading term [31]. The determination of the corresponding coefficients and TOF can be very difficult. When only the leading term is used, the complexity of this parameter estimation problem is reduced but multiple reflections cannot be taken into account.

The Q-transform has also been used in another way to transform ultrasonic measurements into equivalent ECT measurements. This enables one to transform ultrasonic measurements into the ECT format and, therefore, to fuse ultrasonic and ECT measurements from the ECT standpoint as shown in Figure 1.3. A relevant problem that has to be addressed to successfully fuse the data is the so-called registration problem, i.e. a time-shift affecting the ultrasonic data may significantly affect its Q-transform [16].

Several papers summarizing the work done to date have been published. TOF extraction for time-domain fields was proposed in [32, 33]. The corresponding numerical analyses of scalar and vector cases can be found in [34] and [35]. The treatment of interfaces has been developed in [36] and its numerical validation has been presented in [37].

1.5 Organization of This Work

This dissertation is organized into seven chapters.

Chapter 1, introduces the concept of nondestructive evaluation. The physics underlying ECT techniques and diffusion phenomena is discussed. After a brief description of the time-of-flight and Q-transform concepts, the basic strategy proposed for solving the ECT inverse problem (TOF extraction) using mathematical connections between diffusion and wave propagation phenomena are presented. A short literature review is also included in the chapter.

Chapter 2, summarizes the basics of electromagnetic fields. The eddy current formulation based on magnetic vector potential $\bar{A}$ and electric scalar potential V is presented. The fundamentals of the finite element method are also described.

In Chapter 3, the definition of the Q-transform is introduced through detailed derivations for both the scalar and vector cases. Important mathematical properties are presented and numerical implementations for computing the transform are discussed.

In Chapter 4, the constraints associated with (fictitious) wave front recovery in the time domain are introduced. These constraints are then taken into consideration

for designing appropriate excitation waveforms for eddy current testing. The TOF information is extracted afterwards by measuring special features of the received signals, such as the position of the peak value. This strategy is demonstrated through an example involving localization of a small anomaly embedded in an unbounded homogeneous medium. The scalar diffusive case is investigated first for its theoretical simplicity and significance. The investigation strategy is then extended to the vector diffusive case. The approach is validated using data from numerical models simulating some simple test geometries. The results obtained reveal good agreement with the theoretical predictions.

In Chapter 5, the problem of material interfaces is treated. A cylindrical structure is presented as an illustrative example. To remove the effect of multi-reflection on the material interfaces, a stable linear filtering method is developed. The time-of-flight is then extracted by solving a one-dimensional single-parameter minimization problem.

In Chapter 6, the idea of interface removal is adapted to a planar configuration. The corresponding experimental set-up is built and tested. The experimental measurements obtained agree with numerical as well as analytical predictions very well. The measured data is then used successfully to recover the position of point sources.

In Chapter 7, a brief summary is presented.

CHAPTER 2

FUNDAMENTALS OF ELECTROMAGNETIC THEORY AND THE FINITE ELEMENT METHOD

This chapter reviews the basics of electromagnetic theory, including Maxwell's equations as well as a short discussion covering constitutive relations and boundary conditions. Some of the popular potential formulations for eddy current problems are then discussed. The last section focuses on a short introduction to one of the most important numerical techniques, i.e. finite element method (FEM). More detailed discussion on electromagnetic theory, finite element method and computational electromagnetics can be found in references such as [38, 39].

2.1 Basics of Electromagnetic Theory

The problem of electromagnetic analysis on a macroscopic level can be addressed by solving Maxwell's equations, subject to certain boundary and interface conditions. Various scalar and vector potentials can be introduced to reformulate the Maxwell's equation into preferred forms depending on specific applications.

2.1.1 *Maxwell's Equations*

For time-varying electromagnetic (EM) fields, the differential form of Maxwell's equations is given by

$$\nabla \times \mathbf{E}(\mathbf{x},t) = -\frac{\partial \mathbf{B}(\mathbf{x},t)}{\partial t} \tag{2.1}$$

$$\nabla \times \mathbf{H}(\mathbf{x},t) = \mathbf{J}(\mathbf{x},t) + \frac{\partial \mathbf{D}(\mathbf{x},t)}{\partial t} \tag{2.2}$$

$$\nabla \cdot \mathbf{D}(\mathbf{x},t) = \rho(\mathbf{x},t) \tag{2.3}$$

$$\nabla \cdot \mathbf{B}(\mathbf{x},t) = 0, \tag{2.4}$$

where $\mathbf{E}$ ($volts/meter$) is the electric field intensity, $\mathbf{H}$ ($amperes/meter$) is the magnetic field intensity, $\mathbf{D}$ ($coulombs/meter^2$) is the electric flux density, $\mathbf{B}$ ($Tesla$ or $webers/meter^2$) is the magnetic flux density, $\mathbf{J}$ ($amperes/meter^2$) is the electric current density, ρ ($coulombs/meter^3$) is the electric charge density and $\mathbf{x} = \mathbf{x}(x,y,z)$ is the spatial position. Here, Eq. (2.1) and (2.2) are referred to as Faraday's law and Maxwell-Ampere's law, respectively. At the same time, Eq. (2.3) and (2.4) are two different forms of Gauss's law, i.e. the electric and magnetic form, respectively.

Another fundamental equation, the equation of continuity, can be derived from Eqs. (2.2) and (2.3), which is

$$\nabla \cdot \mathbf{J}(\mathbf{x},t) + \frac{\partial \rho(\mathbf{x},t)}{\partial t} = 0. \tag{2.5}$$

It is indeed a mathematical form of the law of the conservation of charges, which means that the net flow of electric current out of a small volume equals the time rate of decrease in electric charges.

Among the above five fundamental Eqs. (2.1)-(2.5), only three of them are independent. Eq. (2.1)-(2.2) combined with either Eq. (2.3) or (2.5) and proper initial conditions can be used to form an independent system, while others can be derived from this system.

Although we will utilize the differential form of Maxwell's equations in this research, the equivalent integral form of Eqs. (2.1)-(2.4) is worth presenting here for sake of their significance in both analytical and numerical treatments. The equations are

$$\oint_C \mathbf{E}(\mathbf{x},t)\cdot d\mathbf{l} = -\int_S \frac{\partial \mathbf{B}(\mathbf{x},t)}{\partial t}\cdot d\mathbf{S} \tag{2.6}$$

$$\oint_C \mathbf{H}(\mathbf{x},t)\cdot d\mathbf{l} = \int_S \left[\mathbf{J}(\mathbf{x},t)+\frac{\partial \mathbf{D}(\mathbf{x},t)}{\partial t}\right]\cdot d\mathbf{S} \tag{2.7}$$

$$\oint_S \mathbf{D}(\mathbf{x},t)\cdot d\mathbf{S} = \int_V \rho(\mathbf{x},t)\,dv \tag{2.8}$$

$$\oint_S \mathbf{B}(\mathbf{x},t)\cdot d\mathbf{S} = 0. \tag{2.9}$$

Equation (2.6), Faraday's integral law, states that the circulation of the electric field $\mathbf{E}$ around a contour C is determined by the time rate of change of the magnetic flux linking the surface S enclosed by contour C. Equation (2.7), Ampère's integral law requires that the circulation of the magnetic field intensity $\mathbf{H}$ around a closed contour C is equal to the net current passing through the surface S spanning the contour plus the time rate of change of the net displacement flux density $\partial\mathbf{D}/\partial t$ through the surface. Equation (2.8) and (2.9) are called Gauss' integral law of electric flux and magnetic flux, respectively. The first one indicates that the net electric flux crossing a surface S that encloses a volume V is equal to the charge contained in this volume.

The second one states that the total magnetic flux passing through a closed surface is zero, i.e. the magnetic flux is conservative.

2.1.2 Constitutive Relations

Assume the medium is isotropic, linear and nondispersive, the constitutive relations describing the material properties of the medium are usually combined with Maxwell's equations. They are

$$\mathbf{D}(\mathbf{x},t) = \varepsilon(\mathbf{x})\,\mathbf{E}(\mathbf{x},t) \tag{2.10}$$

$$\mathbf{B}(\mathbf{x},t) = \mu(\mathbf{x})\,\mathbf{H}(\mathbf{x},t) \tag{2.11}$$

$$\mathbf{J}(\mathbf{x},t) = \sigma(\mathbf{x})\,\mathbf{E}(\mathbf{x},t), \tag{2.12}$$

where ε $(farads/meter)$ is the electric permittivity of a medium, μ $(henrys/meter)$ is the magnetic permeability and σ $(siemens/meter)$ is the electrical conductivity. In a more general case, i.e. the medium may be anisotropic and nonlinear, these property parameters are tensors while their values depend on the field values.

2.1.3 Boundary Conditions

Maxwell's equations should be satisfied everywhere in space. However, certain boundary conditions are necessary to determine a unique solution for a specific problem.

At interfaces between two media, the following conditions can be derived from the

integral form of Maxwell's equations:

$$\hat{\mathbf{n}} \times (\mathbf{E}_1 - \mathbf{E}_2) = \mathbf{0} \tag{2.13}$$

$$\hat{\mathbf{n}} \cdot (\mathbf{D}_1 - \mathbf{D}_2) = \rho_S \tag{2.14}$$

$$\hat{\mathbf{n}} \times (\mathbf{H}_1 - \mathbf{H}_2) = \mathbf{J}_S \tag{2.15}$$

$$\hat{\mathbf{n}} \cdot (\mathbf{B}_1 - \mathbf{B}_2) = 0, \tag{2.16}$$

where $\hat{\mathbf{n}}$ is defined as the unit vector normal to the interface and pointing from medium 2 to medium 1. This implies that only the tangential component of the electric field intensity $\mathbf{E}$ and the normal component of the magnetic flux density $\mathbf{B}$ are always continuous on inter-material boundaries. The discontinuity of the tangential component of $\mathbf{H}$ and the normal component of $\mathbf{D}$ are characterized by the surface current density $\mathbf{J}_S$ and the surface charge density ρ_S. Meanwhile, only two of these four boundary conditions are independent. One of Eqs. (2.13) and (2.16), together with one of Eqs. (2.14) and (2.15), form a set of two independent conditions.

In addition, the interface condition for the current density is

$$\hat{\mathbf{n}} \cdot (\mathbf{J}_1 - \mathbf{J}_2) = -\partial \rho_S / \partial t. \tag{2.17}$$

2.1.4 Time-Harmonic Fields

In many engineering applications involving only linear materials, it is sufficient to deal with only the steady-state solutions of the EM fields when produced by sinusoidal currents [40, 41]. Such fields are said to be sinusoidally time-varying or time harmonic,

i.e. they vary at a sinusoidal frequency ω. An arbitrary sinusoidal field $\mathbf{F}(\mathbf{x}, t)$ can be expressed as

$$\mathbf{F}(\mathbf{x}, t) = \mathrm{Re}\left[\mathbf{F}_p(\mathbf{x}; j\omega)\exp(j\omega t)\right], \tag{2.18}$$

where $\mathbf{F}_p(\mathbf{x}; j\omega)$ is the phasor form of $\mathbf{F}(\mathbf{x}, t)$ and is in general a complex value, $\mathrm{Re}[\cdot]$ indicates "taking the real part of" the quantity within brackets, and ω is the angular frequency (in rad/s) of the sinusoidal excitation.

Using the phasor representations of the EM quantities and replacing the time derivatives $\partial/\partial t$ by $j\omega$, the Maxwell's equations, in the harmonic case, become

$$\nabla \times \mathbf{E}_p(\mathbf{x}; j\omega) = -j\omega\mathbf{B}_p(\mathbf{x}; j\omega) \tag{2.19}$$

$$\nabla \times \mathbf{H}_p(\mathbf{x}; j\omega) = \mathbf{J}_p(\mathbf{x}; j\omega) + j\omega\mathbf{D}_p(\mathbf{x}; j\omega) \tag{2.20}$$

$$\nabla \cdot \mathbf{D}_p(\mathbf{x}; j\omega) = \rho_p(\mathbf{x}; j\omega) \tag{2.21}$$

$$\nabla \cdot \mathbf{B}_p(\mathbf{x}; j\omega) = 0. \tag{2.22}$$

Also, interface conditions (2.13)-(2.16) are converted to:

$$\hat{\mathbf{n}} \times \left(\mathbf{E}_{1p} - \mathbf{E}_{2p}\right) = \mathbf{0} \tag{2.23}$$

$$\hat{\mathbf{n}} \cdot \left(\mathbf{D}_{1p} - \mathbf{D}_{2p}\right) = \rho_{sp} \tag{2.24}$$

$$\hat{\mathbf{n}} \times \left(\mathbf{H}_{1p} - \mathbf{H}_{2p}\right) = \mathbf{J}_{sp} \tag{2.25}$$

$$\hat{\mathbf{n}} \cdot \left(\mathbf{B}_{1p} - \mathbf{B}_{2p}\right) = 0. \tag{2.26}$$

In the above equations, the time-space dependent Maxwell's equations are reduced to space dependent equations and the differential operations are reduced to alge-

braic operations. Thus, time-harmonic analysis could simplify the solution process significantly.

Furthermore, considering the fact that ω is one element of a whole frequency spectrum, we can represent a nonsinusoidal field in terms of its time-harmonic components, i.e.

$$\mathbf{F}(\mathbf{x},t) = \int_{-\infty}^{\infty} \mathbf{F}_p(\mathbf{x},\omega)\, e^{j\omega t} d\omega. \tag{2.27}$$

Therefore, if a time-harmonic field is known for any frequency ω, the corresponding nonsinusoidal field can be obtained through Fourier analysis. In later sections, we will drop the subscript p when no misunderstanding could occur.

2.1.5 Quasi-Static Approximation

For eddy current NDE, the so-called magneto-quasistatic (MQS) approximation holds. Thus the general electromagnetic wave propagation phenomena represented by the original Maxwell's equations can be simplified.

As can be seen from Eq. (2.2), there exist two kinds of currents: conduction current and displacement current. The conduction current $\mathbf{J}$ is proportional to the electric field intensity, as stated by Ohm's law (2.12). The displacement current $\mathbf{J}_d$ is defined as the time varying rate of electric flux density, i.e.

$$\mathbf{J}_d(\mathbf{x},t) \equiv \frac{\partial \mathbf{D}(\mathbf{x},t)}{\partial t}. \tag{2.28}$$

Under the assumption that the time varying rate is low enough such that $\sigma \gg \omega\varepsilon$, the displacement current can be neglected and the EM field can be obtained by

considering stationary current at every instant. This fact implies that the equation of continuity can be rewritten as

$$\nabla \cdot \mathbf{J}(\mathbf{x}, t) = 0 \tag{2.29}$$

and the time derivative of the electric displacement $\partial \mathbf{D}(\mathbf{x}, t)/\partial t$ can be disregarded in Maxwell-Ampere's law to yield

$$\nabla \times \mathbf{H}(\mathbf{x}, t) = \mathbf{J}(\mathbf{x}, t). \tag{2.30}$$

By neglecting the displacement current, the Maxwell's equations and corresponding constitutive relations can be divided into two sub-systems of equations, i.e. one representing an electrostatic field system

$$\nabla \cdot \mathbf{D}(\mathbf{x}, t) = \rho(\mathbf{x}, t) \tag{2.31}$$

$$\mathbf{D}(\mathbf{x}, t) = \varepsilon(\mathbf{x}) \mathbf{E}(\mathbf{x}, t) \tag{2.32}$$

and the other a magnetodynamic field system [42]

$$\nabla \times \mathbf{H}(\mathbf{x}, t) = \mathbf{J}(\mathbf{x}, t) \tag{2.33}$$

$$\nabla \cdot \mathbf{B}(\mathbf{x}, t) = 0 \tag{2.34}$$

$$\nabla \times \mathbf{E}(\mathbf{x}, t) = -\frac{\partial \mathbf{B}(\mathbf{x}, t)}{\partial t} \tag{2.35}$$

$$\mathbf{B}(\mathbf{x},t) = \mu(\mathbf{x})\,\mathbf{H}(\mathbf{x},t) \tag{2.36}$$

$$\mathbf{J}(\mathbf{x},t) = \sigma(\mathbf{x})\,\mathbf{E}(\mathbf{x},t)\,. \tag{2.37}$$

2.1.6 Potential Functions

It is often helpful to formulate the problems using potential functions. The following two vector identities are frequently applied to define the potential functions. They are

$$\nabla \times \nabla V = 0 \tag{2.38}$$

and

$$\nabla \cdot \nabla \times \mathbf{A} = 0. \tag{2.39}$$

These equalities state that the gradient of an arbitrary scalar function is irrotational and the curl of an arbitrary vector function is solenoidal, provided these functions are sufficiently differentiable. Two useful potential functions are the magnetic vector potential $\mathbf{A}$ and the electric scalar potential V. They are given by the equalities

$$\mathbf{B} = \nabla \times \mathbf{A} \tag{2.40}$$

$$\mathbf{E} = -\frac{\partial \mathbf{A}}{\partial t} - \nabla V, \tag{2.41}$$

which are direct consequences of the magnetic form of Gauss's law and Faraday's law, respectively.

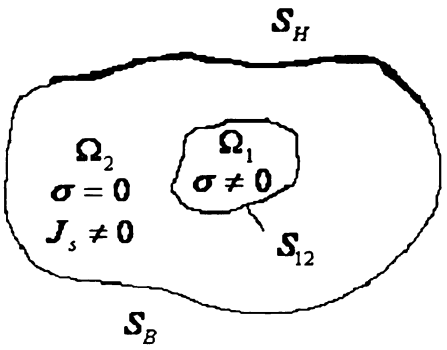

Figure 2.1: A typical solution domain of an eddy current problem

2.2 Potential Formulations for Eddy Current Problems

For eddy current problems, the quasi-static approximation is valid and potential formulations are often introduced to simplify the governing Maxwell's equations and minimize computational costs. For a general three-dimensional eddy current problem shown in Figure 2.1, the solution domain Ω can be divided into a conducting region Ω_1 and a nonconducting region Ω_2, which may include the excitation current source $\mathbf{J}_s$. On the outside boundary S_H, the tangential component of the magnetic field is zero while on the other part of the boundary, S_B, the normal component of the magnetic flux density is zero. Also, we have S_{12} as interface between the conducting region and the nonconducting region.

The Maxwell's equations and corresponding boundary conditions for eddy current

problems can be written as:

$$\nabla \times \mathbf{H} = \sigma \mathbf{E} \quad \text{in } \Omega_1 \tag{2.42}$$

$$\nabla \times \mathbf{E} = -\frac{\partial \mathbf{B}}{\partial t} \quad \text{in } \Omega_1 \tag{2.43}$$

$$\nabla \cdot \mathbf{B} = 0 \quad \text{in } \Omega_1 \tag{2.44}$$

$$\nabla \times \mathbf{H} = \mathbf{J}_S \quad \text{in } \Omega_2 \tag{2.45}$$

$$\nabla \cdot \mathbf{B} = 0 \quad \text{in } \Omega_2 \tag{2.46}$$

$$\mathbf{B} \cdot \hat{\mathbf{n}} = 0 \quad \text{on } S_B \tag{2.47}$$

$$\mathbf{H} \times \hat{\mathbf{n}} = \mathbf{0} \quad \text{on } S_H \tag{2.48}$$

$$\hat{\mathbf{n}} \cdot (\mathbf{B}_1 - \mathbf{B}_2) = 0 \quad \text{on } S_{12} \tag{2.49}$$

$$\hat{\mathbf{n}} \times (\mathbf{H}_1 - \mathbf{H}_2) = \mathbf{0} \quad \text{on } S_{12}, \tag{2.50}$$

where $\hat{\mathbf{n}}$ is the outer normal on the corresponding surface, and the subscript 1 and 2 refer to quantities in the region Ω_1 and Ω_2, respectively.

Providing boundaries S_B and S_H are simply connected, the uniqueness of $\mathbf{B}$ and $\mathbf{E}$ as the solutions of these equations can be proved [43]. There are a number of potential based methods aimed at reformulating the basic Maxwell's equations. Each of them is associated with certain advantages and disadvantages [44]. In this section, Eqs. (2.42)-(2.50) will be reformulated in terms of magnetic vector potential $\mathbf{A}$ and electric scalar potential V.

2.2.1 $\mathbf{A} - V$ Formulation

In $\mathbf{A}-V$ formulation, the magnetic vector potential $\mathbf{A}$ and electric scalar potential V are used to represent the electromagnetic field in the conducting region Ω_1, while in the nonconducting region Ω_2, only $\mathbf{A}$ is used. This method is also referred as $\mathbf{A} - V - \mathbf{A}$ formulation [45].

Invoking Eq. (2.40) and (2.41), Eqs. (2.42) - (2.50) can be expressed as

$$\nabla \times \frac{1}{\mu}\nabla \times \mathbf{A} + \sigma\frac{\partial \mathbf{A}}{\partial t} + \sigma\nabla V = 0 \quad \text{in } \Omega_1 \tag{2.51}$$

$$\nabla \times \left(\frac{1}{\mu}\nabla \times \mathbf{A}\right) = \mathbf{J}_S \quad \text{in } \Omega_2 \tag{2.52}$$

$$\hat{\mathbf{n}} \cdot \nabla \times \mathbf{A} = 0 \quad \text{on } S_B \tag{2.53}$$

$$\frac{1}{\mu}\nabla \times \mathbf{A} \times \hat{\mathbf{n}} = \mathbf{0} \quad \text{on } S_H \tag{2.54}$$

$$\hat{\mathbf{n}} \cdot (\nabla \times \mathbf{A}_1 - \nabla \times \mathbf{A}_2) = 0 \quad \text{on } S_{12} \tag{2.55}$$

$$\left(\frac{1}{\mu_1}\nabla \times \mathbf{A}_1 - \frac{1}{\mu_2}\nabla \times \mathbf{A}_2\right) \times \hat{\mathbf{n}} = \mathbf{0} \quad \text{on } S_{12}. \tag{2.56}$$

Notice that Eq. (2.43), (2.44) and (2.46) are automatic satisfied. Eq. (2.55) is satisfied when $\mathbf{A}$ is continuous across the interface S_{12} [45].

Equation (2.40) specifies the curl of the magnetic vector potential as the magnetic flux density. Helmholtz theorem states that a vector field is uniquely determined when both its curl and divergence are specified. Therefore, the divergence of the magnetic vector potential must be specified to fix the additional degrees of freedom associated with $\mathbf{A}$ (called gauging). This value may be specified freely without affecting the physical problem. In many circumstances, the divergence free condition is imposed,

which is

$$\nabla \cdot \mathbf{A} = 0. \tag{2.57}$$

This is the well-known Coulomb gauge [1]. If we adopt the Coulomb gauge, $\mathbf{A}$ will have a unique solution in a closed region providing the boundary conditions

$$\hat{\mathbf{n}} \times \mathbf{A} = \mathbf{0} \quad \text{on } S_B \tag{2.58}$$

$$\hat{\mathbf{n}} \cdot \mathbf{A} = 0 \quad \text{on } S_H \tag{2.59}$$

are satisfied [47]. Consequently, ∇V is determined uniquely [43]. Eq. (2.53) can be derived from Eq. (2.58).

In order to incorporate the Coulomb gauge, we may add a term $-\nabla\,(1/\mu)\,\nabla \cdot \mathbf{A}$ on the left-side of both Eq. (2.51) and (2.52), which leads to [43, 48]

$$\nabla \times \frac{1}{\mu}\nabla \times \mathbf{A} - \nabla\frac{1}{\mu}\nabla \cdot \mathbf{A} + \sigma\frac{\partial \mathbf{A}}{\partial t} + \sigma\nabla V = 0 \quad \text{in } \Omega_1 \tag{2.60}$$

$$\nabla \times \left(\frac{1}{\mu}\nabla \times \mathbf{A}\right) - \nabla\frac{1}{\mu}\nabla \cdot \mathbf{A} = \mathbf{J}_S \quad \text{in } \Omega_2. \tag{2.61}$$

Now, the equation of continuity (2.29), which is automatically satisfied in Eq. (2.51), no longer holds in (2.60). Hence, it must be enforced explicitly as

$$\nabla \cdot \left(-\sigma\frac{\partial \mathbf{A}}{\partial t} - \sigma\nabla V\right) = 0 \quad \text{in } \Omega_1. \tag{2.62}$$

[1] Other gauges could be used in eddy current problems too, such as the Lorentz gauge [46]

$$\nabla \cdot \mathbf{A} = -\mu\sigma V.$$

Furthermore, we can assume that the media are linear, isotropic and homogeneous. Accordingly, the magnetic permeability is a scalar. And, by using the vector identity

$$\nabla \times \nabla \times \mathbf{A} = \nabla (\nabla \cdot \mathbf{A}) - \nabla^2 \mathbf{A} \tag{2.63}$$

and the Coulomb gauge, we may rewrite Eqs. (2.51) and (2.52) as:

$$-\frac{1}{\mu}\nabla^2 \mathbf{A} + \sigma \frac{\partial \mathbf{A}}{\partial t} + \sigma \nabla V = 0 \quad \text{in } \Omega_1 \tag{2.64}$$

$$-\nabla^2 \mathbf{A} = \mathbf{J}_S \quad \text{in } \Omega_2, \tag{2.65}$$

where $\nabla^2 \equiv \nabla \cdot \nabla$ is the vector Laplacian operator.

The normal component of the current density must be constrained to be zero on the interface S_{12} since eddy currents are restricted to the conducting region only, i.e.

$$\sigma \left(-\frac{\partial \mathbf{A}}{\partial t} - \nabla V \right) \cdot \hat{\mathbf{n}} = 0. \tag{2.66}$$

In addition, the following constraints are added to boundary conditions on S_H and S_B to satisfy the Coulomb gauge [45]:

$$\frac{1}{\mu}\nabla \cdot \mathbf{A} = 0 \quad \text{on } S_B \tag{2.67}$$

$$\left(\frac{1}{\mu}\nabla \times \mathbf{A} \right) \times \hat{\mathbf{n}} = \mathbf{0} \quad \text{on } S_H. \tag{2.68}$$

In summary, the $\mathbf{A} - V$ formulation of eddy current computation can be expressed

as

$$-\frac{1}{\mu}\nabla^2\mathbf{A} + \sigma\frac{\partial\mathbf{A}}{\partial t} + \sigma\nabla V = 0 \quad \text{in } \Omega_1 \tag{2.69}$$

$$\nabla\cdot\sigma\left(\frac{\partial\mathbf{A}}{\partial t} + \nabla V\right) = 0 \quad \text{in } \Omega_1 \tag{2.70}$$

$$\nabla^2\mathbf{A} = \mathbf{J}_S \quad \text{in } \Omega_2 \tag{2.71}$$

$$\hat{\mathbf{n}}\cdot\mathbf{A} = 0 \quad \text{on } S_H \tag{2.72}$$

$$\left(\frac{1}{\mu}\nabla\times\mathbf{A}\right)\times\hat{\mathbf{n}} = \mathbf{0} \quad \text{on } S_H \tag{2.73}$$

$$\hat{\mathbf{n}}\times\mathbf{A} = \mathbf{0} \quad \text{on } S_B \tag{2.74}$$

$$\frac{1}{\mu}\nabla\cdot\mathbf{A} = \mathbf{0} \quad \text{on } S_B \tag{2.75}$$

$$\mathbf{A}_1 = \mathbf{A}_2 \quad \text{on } S_{12} \tag{2.76}$$

$$\frac{1}{\mu_1}\nabla\cdot\mathbf{A}_1 = \frac{1}{\mu_2}\nabla\cdot\mathbf{A}_2 \quad \text{on } S_{12} \tag{2.77}$$

$$\left(\frac{1}{\mu_1}\nabla\times\mathbf{A}_1 - \frac{1}{\mu_2}\nabla\times\mathbf{A}_2\right)\times\hat{\mathbf{n}} = \mathbf{0} \quad \text{on } S_{12} \tag{2.78}$$

$$\sigma\left(-\frac{\partial\mathbf{A}}{\partial t} - \nabla V\right)\cdot\hat{\mathbf{n}} = 0 \quad \text{on } S_{12}. \tag{2.79}$$

With $\mathbf{A}-V$ formulation, the uniqueness of $\mathbf{A}$ and V is guaranteed, which leads to stable numerical solutions for any quasi-static field problem. The handling of internal interface conditions is trivial and applicable to multiply connected conductors. At the same time, the current sources can be incorporated easily. The major drawback lies in the fact that the number of unknowns is high, i.e. four unknowns in conducting region and three unknowns in nonconducting region at each node.

2.2.2 **A** *Formulation*

In order to eliminate the scalar electric potential V in $\mathbf{A} - V$ formulation, we employ the following gauge transformation

$$\mathbf{A} = \mathbf{A}^* + \nabla\Psi \tag{2.80}$$

$$V = V^* - \frac{\partial\Psi}{\partial t}. \tag{2.81}$$

If Ψ satisfies the Laplace equation

$$\nabla^2\Psi = 0, \tag{2.82}$$

Eq. (2.51) and (2.62) hold the same form for $\mathbf{A}^*$ and V^*, which are

$$\nabla \times \frac{1}{\mu}\nabla \times \mathbf{A}^* = -\sigma\frac{\partial \mathbf{A}^*}{\partial t} - \sigma\nabla V^* \tag{2.83}$$

$$\nabla \cdot \left(-\sigma\frac{\partial \mathbf{A}^*}{\partial t} - \sigma\nabla V^*\right) = 0. \tag{2.84}$$

Suppose the function Ψ is defined as

$$\Psi = -\int_{-\infty}^{t} V dt, \tag{2.85}$$

then V^* equals zero. By dropping the $*$ sign, Eqs. (2.69)-(2.71) can be combined to yield

$$\nabla \times \frac{1}{\mu}\nabla\mathbf{A} + \sigma\frac{\partial \mathbf{A}}{\partial t} = \mathbf{J}_S. \tag{2.86}$$

Equation (2.86) holds in both the conducting domain Ω_1 and nonconducting domain Ω_2, and is referred to as the **A** formulation.

We must point out that the electric scalar potential V can be eliminated only if the conductivity is constant everywhere [48]. When regions of different conductivities exist, the introduction of the electric scalar potential is necessary to ensure the continuity of current at the interface of different regions.

2.3 Finite Element Method

Analytical solutions for problems governed by the Maxwell's equations are not available for most engineering applications. Hence, the implementation of numerical methods referred to as computational electromagnetics (CEM) dominate electromagnetic field analysis. Some of popular numerical methods include finite difference (FD) method, boundary element method (BEM), method of moments (MOM) and finite element method (FEM). Although each method has its own advantages and disadvantages, FEM is considered more powerful and flexible in handling problems involving complex geometries and inhomogeneous media [50]. FEM is also regarded as the most widely applied numerical simulation method in various engineering applications and is not limited to electromagnetic field analysis. Moreover, FEM attracts researchers in all fields and a large number of well-developed software packages are currently available. The computer codes developed for one particular discipline can be easily adapted to another discipline. In this section, the basic principles underlining the finite element method are briefly presented.

The basic strategy of FEM is to discretize the solution domain into a finite number

of interconnected subdomains, called elements. The shape and the size of the elements can be selected arbitrarily, which provide superior capabilities in fitting different objects and interfaces. In every element, the solution to be sought is approximated with low-order polynomial functions. For nodal-based FEM methods, this approximation is calculated on the nodes of the elements and is sufficient to approximate the solution on the whole element by interpolating with the basis functions, also called the shape functions. We use the weighted residuals approach or the variational principle to obtain a system of linear equations that are related to the governing differential equations and the applications of proper boundary conditions. Once this linear system of equations, which is typically a sparse, banded, symmetric and positive definite matrix equation, is solved for the interpolation coefficients in each element, the solution is uniquely determined throughout the solution domain. The procedures can be used for solving time-dependent, linear or nonlinear and two-dimensional or three-dimensional problems [51].

2.3.1 Discretization

As mentioned before, the first step in FEM is to divide the solution domain into small elements. A continuous solution domain is thus replaced with a number of subdomains in which the unknown is represented by simple interpolation functions with unknown coefficients. Thus, the solution of the entire system is approximated by a finite number of unknown coefficients to be solved. Typical elements used are triangles and quadrilaterals in two-dimensional case, and tetrahedrons and hexahedrons in three-dimensional case. The element type and the number of elements must be care-

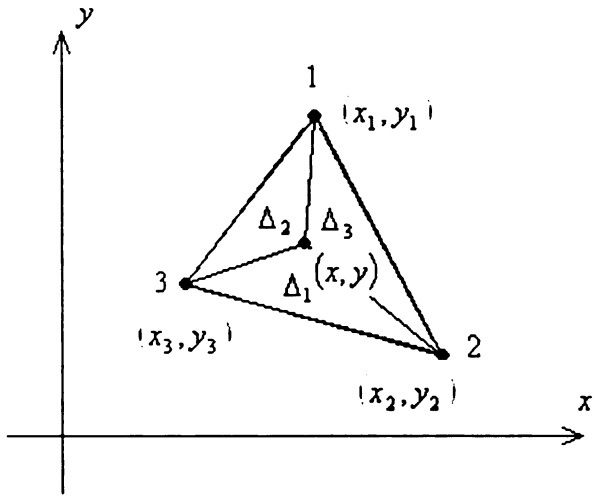

Figure 2.2: A triangular element

fully selected to meet specific requirements on numerical accuracy and computational resources.

Typically, the solution u of the governing differential equation is approximated in the local element with a set of linearly independent polynomial functions , i.e. shape functions. Let us consider a two-dimensional triangular element with vertex coordinates (x_1, y_1), (x_2, y_2) and (x_3, y_3), which are designated as node 1, 2, and 3, respectively (Figure 2.2). Also, the solutions on the nodes 1, 2 and 3 are u_1, u_2 and u_3, respectively. The approximated solution $\tilde{u}(x, y)$ within the element can then be expressed as [51, 52, 53]

$$\begin{aligned} \tilde{u}(x,y) &= \begin{bmatrix} \phi_1(x,y) & \phi_2(x,y) & \phi_3(x,y) \end{bmatrix} \begin{bmatrix} u_1 \\ u_2 \\ u_3 \end{bmatrix} \\ &= u_1\phi_1(x,y) + u_2\phi_2(x,y) + u_3\phi_3(x,y), \end{aligned} \tag{2.87}$$

where $\phi_1(x,y)$, $\phi_2(x,y)$ and $\phi_3(x,y)$ are first order polynomial that satisfy:

$$\phi_i(x_j, y_j) = \delta_{ij}. \tag{2.88}$$

Therefore,

$$\begin{cases} \phi_1(x,y) = \dfrac{\Delta_1}{\Delta} = \dfrac{1}{2\Delta}(a_1 + b_1 x + c_1 y) \\ \phi_2(x,y) = \dfrac{\Delta_2}{\Delta} = \dfrac{1}{2\Delta}(a_2 + b_2 x + c_2 y) \\ \phi_3(x,y) = \dfrac{\Delta_3}{\Delta} = \dfrac{1}{2\Delta}(a_3 + b_3 x + c_3 y) \end{cases}$$

where Δ is the area of the whole element, Δ_1, Δ_2 and Δ_3 are areas of the subordinate triangles as shown in Figure 2.2, respectively. Thus, we have

$$\Delta = \frac{1}{2}\begin{vmatrix} 1 & x_1 & y_1 \\ 1 & x_2 & y_2 \\ 1 & x_3 & y_3 \end{vmatrix}, \quad \Delta_i = \frac{1}{2}\begin{vmatrix} 1 & x & y \\ 1 & x_j & y_j \\ 1 & x_k & y_k \end{vmatrix}$$

and

$$a_i = x_j y_k - x_k y_j, \quad b_i = y_j - y_k, \quad c_i = x_k - x_j \tag{2.89}$$

where (i,j,k) are cyclical permutations of $(1,2,3)$.

For example, if the node coordinates are given by

$$(x_1, y_1) = (0,0), \quad (x_2, y_2) = (1,0), \quad (x_3, y_3) = (1,1),$$

the basis functions become

$$\left\{ \phi_1(x,y) = 1 - x, \quad \phi_2(x,y) = x - y, \quad \phi_3(x,y) = y \right\} \tag{2.90}$$

and

$$\tilde{u}(x,y) = \begin{bmatrix} 1-x & x-y & y \end{bmatrix} \cdot \begin{bmatrix} u_1 \\ u_2 \\ u_3 \end{bmatrix}. \tag{2.91}$$

In general, the unknown solution in an element e can be written as

$$\tilde{u}^e(x,y) = \sum_{k=1}^{n} S_k^e(x,y)\, u_k^e = \{S^e(x,y)\}^T \{u^e\}, \tag{2.92}$$

where n is the number of nodes in the element, u_k^e is the value of u at node k of the element and S_k^e is the interpolation function for node k, which is also known as nodal function or basis function. The superscript T denotes transpose operation. In common, the order N of the element e is defined as the highest order of the functions $S_j^e(x,y)$.

2.3.2 Galerkin's Method

The next step is to formulate the system of equations, which can be done using either the weighted residuals approach or the variational principle. Here, we will adopt one of the weighted residual methods, i.e. the Galerkin's method, due to its simplicity.

Let us consider a general differential equation problem defined in a domain Ω

enclosed by surface $\partial\Omega = \partial\Omega_1 \cup \partial\Omega_2$ with $\partial\Omega_1 \cap \partial\Omega_2 = 0$, which is

$$\mathcal{L}u = f \quad in\ \Omega \tag{2.93}$$

$$u = g \quad on\ \partial\Omega_1 \tag{2.94}$$

$$\frac{\partial u}{\partial \hat{n}} + \alpha u = h \quad on\ \partial\Omega_2, \tag{2.95}$$

where $\mathcal{L}$ is a differential operator up to the second order, f is the source term, u is the unknown field and $\hat{n}$ is the normal vector. Equation (2.94) is known as the Dirichlet boundary condition, or essential boundary condition, which specifies the value of u on surface $\partial\Omega_1$. Equation (2.95) is called the Cauchy boundary condition, or mixed boundary condition, which is a combination of u and its derivative. If $\alpha = 0$, Eq. (2.95) yields the Neumann boundary condition (also named as natural boundary condition)

$$\frac{\partial u}{\partial \hat{n}} = h \quad on\ \partial\Omega_2, \tag{2.96}$$

which depends on the derivative of u only.

For a given approximate solution $\tilde{u}$, the residual R is defined as

$$R = \mathcal{L}\tilde{u} - f. \tag{2.97}$$

We wish to estimate an optimal $\tilde{u}$ by letting the integral of the so-called "weighted residual" to be zero, i.e.

$$R_l = \int_\Omega S_l R d\Omega = 0, \quad l = 1, \ldots, N \tag{2.98}$$

where Ω denotes the whole solution domain and S_l is the l-th nodal function.

Following Jin's formulation [39], we consider a single element, i.e. the eth element. Then, the weighted residual

$$R_l = \sum_{k=1}^{N} R_k^e \tag{2.99}$$

and

$$R_i^e = \int_{\Omega^e} S_i^e \left(\mathcal{L}\tilde{u}^e - f\right) d\Omega \quad i = 1, 2, 3, ..., n, \tag{2.100}$$

where n is the number of nodes in the element. By incorporating Eq. (2.92) into Eq. (2.100), we obtain

$$R_i^e = \int_{\Omega^e} S_i^e \mathcal{L} \left\{S^e\right\}^T d\Omega \left\{u^e\right\} - \int_{\Omega^e} f S_i^e d\Omega \quad i = 1, 2, 3, ..., n, \tag{2.101}$$

or in its matrix form as

$$\left\{R^e\right\} = \left[K^e\right] \left\{u^e\right\} - \left\{b^e\right\}, \tag{2.102}$$

where

$$\left\{R^e\right\} = \left[R_1^e, R_2^e, ..., R_n^e\right]^T \tag{2.103}$$

$$K_{ij}^e = \int_{\Omega^e} S_i^e \mathcal{L} S_j^e d\Omega \tag{2.104}$$

$$b_i^e = \int_{\Omega^e} f S_i^e d\Omega. \tag{2.105}$$

Taking into account Eqs. (2.98) and (2.102)-(2.105), we have

$$\left[\overline{K}\right] \left[\overline{u}\right] = \left[\overline{b}\right], \tag{2.106}$$

where $[\overline{K}]$ is a sparse matrix.

Boundary conditions specified in Eq. (2.94)-(2.95) must be incorporated to guarantee the uniqueness of the solution. In finite element formulations, the natural boundary conditions are automatically satisfied while the implementation of the essential boundary conditions must be imposed explicitly through some modifications to matrix $[\overline{K}]$ and $\{\bar{b}\}$ in Eq. (2.106).

2.3.3 Solution Methods

The matrix Eq. (2.106) derived from the Galerkin's method often involves a very large coefficient matrix $[\overline{K}]$, called the stiffness matrix. $[\overline{K}]$ is not necessarily a symmetric matrix since the operator $\mathcal{L}$ is not required to be self-adjoint. Therefore, methods for solving such a linear equation system must be chosen carefully. Typical solution methods can be classified as either direct solvers or iterative solvers.

Direct solution methods, such as Gaussian elimination and its symmetric variant called Cholesky decomposition (triangular decomposition), lead to accurate solutions of Eq. (2.106) providing the round off errors are negligible. However, storage requirements can be excessive and deter the use of such methods when a large stiffness matrix is involved. The problem could be minimized by choosing a node numbering scheme that results in a highly sparse and banded stiffness matrix, i.e. a great number of the elements of the matrix are zeros and most of the nonzero elements are distributed around the diagonal of the stiffness matrix. Under these conditions, it is possible to use methods [49] that discard all zero elements outside a diagonal band. Thus the storage requirement is significantly reduced.

Iterative solvers including the conjugate-gradient method, over-relaxation method, and so on, are quite efficient with regard to memory usage since all nonzero elements are discarded and the structure of the stiffness matrix does not affect memory requirements. The major concern associated with iterative solvers is in regard to their convergence properties. In principle, the rate of convergence is closely related to the condition number of the stiffness matrix, i.e. the ratio of the highest eigenvalue and the smallest one. Ideally, this ratio should be as close to unity as possible. In order to achieve faster convergence, a preconditioner is usually applied before the final solution step to lower the condition number of the stiffness matrix. Common preconditioners include incomplete LU, diagonal scaling, symmetric successive over-relaxation (SSOR) and so on [39]. The iterative solvers can also be accelerated using the multigrid method and easily implemented in a parallel computing environment.

Some other key factors relevant to the success of FEM implementation include reliable mesh generation, handling open-boundary domains, etc. In addition, a balance between the available computational resources and the accuracy must be achieved.

CHAPTER 3

THE Q-TRANSFORM

In this chapter, the Q-transform will be presented in a scalar form in the first section and extended to vector form in the last section. Some of the more important mathematical properties of the Q-transform are delineated in the second section while numerical implementations of the scalar Q-transform are discussed in the third section.

3.1 Derivations of the Scalar Q-transform

In this section, we focus our attention on the Q-transform in scalar form only. It is worth noting that familiarity with the scalar Q-transform is essential for using the Q-transform for analyzing electromagnetic fields governed by vector equations such as Maxwell's equations. The validation of this statement will be provided in subsequent sections.

Consider the following two initial boundary value problems [10]:

$$\nabla^2 v(\mathbf{x},t) - c(\mathbf{x})\,\partial_t v(\mathbf{x},t) = F(\mathbf{x},t) \quad \text{in } \Omega, \text{ for } t \geq 0 \tag{3.1}$$

$$\alpha(\mathbf{x})\,v(\mathbf{x},t) + \beta(\mathbf{x})\,\partial_n v(\mathbf{x},t) = G(\mathbf{x},t) \quad \text{on } \partial\Omega, \text{ for } t \geq 0 \tag{3.2}$$

$$v(\mathbf{x},0) = h(\mathbf{x}) \quad \text{in } \Omega \tag{3.3}$$

and

$$\nabla^2 u(\mathbf{x},q) - c(\mathbf{x})\,\partial_{qq} u(\mathbf{x},q) = f(\mathbf{x},q) \quad \text{in } \Omega, \text{ for } q \geq 0 \tag{3.4}$$

$$\alpha(\mathbf{x})\,u(\mathbf{x},q) + \beta(\mathbf{x})\,\partial_n u(\mathbf{x},q) = g(\mathbf{x},q) \quad \text{on } \partial\Omega, \text{ for } t \geq 0 \tag{3.5}$$

$$u(\mathbf{x},0) = 0 \quad \text{in } \Omega \tag{3.6}$$

$$\partial_q u(\mathbf{x},0) = h(\mathbf{x}) \quad \text{in}\Omega, \tag{3.7}$$

where $\mathbf{x}$ denotes the spatial variable, $\Omega \in \Re^N$ $(N \geq 1)$ with a smooth boundary $\partial\Omega$, $c(\mathbf{x})$ is a real and nonnegative function, ∂_n denotes the normal derivative on the $\partial\Omega$ and the two scalar functions α, β are known.

To derive the relation between a solution of diffusion equation problem (3.1)-(3.3) and a solution of wave equation problem (3.4)-(3.7), we follow the method presented by Romanov [10]. Taking the Laplace transform[1] of Eqs. (3.1)-(3.3) and Eqs. (3.4)-(3.7) (transforming t to s and from q to p, respectively) and denoting Laplace transformed variables with an over-hat, we have

$$\nabla^2 \hat{v}(\mathbf{x},s) - c(\mathbf{x})\left[s\hat{v}(\mathbf{x},s) - v(\mathbf{x},0)\right] = \hat{F}(\mathbf{x},s) \tag{3.8}$$

$$\alpha(\mathbf{x})\,\hat{v}(\mathbf{x},s) + \beta(\mathbf{x})\,\partial_n \hat{v}(\mathbf{x},s) = \hat{G}(\mathbf{x},s) \tag{3.9}$$

[1]The Laplace transform and the inverse Laplace transform are defined as

$$F(s) \equiv \int_0^\infty f(t)\,\mathrm{e}^{-st}dt \quad \textit{and} \quad f(t) \equiv \frac{1}{2\pi i}\int_{\gamma - j\infty}^{\gamma + j\infty} F(s)\,\mathrm{e}^{st}ds,$$

respectively, where γ is a vertical contour in the complex plane chosen so that all singularities of the $F(s)$ are to the left of the contour.

and

$$\nabla^2 \hat{u}(\mathbf{x},p) - c(\mathbf{x})\left[p^2 \hat{u}(\mathbf{x},p) - pu(\mathbf{x},0) - \partial_q u(\mathbf{x},0)\right] = \hat{f}(\mathbf{x},p) \tag{3.10}$$

$$\alpha(\mathbf{x})\,\hat{u}(\mathbf{x},p) + \beta(\mathbf{x})\,\partial_n \hat{u}(\mathbf{x},p) = \hat{g}(\mathbf{x},p). \tag{3.11}$$

Invoking initial conditions given by Eqs. (3.3) and (3.6)-(3.7), we obtain

$$\nabla^2 \hat{v}(\mathbf{x},s) - c(\mathbf{x})\,s\hat{v}(\mathbf{x},s) + c(\mathbf{x})\,h(\mathbf{x}) = \hat{F}(\mathbf{x},s) \tag{3.12}$$

$$\alpha(\mathbf{x})\,\hat{v}(\mathbf{x},s) + \beta(\mathbf{x})\,\partial_n \hat{v}(\mathbf{x},s) = \hat{G}(\mathbf{x},s) \tag{3.13}$$

and

$$\nabla^2 \hat{u}(\mathbf{x},p) - c(\mathbf{x})\,p^2 \hat{u}(\mathbf{x},p) + c(\mathbf{x})\,h(\mathbf{x}) = \hat{f}(\mathbf{x},p) \tag{3.14}$$

$$\alpha(\mathbf{x})\,\hat{u}(\mathbf{x},p) + \beta(\mathbf{x})\,\partial_n \hat{u}(\mathbf{x},p) = \hat{g}(\mathbf{x},p). \tag{3.15}$$

If we let $s = p^2$ and if $\hat{D}$ is the difference between $\hat{v}(\mathbf{x},p^2)$ and $\hat{u}(\mathbf{x},p)$, we can subtract Eq. (3.12) from Eq. (3.14) to obtain

$$\nabla^2 \hat{D}(\mathbf{x},p) - c(\mathbf{x})\,p^2 \hat{D}(\mathbf{x},p) = 0, \tag{3.16}$$

providing that source terms $\hat{F}(\mathbf{x},p^2)$ and $\hat{f}(\mathbf{x},p)$ satisfy

$$\hat{F}\left(\mathbf{x},p^2\right) = \hat{f}(\mathbf{x},p). \tag{3.17}$$

Similarly, by subtracting Eq. (3.13) from Eq. (3.15), we have

$$\alpha(\mathbf{x})\,\hat{D}(\mathbf{x},p)+\beta(\mathbf{x})\,\partial_n\hat{D}(\mathbf{x},p)=0, \tag{3.18}$$

given that boundary conditions $\hat{G}(\mathbf{x},p^2)$ and $\hat{g}(\mathbf{x},p)$ satisfy

$$\hat{G}\left(\mathbf{x},p^2\right)=\hat{g}(\mathbf{x},p). \tag{3.19}$$

Observing Eq. (3.16), it is clear that $\hat{D}(\mathbf{x},p)$ must equal to zero, or

$$\hat{v}\left(\mathbf{x},p^2\right)=\hat{u}(\mathbf{x},p). \tag{3.20}$$

Equation (3.20) can be further written in an integral form as

$$\int_0^\infty v(\mathbf{x},t)\exp\left(-p^2t\right)dt=\int_0^\infty u(\mathbf{x},q)\exp(-pq)dq. \tag{3.21}$$

Then, if we take the inverse Laplace transform of both sides of Eq. (3.21), with $s=p^2$, we obtain the Q-transform relation from $u(\mathbf{x},q)$ to $v(\mathbf{x},t)$, i.e.

$$v(\mathbf{x},t)=\frac{1}{2\sqrt{\pi t^3}}\int_0^\infty q\exp(-\frac{q^2}{4t})u(\mathbf{x},q)dq, \tag{3.22}$$

which is a one-to-one transform. Comparing Eq. (3.17) and Eq. (3.19) with Eq. (3.20), it is easy to see that the same relation, i.e. Eq. (3.22), exists for the source and boundary conditions in the q and t domains.

In addition, the inversion of Eq. (3.22), called the inverse Q-transform, can be

achieved by taking the inverse Laplace transform of Eq. (3.21) [7], which gives

$$u(\mathbf{x}, q) = \frac{1}{2\pi i} \int_{\gamma - i\infty}^{\gamma + i\infty} \int_0^{\infty} v(\mathbf{x}, q) \exp\left(-p^2 t\right) dt \exp(pq) dp, \tag{3.23}$$

where γ is defined in the same manner as the contour associated with the Laplace transform defined earlier.

From now on, we will frequently use the following simplified notation to denote Eqs. (3.22) and (3.23), which are

$$v(t) = \mathcal{Q}\{u(q)\}(t) \quad \text{and} \quad u(q) = \mathcal{Q}^{-1}\{v(t)\}(q),$$

respectively (we drop the spatial variable $\mathbf{x}$). Some important properties of the Q-transform are presented in Appendix A.

3.2 Mathematical Properties of the Q-transform

The mathematical properties of the scalar Q-transform have been derived by Tamburrino [32] and others [6, 16]. We begin by rewriting the definition of the scalar Q-transform adopted from Eq. (3.22) here, which is

$$v(t) = \mathcal{Q}\{u(q)\}(t) = \frac{1}{2\sqrt{\pi t^3}} \int_0^{\infty} q \exp(-\frac{q^2}{4t}) u(q) dq.$$

Some of the more important properties of the scalar Q-transform are:

- **Invariance of the Dirac function**

$$\mathcal{Q}\{\delta(q)\}(t) = \delta(t) \tag{3.24}$$

- **Linearity**

$$\mathcal{Q}\{au_1(q) + bu_2(q)\}(t) = a\mathcal{Q}\{u_1(q)\}(t) + b\mathcal{Q}\{u_2(q)\}(t), \tag{3.25}$$

where a and b are arbitrary constants.

- **Translation**

$$\mathcal{Q}\{u(q-q_0)\}(t) = \left\{\frac{q_0}{\sqrt{4\pi}}\exp\left(-\frac{q_0^2}{4t}\right)\right\} * \mathcal{Q}\{u(q)\}(t), \tag{3.26}$$

where $*$ stands for the convolution operation.

- **Scaling**

$$\mathcal{Q}\{u(aq)\}(t) = a\mathcal{Q}\{u(q)\}\left(a^2 t\right), \tag{3.27}$$

where a is a positive scaling factor.

- **Q-transform of the first derivative**

$$\mathcal{Q}\{u'(q)\}(t) = \frac{1}{2t}\mathcal{Q}\{qu(q)\}(t) - \mathcal{Q}\left\{\frac{u(q)}{q}\right\}(t) - \frac{[qu(q)]_{0+}}{2\sqrt{\pi t^3}} \tag{3.28}$$

- **Time derivative**

$$\frac{d\mathcal{Q}\left\{u\left(q\right)\right\}\left(t\right)}{dt}=\frac{1}{4t^{2}}\mathcal{Q}\left\{q^{2}u\left(q\right)\right\}\left(t\right)-\frac{3}{2t}\mathcal{Q}\left\{u\left(q\right)\right\}\left(t\right) \tag{3.29}$$

- **Laplace transform**

$$\mathcal{L}\left\{\mathcal{Q}\left\{u\left(q\right)\right\}\left(t\right)\right\}\left(s^{2}\right)=\mathcal{L}\left\{u\left(q\right)\right\}\left(s\right) \tag{3.30}$$

- **Fourier transform**

$$\mathcal{F}\left\{\mathcal{Q}\left\{u\left(q\right)\right\}\left(t\right)\right\}\left(\omega\right)=\int_{0}^{+\infty}u\left(q\right)\exp\left(-q\sqrt{i\omega}\right)dq \tag{3.31}$$

- **Relationship with the Fourier sine transform**

We define the Fourier sine transform of function $u\left(q\right)$ as:

$$U_{s}\left(\omega\right)\equiv\sqrt{\frac{2}{\pi}}\int_{0}^{+\infty}u\left(q\right)\sin\left(\omega q\right)dq, \tag{3.32}$$

we have

$$\begin{aligned}\mathcal{Q}\left\{u\left(q\right)\right\}\left(t\right) &= \sqrt{\frac{2}{\pi}}\int_{0}^{+\infty}\omega\exp\left(-\omega^{2}t\right)U_{s}\left(\omega\right)d\omega &(3.33)\\ &= \frac{1}{\left(2t\right)^{3/2}}\mathcal{Q}\left\{U_{s}\left(\omega\right)\right\}\left(\frac{1}{4t}\right). &(3.34)\end{aligned}$$

- **Relationship with the Fourier cosine transform**

We define the Fourier cosine transform of a function $u(q)$ as:

$$U_c(\omega) \equiv \sqrt{\frac{2}{\pi}} \int_0^{+\infty} u(q) \cos(\omega q) dq, \tag{3.35}$$

we have

$$\mathcal{Q}\{u(q)\}(t) = \sqrt{\frac{2}{\pi}} \int_0^{+\infty} \frac{1}{\sqrt{\pi t}} \left[1 - 2\omega^2 t \Phi\left(1; \frac{3}{2}; -\omega^2 t\right)\right] U_c(\omega) d\omega, \tag{3.36}$$

where $\Phi(\cdot)$ is a confluent hypergeometric function [54].

- **Q-transform of functions with finite support in the q domain**

If $\text{supp}\{u(q)\} \subseteq [q_0, q_1]$, where $\text{supp}\{\cdot\}$ refers to the support of a function, we have:

$$\mathcal{Q}\{u(t)\} = \frac{1}{\sqrt{\pi t}} \left[u(q) \exp\left(-\frac{q^2}{4t}\right)\right]_{q_0^+}^{q_1^-} + \frac{1}{\sqrt{\pi t}} \int_{q_0^+}^{q_1^-} u'(q) \exp\left(-\frac{q^2}{4t}\right) dq. \tag{3.37}$$

- **Q-transform of functions with finite support in the ω domain**

If $\text{supp}\{U_s(\omega)\} \subseteq [\omega_0, \omega_1]$, we have:

$$\mathcal{Q}\{u(t)\} = \frac{1}{\sqrt{2\pi t^3}} \left[U_s(\omega) \exp\left(-\omega^2 t\right)\right]_{\omega_0^+}^{\omega_1^-} + \frac{1}{\sqrt{\pi t}} \int_{\omega_0^+}^{\omega_1^-} U_s'(-\omega) \exp\left(-\omega^2 t\right) d\omega. \tag{3.38}$$

In Appendix A, some of useful Q-transform pairs are provided for quick reference.

Also given, is a short list of mathematical properties of a related transform, i.e. the $\widetilde{Q}$-transform .

3.3 Numerical Implementation of the Scalar Q-transform

The scalar Q-transform defined in the previous sections reveals the unique mapping relation between solutions of wave equation problems and those of diffusion equation problems. By evaluating Eq. (3.22) directly, we can convert solutions of the scalar wave equation problems to solutions of the scalar diffusion equation problems. Unfortunately, the inverse of this process, i.e. the conversion of solutions of the scalar diffusion equation problems to those of scalar wave equation problems suffers from numerical instability as pointed out by Gibert [26] and Ross [7]. This instability originates from the mathematical nature of Eq. (3.22), which is a Fredholm integral of the first kind [55]. We also notice that Eq. (3.22) is an infinite integral from zero to infinity, which requires some sort of truncation to be imposed during numerical evaluation. This issue, as well as methods of numerically approximating Eq. (3.22), will be discussed in this section.

3.3.1 Numerical Approximation of the Q-transform

The following numerical schemes have been proposed in [32] to evaluate the Q-transform. The numerical approximation of a function $u(q)$ could be expressed in the form of

$$u(q) = \sum_{k=1}^{N} f(u_k)\, s_k(q), \tag{3.39}$$

where u_k is a given sequence with $k = 1, 2, \ldots, N$, $0 \leq q_1 < q_2 < \ldots < q_N$, and N is an integer. $f(u_k)$ and $s_k(q)$ are unknown functions of u_k and q is to be found. The Q-transform of $u(q)$ is given by

$$\mathcal{Q}\{u(q)\}(t) = \sum_{k=1}^{N} f(u_k)\,\mathcal{Q}\{s_k(q)\}(t). \tag{3.40}$$

A discussion on two methods of approximation follows.

Let $u(q)$ be a piecewise constant. Then,

$$u(q) = \sum_{k=1}^{N} u_k \left[H(q - q_k) - H(q - q_{k+1})\right], \tag{3.41}$$

where one more point $u_{k+1} = 0$ for $q_{k+1} > q_k$ is added for convenience and $H(q)$ is the so-called Heaviside step function. Taking the Q-transform of both sides of Eq. (3.41), we obtain

$$\mathcal{Q}\{u(q)\}(t) = \sum_{k=1}^{N} u_k \mathcal{Q}\{H(q - q_k) - H(q - q_{k+1})\}(t),$$

which yields

$$\mathcal{Q}\{u(q)\}(t) = \sum_{k=1}^{N} u_k \left[F_k(t) - F_{k+1}(t)\right], \tag{3.42}$$

where (See section 3.2)

$$F_k(t) \equiv \mathcal{Q}\{H(q - q_k)\}(t) = \frac{1}{\sqrt{\pi t}} \exp\left(-\frac{q_k^2}{4t}\right). \tag{3.43}$$

Rearranging terms, Eq. (3.42) can be rewritten as

$$\mathcal{Q}\{u(q)\}(t) = \sum_{k=1}^{N+1} (u_k - u_{k-1}) F_k(t), \tag{3.44}$$

where we also set $u_0 = 0$. Obviously, Eq. (3.44) is more efficient than Eq. (3.42) in terms of computational costs.

Using a similar strategy, employing a piece-wise linear approximation of $u(q)$:

$$\begin{aligned} u(q) &= \sum_{k=1}^{N-1} \left\{ u_k + (u_{k+1} - u_k) \frac{q - q_k}{q_{k+1} - q_k} \right\} [H(q - q_k) - H(q - q_{k+1})] \\ &= \sum_{k=1}^{N-1} \frac{u_{k+1}(q - q_k) - u_k(q - q_{k+1})}{q_{k+1} - q_k} [H(q - q_k) - H(q - q_{k+1})]. \end{aligned} \tag{3.45}$$

we have,

$$\mathcal{Q}\{u(q)\}(t) = \sum_{k=1}^{N-1} \frac{u_{k+1}}{q_{k+1} - q_k} \mathcal{Q}\{(q - q_k)[H(q - q_k) - H(q - q_{k+1})]\}. \tag{3.46}$$

Further manipulations of Eq. (3.46) lead to cumbersome semi-analytical expressions imposing an extremely heavy computational burden.

Instead, if the support of $u(q)$ is $[q_1, q_N]$, one can show that (See Eq. (3.37))

$$\mathcal{Q}\{u(q)\}(t) = \frac{1}{\sqrt{\pi t}} \left[u_1 \exp\left(-\frac{q_1^2}{4t}\right) - u_N \exp\left(-\frac{q_N^2}{4t}\right) \right] + I(t), \tag{3.47}$$

where,

$$I(t) \equiv \frac{1}{\sqrt{\pi t}} \sum_{k=1}^{N-1} u_k' \int_{q_k}^{q_{k+1}} \exp\left(-\frac{q^2}{4t}\right) dq, \tag{3.48}$$

where u'_k is the first order approximation of the derivative of $u(q)$, i.e.,

$$u'_k = \frac{u_{k+1} - u_k}{q_{k+1} - q_k}. \tag{3.49}$$

By introducing the complementary error function, which is defined as:

$$\operatorname{erfc}(x) \equiv \frac{2}{\sqrt{\pi}} \int_x^{+\infty} \exp\left(-y^2\right) dy, \tag{3.50}$$

the integral included in Eq. (3.48) can be evaluated and $I(t)$ can then be shown as:

$$I(t) \equiv \frac{1}{\sqrt{\pi t}} \sum_{k=1}^{N-1} u'_k \left[\operatorname{erfc}\left(\frac{q_k}{2\sqrt{t}}\right) - \operatorname{erfc}\left(\frac{q_{k+1}}{2\sqrt{t}}\right) \right]. \tag{3.51}$$

Again, with the rearrangements of terms,

$$I(t) \equiv \frac{1}{\sqrt{\pi t}} \sum_{k=1}^{N} \left(u'_k - u'_{k-1}\right) \operatorname{erfc}\left(\frac{q_k}{2\sqrt{t}}\right), \tag{3.52}$$

subject to the condition that $u'_0 = u'_N = 0$.

The piece-wise linear approximation presented in Eq. (3.52) results in similar computational costs as the piece-wise constant approximation, i.e. Eq. (3.44). However, the calculation accuracy improves in general.

3.3.2 Truncation of the Infinite Integral

In order to numerically evaluate the Q-transform, which is an integral from zero to infinity in the q domain as specified before, we must truncate the integral in ways that offer sufficient accuracy and, hopefully, involve reduced computational costs at

the same time. This mission can also be interpreted as an optimization task in order to determine the support of the Q-transform.

As reported in [32], the Q-transform can be represented in forms that differ from Eq. (3.22), such as

$$v(t) = \mathcal{Q}\{u(q)\}(t) = \frac{1}{\sqrt{\pi e t}} \int_0^{+\infty} w(q)\, u\left(q\sqrt{2t}\right) dq, \tag{3.53}$$

where

$$w(x) \equiv \sqrt{e} x \exp\left(-\frac{x^2}{2}\right). \tag{3.54}$$

As shown in Figure 3.1 and Figure 3.2, the function $w(x)$ reaches its maximum at $x = 1$ and then decays very fast as x becomes larger than one. This fact reveals that, when the integral in Eq. (3.53) is evaluated at a certain time t_0, the most relevant part of the q domain signal $u(q)$ is constrained within a region $q \in [q_1, q_2]$ 'centered' at $q = \sqrt{2t_0}$, or equivalently, $x = 1$.

Since $q = x\sqrt{2t_0}$, the lower and upper bounds of the region that contributes most to the value of $\mathcal{Q}\{u(q)\}(t)$, i.e. $[q_1, q_2]$, can be determined by solving equation

$$w(x) = x_0, \tag{3.55}$$

where x_0 is a predetermined threshold based on the behavior of function $u(q)$ that is applied and the expected level of numerical accuracy. The smaller solution x_1 of the Eq. (3.55) can be obtained analytically with the help of the so-called Lambert's W function [56] while the bigger solution x_2 can be reached numerically. Since the x_1 is often very small, we can set it to zero while some typical values of x_2 are listed in

Table 3.1.

Table 3.1: Maximum support for numerical evaluation of the Q-transform

x_0	1E-4	1E-5	1E-6	1E-7
$\sqrt{2}x_2$	6.9	7.6	8.1	8.7

In our experience, the piece-wise linear approximation appears to be more efficient and reliable in most applications. Although the piece-wise constant approximation is equally efficient, it is less accurate. The higher order approximation could be very complex in implementation and is not necessary. The interval for truncating the improper integral Eq. (3.53) in a numerical evaluation can be determined by solving Eq. (3.55) numerically. Beyond these considerations, the size of interval of the evaluation points is also critical for a successful numerical evaluation.

3.4 Derivations of the Vector Q-transform

The Q-transform was extended from scalar form to vector form by Lee in low-frequency EM field analysis [6]. The underlining strategy is similar to that of the scalar case. However, some special considerations had to be taken into account. For the sake of thoroughness, this derivation will be sketched here.

If we consider only linear, isotropic and charge free media, the Maxwell's equations (Eqs. (2.1)-(2.4)) together with the constitutive equations (Eqs. (2.10)-(2.12)) can be written as:

$$\nabla \times \mathbf{E}(\mathbf{x},t) = -\mu(\mathbf{x}) \frac{\partial \mathbf{H}(\mathbf{x},t)}{\partial t} \tag{3.56}$$

$$\nabla \times \mathbf{H}(\mathbf{x},t) = \sigma(\mathbf{x}) \mathbf{E}(\mathbf{x},t) + \varepsilon(\mathbf{x}) \frac{\partial \mathbf{E}(\mathbf{x},t)}{\partial t} + \mathbf{J}_s(\mathbf{x},t). \tag{3.57}$$

Assuming that μ is constant, Eqs. (3.56)-(3.57) implies

$$\nabla \times \nabla \times \mathbf{E}(\mathbf{x},t) + \mu\sigma(\mathbf{x})\frac{\partial}{\partial t}\mathbf{E}(\mathbf{x},t) + \mu\varepsilon(\mathbf{x})\frac{\partial^2}{\partial t^2}\mathbf{E}(\mathbf{x},t) = -\mu\frac{\partial}{\partial t}\mathbf{J}_s(\mathbf{x},t). \quad (3.58)$$

In eddy current applications, the EM field is considered magnetoquasistatic (MQS) and the displacement current term in Eq. (3.57) can be neglected. Then, by substituting Eq. (3.56) into Eq. (3.57), we obtain the diffusive governing equation for the electric field, which is

$$\nabla \times \nabla \times \mathbf{E}(\mathbf{x},t) + \mu\sigma(\mathbf{x})\frac{\partial}{\partial t}\mathbf{E}(\mathbf{x},t) = -\mu\frac{\partial}{\partial t}\mathbf{J}_s(\mathbf{x},t). \quad (3.59)$$

The corresponding initial and boundary conditions are given by

$$\mathbf{E}(\mathbf{x},0) = \mathbf{0}, \quad \mathbf{E}_\Gamma = \mathbf{E}(\mathbf{x}_b,t) \quad t > 0,$$

where Γ is the boundary of the solution domain at $\mathbf{x} = \mathbf{x}_b$. On the other side, for a lossless problem, we have

$$\nabla \times \nabla \times \mathbf{E}(\mathbf{x},t) + \mu\varepsilon(\mathbf{x})\frac{\partial^2}{\partial t^2}\mathbf{E}(\mathbf{x},t) = -\mu\frac{\partial}{\partial t}\mathbf{J}_s(\mathbf{x},t). \quad (3.60)$$

Therefore, referring to the diffusive electric field shown in Eq. (3.59), we can construct a fictitious wave field in the q domain by replacing the first-order time derivative with a second-order derivative with respect to q , i.e.

$$\nabla \times \nabla \times \mathbf{U}(\mathbf{x},q) + \mu\sigma(\mathbf{x})\frac{\partial^2}{\partial q^2}\mathbf{U}(\mathbf{x},q) = -\mu\frac{\partial^2}{\partial q^2}\mathbf{j}_s(\mathbf{x},q), \quad (3.61)$$

together with

$$\mathbf{U}(\mathbf{x},0)=\frac{\partial}{\partial q}\mathbf{U}(\mathbf{x},q)\,|_{q=0}=\mathbf{0},\quad \mathbf{U}_\Gamma=\mathbf{U}(\mathbf{x}_b,q)\quad q>0,$$

where $\mathbf{j}_s$ is the corresponding external source for the fictitious field. It is clear that, by comparing Eq. (3.61) with Eq. (3.60), the fictitious field $\mathbf{U}(\mathbf{x},q)$ behaves as a propagating wave with a velocity of $(\mu\sigma)^{-1/2}$ while the independent variable q has the dimension of square root of time.

Again, we take the Laplace transform to both Eqs. (3.59) and (3.61) from t to s and q to p, respectively. We obtain

$$\nabla\times\nabla\times\widehat{\mathbf{E}}(\mathbf{x},s)+\mu\sigma(\mathbf{x})\,s\widehat{\mathbf{E}}(\mathbf{x},s)=-\mu s\widehat{\mathbf{J}}_s(\mathbf{x},s) \tag{3.62}$$

$$\widehat{\mathbf{E}}|_\Gamma=\widehat{\mathbf{E}}(\mathbf{x}_b,s)\quad -\pi/2<\arg(s)<+\pi/2 \tag{3.63}$$

and

$$\nabla\times\nabla\times\widehat{\mathbf{U}}(\mathbf{x},p)+\mu\sigma(\mathbf{x})\,p^2\widehat{\mathbf{U}}(\mathbf{x},p)=-\mu p^2\widehat{\mathbf{j}}_s(\mathbf{x},p)\,, \tag{3.64}$$

$$\widehat{\mathbf{U}}|_\Gamma=\widehat{\mathbf{U}}(\mathbf{x}_b,p)\quad -\pi/2<\arg(p)<+\pi/2. \tag{3.65}$$

By observing the similarities between Eq. (3.62) and (3.64), and selecting $s=p^2$ and limiting $\arg(p)$ to the domain $(-\pi/4,+\pi/4)$, we may subtract Eq. (3.62) from Eq. (3.64) to obtain:

$$\nabla\times\nabla\times\widehat{\mathbf{F}}(\mathbf{x},p)+\mu\sigma(\mathbf{x})\,p^2\widehat{\mathbf{F}}(\mathbf{x},p)=\mathbf{0} \tag{3.66}$$

$$\widehat{\mathbf{F}}|_\Gamma=\mathbf{0},\quad -\pi/4<\arg(p)<+\pi/4, \tag{3.67}$$

where $\widehat{\mathbf{F}}(\mathbf{x}, p)$ is the difference between $\widehat{\mathbf{E}}(\mathbf{x}, p^2)$ and $\widehat{\mathbf{U}}(\mathbf{x}, p)$, while conditions for source and boundary terms

$$\widehat{\mathbf{J}}\left(\mathbf{x}, p^2\right) = \widehat{\mathbf{j}}(\mathbf{x}, p) \tag{3.68}$$

$$\widehat{\mathbf{E}}\left(\mathbf{x}_b, p^2\right) = \widehat{\mathbf{U}}(\mathbf{x}_b, p) \tag{3.69}$$

are satisfied. Then, by multiplying both sides of Eq. (3.66) with the complex conjugate of $\widehat{\mathbf{F}}(\mathbf{x}, p)$ and integrating over the region V enclosed in boundary Γ, we can obtain (with some additional manipulations)

$$\int_V |\nabla \times \widehat{\mathbf{F}}(\mathbf{x}, p)|^2 + \mu\sigma(\mathbf{x}) p^2 |\widehat{\mathbf{F}}(\mathbf{x}, p)|^2 dv = \mathbf{0}, \tag{3.70}$$

which implies

$$\widehat{\mathbf{E}}\left(\mathbf{x}, p^2\right) = \widehat{\mathbf{U}}(\mathbf{x}, p), \tag{3.71}$$

or

$$\widehat{\mathbf{E}}(\mathbf{x}, s) = \widehat{\mathbf{U}}\left(\mathbf{x}, \sqrt{s}\right). \tag{3.72}$$

The integral relation between the electric field $\mathbf{E}(\mathbf{x}, t)$ and its fictitious wave domain counterpart $\mathbf{U}(\mathbf{x}, q)$ is then presented, by taking the inverse Laplace transform to both sides of Eq. (3.72), as we did before:

$$\mathbf{E}(\mathbf{x}, t) = \frac{1}{2\sqrt{\pi t^3}} \int_0^{+\infty} q \exp(-\frac{q^2}{4t}) \mathbf{U}(\mathbf{x}, q) dq. \tag{3.73}$$

This vector relation is identical as Eq. (3.22) for scalar case. A similar transforming

relation can be derived from Eq. (3.68) and (3.69) for the corresponding source and boundary conditions.

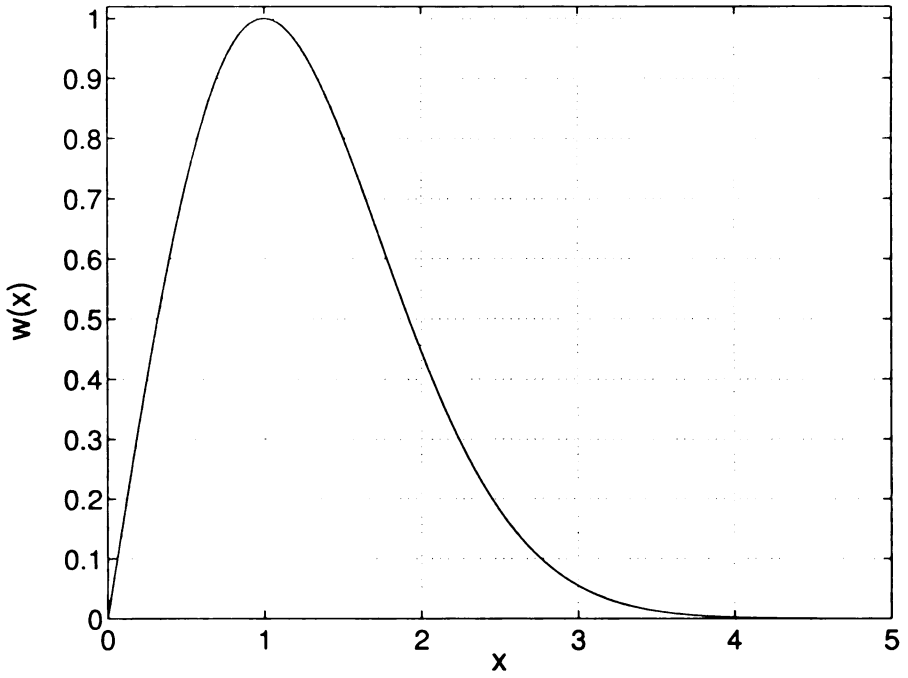

Figure 3.1: Weighting function of the Q-transform in linear scale.

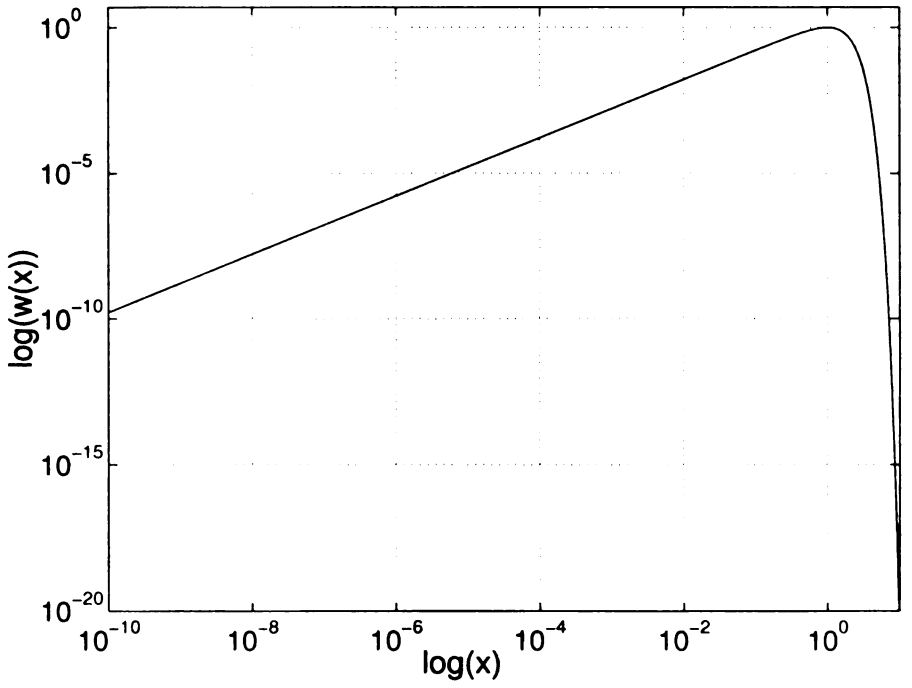

Figure 3.2: Weighting function of the Q-transform in logarithmic scale

CHAPTER 4

TIME-OF-FLIGHT EXTRACTION FOR TRANSIENT DIFFUSIVE FIELDS

In this chapter, the main issues concerning the extraction of time-of-flight information from measurements of transient diffusive fields are discussed with reference to a scalar configuration. We will show that time-of-flight information associated with position of a "small" scatterer can be extracted providing appropriate excitation signals are applied. In addition, numerical simulations are presented along with theoretical analysis. We will also introduce a vector diffusive field configuration briefly. The approaches discussed in section 4.1 and 4.3 have been proposed in [32, 33]. Numerical validation and analysis has been developed in [34, 35].

4.1 A Scalar Diffusion Equation Problem

As we pointed out in the previous chapters, the time-of-flight concept has no physical meaning in the case of diffusion phenomena. However, with help of Q-transform, a fictitious wave field could be established with respect to the diffusive field of interest. The time-of-flight information could be estimated in the fictitious wave domain and converted back to obtain its equivalent in the diffusion domain. In general, this process of estimating the time-of-flight could be very complicated. In this section, we will introduce a simple reference scalar diffusive field problem that shows how the position of a "small" scatterer embedded in a homogeneous medium with a point source can be estimated.

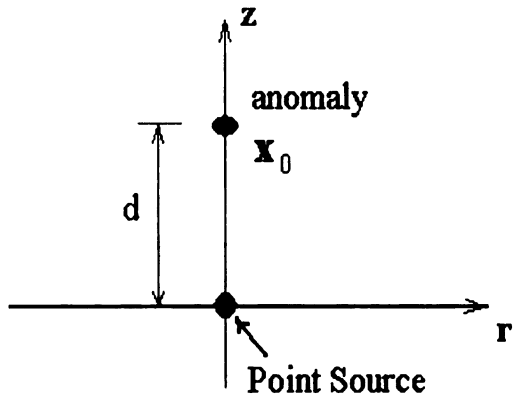

Figure 4.1: A small anomaly in the vicinity of a point source

Referring to Figure 4.1, assume that the host medium is a conductor of conductivity σ_0, permeability μ_0 and that the displacement current can be neglected. Also, we assume that the anomaly is confined within the ball $B_R(\mathbf{x}_0) \hat{=} \{\mathbf{x} \in \Re^3 | \, |\mathbf{x} - \mathbf{x}_0| \leq R\}$, where $R \ll |\mathbf{x}_0|$. A point source is located at the origin of the coordinate system and the measured quantity is the reaction field (evaluated at the origin of the coordinates system) due to the anomaly. The unknown quantity that is sought in this canonical problem is the distance from the scatterer to the origin, i.e. $d \hat{=} |\mathbf{x}_0|$ shown in Figure 4.1. In order to show the main ideas underlying the proposed approach, we consider a scalar diffusion equation first. We further indicate that the position of the anomaly is arbitrary. The anomaly is on the z-axis, as shown in Figure 4.1. However, it could be anywhere else.

4.1.1 Time-of-Flight and Peak Value of the Eddy Current Measurement

To make time-of-flight information "visible" in eddy current measurements, our strategy is to build a link between the time-of-flight for the fictitious field and certain

characteristic properties of the measured ECT signal in the time domain.

We notice that the measurement from a wave receiver is zero before a certain time q_0 due to the propagation delay of the excitation signal. The Q-transform of such a fictitious wave domain signal $u(q)$ can be expressed as (See Eq. (3.37) in section 3.2):

$$v(t) = \mathcal{Q}\{u(q)\}(t) = \frac{u(q_0^+)}{\sqrt{\pi t}} \exp\left(-\frac{q_0^2}{4t}\right) + \frac{1}{\sqrt{\pi t}} \int_{q_0^+}^{+\infty} u'(q) \exp\left(-\frac{q^2}{4t}\right) dq, \quad (4.1)$$

where $u'(q)$ is a unknown function. If the first term of the r.h.s of the Eq. (4.1) is dominant, i.e.

$$\left| u(q_0^+) \exp\left(-\frac{q_0^2}{4t}\right) \right| \gg \left| \int_0^{+\infty} u'(q) \exp\left(-\frac{q^2}{4t}\right) dq \right|, \quad (4.2)$$

$v(t)$ can then be written in a more explicit form as

$$v(t) \cong \frac{u(q_0^+)}{\sqrt{\pi t}} \exp\left(-\frac{q_0^2}{4t}\right) \quad (4.3)$$

and obtain its maximum

$$|v|_{max} = \frac{|u(q_0^+)|}{q_0} \sqrt{\frac{2}{\pi e}} \quad (4.4)$$

at $t_{max} = q_0^2/2$. This relation between the time-of-flight q_0 and peak position t_{max} of the time domain measurement is illustrated in Figure 4.2.

It has been shown [32] that, if $u(q)$ is finite and different from zero only for $q > q_0$, $u(q)$ is differentiable for $q > q_0$, $|u'(q)|$ is bounded by a constant M, and

$$M \ll |u(q_0^+)|/q_0, \quad (4.5)$$

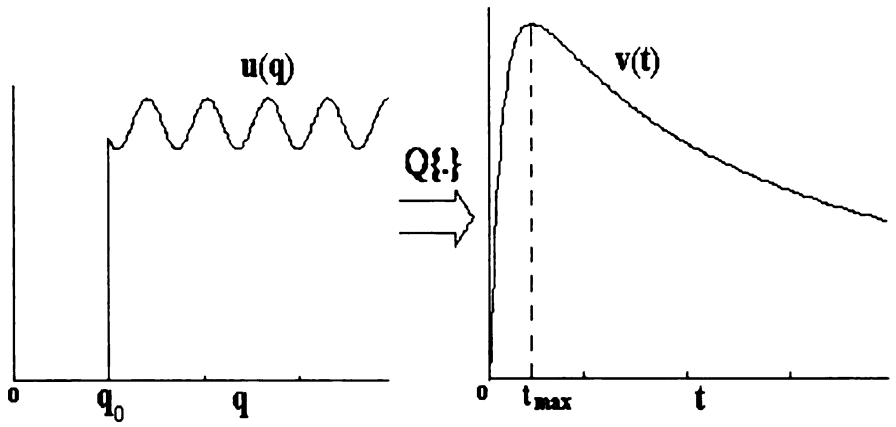

Figure 4.2: The relation between time-of-flight q_0 and peak position t_{max} of the eddy current measurement

then Eq. (4.2) can be satisfied [33]. Similarly, in a neighborhood of t_{max}, when $u(q)$ contains a Dirac pulse such as

$$u(q) = \alpha\delta(q - q_f) + h(q - q_f), \tag{4.6}$$

where α is a scaling constant, $h(q)$ vanishes for $q < 0$ and $|h(q)|$ is bounded by a constant M_1, and

$$M_1 \ll \alpha/q_0. \tag{4.7}$$

Eq. (4.2) can also be satisfied. The corresponding peak value and peak position are

$$|v|_{max} = \frac{|\alpha|}{2q_0^2}\sqrt{\frac{1}{\pi}\left(\frac{6}{e}\right)^3}$$

and $t_{max} = q_0^2/6$, respectively. Therefore, under proper conditions (4.5) or (4.7), the position of the peak of $|v(t)|$ is, simply, proportional to the square of time-of-flight q_0. If additive noise $n(t)$ is present, the peak is observable providing its maximum

value is much bigger than noise level $|n(t)|$, i.e.

$$\frac{|u(q_0^+)|}{q_0}\sqrt{\frac{2}{\pi e}} \gg |n(t)| \tag{4.8}$$

or

$$\frac{|\alpha|}{2q_0^2}\sqrt{\frac{1}{\pi}\left(\frac{6}{e}\right)^3} \gg |n(t)|. \tag{4.9}$$

It is worth noting that Eq. (4.8) not only sets a limit on the acceptable noise level but also imposes an upper limit on the retrievable time-of-flight q_0 for a given $u(q_0^+)$ and noise level.

The necessary conditions (4.5) and (4.7) are stated in terms of the fictitious wave $u(q)$. The only way to impose those conditions is to design the source of the fictitious wave problem properly and the excitation signal to be used during the eddy current test.

4.1.2 Analytical Solutions of the Scalar Problem

The mathematical description of the eddy current problem shown in Figure 4.1 is in the form of a diffusion equation, which is

$$\begin{cases} \nabla^2 v(\mathbf{x},t) - s(\mathbf{x})\,\partial_t v(\mathbf{x},t) = G(\mathbf{x},t) & \text{in} \quad \Re^3, \quad \text{for} \quad t \geq 0 \\ v(\mathbf{x},0) = 0 & \text{in} \quad \Re^3 \\ \lim\limits_{|\mathbf{x}|\to\infty} v(\mathbf{x},t) = 0 & \text{for} \quad t \geq 0 \end{cases} \tag{4.10}$$

where $s(\mathbf{x})$ is a function of material properties and $G(\mathbf{x},t) = \delta(\mathbf{x})\,g(t)$ is a point source, located at the origin of the coordinate system. The fictitious time domain

counterpart of Eq. (4.10) can then be written as

$$\begin{cases} \nabla^2 u(\mathbf{x},q) - s(\mathbf{x})\,\partial_{qq} u(\mathbf{x},q) = F(\mathbf{x},t) & \text{in} \quad \Re^3, \quad \text{for} \quad q \geq 0 \\ u(\mathbf{x},0) = \partial_q u(\mathbf{x},0) = 0 & \text{in} \quad \Re^3 \\ \lim\limits_{|\mathbf{x}|\to\infty} u(\mathbf{x},q) = 0 & \text{for} \quad q \geq 0 \end{cases} \tag{4.11}$$

where $F(\mathbf{x},q) = \delta(\mathbf{x})\, f(q)$ is a point source in fictitious time domain. Let $\sigma(\mathbf{x})$ be the conductivity in the region of interest, $\chi(\mathbf{x}) \hat{=} \sigma(\mathbf{x})/\sigma_0 - 1$ be the contrast function, and let $s(\mathbf{x}) \hat{=} [1+\chi(\mathbf{x})]/c_0^2$, where $c_0 = 1/\sqrt{\mu_0\sigma_0}$ is the velocity of the fictitious wave. With the imposition of the additional constraint, as discussed in Chapter 3,

$$g(t) = Q\{f(q)\}(t), \tag{4.12}$$

$v(\mathbf{x},t)$ and $u(\mathbf{x},q)$ constitute a Q-transform pair, i.e.

$$v(\mathbf{x},t) = Q\{u(\mathbf{x},q)\}(t). \tag{4.13}$$

It is straightforward to obtain an analytical solution of the wave equation problem given by Eq. (4.11) while Eq. (4.13) can then be applied to obtain the analytical solution of the diffusion equation problem given by Eq. (4.10).

If we define $u_0(\mathbf{x},q)$ as incident wave field (which is solution of Eq. (4.11) if the contrast function $\chi(\mathbf{x})$ is zero everywhere, i.e. anomaly doesn't exist), then we have for the scattered field $u_s(\mathbf{x},q)$

$$u_s(\mathbf{x},q) = u(\mathbf{x},q) - u_0(\mathbf{x},q). \tag{4.14}$$

It can be shown that $u_s(\mathbf{x}, q)$ is the solution of the wave equation problem

$$\begin{cases} \nabla^2 u_s(\mathbf{x}, q) - s(\mathbf{x})\,\partial_{qq} u_s(\mathbf{x}, q) = \dfrac{\chi(\mathbf{x})}{c_0^2}\partial_{qq} u_0(\mathbf{x}, q) & \text{in} \quad \Re^3, \quad \text{for} \quad q \geq 0 \\ u(\mathbf{x}, 0) = \partial_q u(\mathbf{x}, 0) = 0 & \text{in} \quad \Re^3 \\ \lim\limits_{|\mathbf{x}| \to \infty} u(\mathbf{x}, q) = 0 & \text{for} \quad q \geq 0 \end{cases} \tag{4.15}$$

and the solution of the corresponding diffusion equation problem, i.e. the measured signal in the time domain, is $v_s(\mathbf{x}, t) = \mathcal{Q}\{u_s(\mathbf{x}, q)\}(t)$.

Eq. (4.15) can be further simplified by introducing the first-order Born approximation, which says that the unknown field inside the anomaly can be replaced with the incident field at the same location providing that the scattered field is "weak". In addition, we can replace the source term in the r.h.s of Eq. (4.15) with a point source located at the center of the anomaly. This yields

$$\begin{cases} \nabla^2 u_s(\mathbf{x}, q) - \dfrac{1}{c_0^2}\partial_{qq} u_s(\mathbf{x}, q) = \delta(\mathbf{x} - \mathbf{x}_0) f_s(q) & \text{in} \quad \Re^3, \quad \text{for} \quad q \geq 0 \\ u(\mathbf{x}, 0) = \partial_q u(\mathbf{x}, 0) = 0 & \text{in} \quad \Re^3 \\ \lim\limits_{|\mathbf{x}| \to \infty} u(\mathbf{x}, q) = 0 & \text{for} \quad q \geq 0 \end{cases} \tag{4.16}$$

where

$$f_s(q) \hat{=} \frac{K}{c_0^2}\partial_{qq} u_0(\mathbf{x}_0, q), \tag{4.17}$$

$$K \hat{=} \int_{B_R(\mathbf{x}_0)} \chi(\mathbf{x}) d\mathbf{x}, \tag{4.18}$$

and

$$u_0(\mathbf{x}_0, q) = -\frac{f(q - |\mathbf{x}_0|/c_0)}{4\pi |\mathbf{x}_0|}. \tag{4.19}$$

Now, the scattered field $u_s(\mathbf{x}, q)$ can be treated as a propagating wave launched by a point source, which should be in the same form as Eq. (4.19), i.e.

$$u_s(\mathbf{x}_0, q) = -\frac{f_s(q - |\mathbf{x} - \mathbf{x}_0|/c_0)}{4\pi |\mathbf{x} - \mathbf{x}_0|}. \tag{4.20}$$

Subsequently, by substituting Eq. (4.17) and (4.19) into Eq. (4.20), we can express the scattered field as:

$$u_s(\mathbf{x}, q) = \frac{1}{4\pi |\mathbf{x} - \mathbf{x}_0| c_0^2} \frac{K}{4\pi |\mathbf{x}_0|} \partial_{qq} f(q - |\mathbf{x} - \mathbf{x}_0|/c_0 - |\mathbf{x}_0|/c_0). \tag{4.21}$$

To reduce the complexity of the above expression, we set our measuring point at $\mathbf{x} = \mathbf{0}$. This allows us to rewrite the scattered field as:

$$u_s(\mathbf{0}, q) = -\frac{K}{(4\pi |\mathbf{x}_0| c_0)^2} \partial_{qq} f(q - 2|\mathbf{x}_0|/c_0). \tag{4.22}$$

The following approach of designing the excitation signal consists of developing a 'simple' analytical model for the measured quantity in the fictitious time domain and thus imposing either constraint (4.5) or (4.7) on $f(q)$. Finally, $g(t)$ can be obtained as the Q-transform of $f(q)$. Notice that the design of the source terms $f(q)$ and $g(t)$ depends on the geometry under consideration.

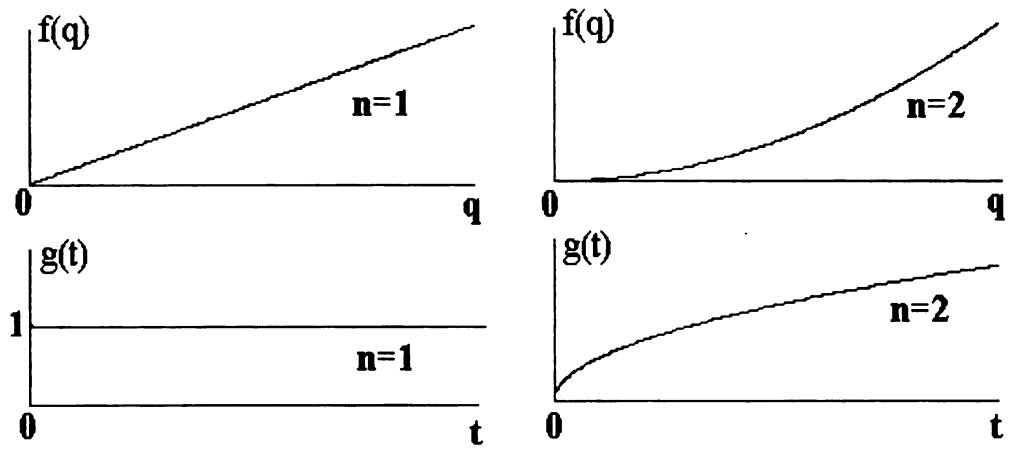

Figure 4.3: Time domain and fictitious time domain excitation signals as given by Eq. (4.23) and (4.24), respectively (q_i equals zero in all cases).

4.1.3 Design of the Excitation Signal

The design of the excitation signal in the fictitious time domain was discussed in [32]. A candidate signal is:

$$f(q) = (q - q_i)^n H(q - q_i), \tag{4.23}$$

where q_i is a nonnegative constant. It can be shown that Eq. (4.7) is automatically satisfied for n =1 whereas Eq. (4.5) is automatically satisfied for n =2. The corresponding time domain excitation signals are

$$g(t) = Q\{f(q)\}(t) = \begin{cases} erfc\left(q_i/\sqrt{4t}\right) & n = 1 \\ 4\sqrt{\frac{t}{\pi}}\exp\left(-\frac{q_i^2}{4t}\right) - 2q_i\mathrm{erfc}\left(\frac{q_i}{2\sqrt{t}}\right) & n = 2 \end{cases}. \tag{4.24}$$

Examples of both time domain and fictitious time domain excitation signals are shown in Figure 4.3.

Using these excitation signals, the scattered field in time domain can be obtained by substituting Eq. (4.23) into Eq. (4.22) and applying the Q-transform to the result. This yields

$$v_s(\mathbf{0},t) = \begin{cases} Bq_f \exp\left(-q_f^2/4t\right)/\sqrt{4\pi t^3} & n=1 \\ 2B\exp\left(-q_f^2/4t\right)/\sqrt{\pi t} & n=2 \end{cases}, \tag{4.25}$$

where $B \hat{=} K/(4\pi c_0 |\mathbf{x_0}|)^2$ and $q_f \hat{=} q_i + 2|\mathbf{x}_0|/c_0$. Finally, the positions of the peak values of the scattered signal $v_s(\mathbf{0},t)$ can be shown as

$$t_{\max} = \begin{cases} q_f^2/6 & n=1 \\ q_f^2/2 & n=2 \end{cases}. \tag{4.26}$$

The peak values are

$$\frac{v_{s,\max}}{B} = \begin{cases} \sqrt{54/(\pi e^3)}\Big/q_f^2 & n=1 \\ \sqrt{8/(\pi e)}\Big/q_f & n=2 \end{cases} \tag{4.27}$$

and the solutions $|\mathbf{x}_0|$ of the inverse problem are

$$|\mathbf{x}_0| = \begin{cases} \left(\sqrt{6t_{\max}} - q_i\right) c_0/2 & n=1 \\ \left(\sqrt{2t_{\max}} - q_i\right) c_0/2 & n=2 \end{cases}. \tag{4.28}$$

We want to indicate that other choices of excitation signals may exist. Also, it is possible to associate other properties of the time domain measurements with time-of-flight.

4.2 Numerical Simulation: A Scalar Problem

This section presents a finite element method based numerical simulation to show the effectiveness of the proposed method. Most of the results presented herein have been published in [34] except for part of section 4.2.2.

4.2.1 Numerical Implementation

The numerical solutions for diffusion equation problems given by equation (4.10) have been obtained. In addition, the numerical solutions for the corresponding wave equation problem given by Eq. (4.11) have also been obtained for the purpose of cross validation. All numerical calculations were carried out using a commercial package called FEMLAB®. In order to further simplify the problem and reduce the computational burden, which is always a concern when finite element techniques are employed, several important simplifications have been made.

Instead of solving Eqs. (4.10)-(4.11) directly for total fields $u(\mathbf{x}, q)$ and $v(\mathbf{x}, t)$, we will solve Eq. (4.16) and its time domain equivalent for $u_s(\mathbf{x}, q)$ and $v_s(\mathbf{x}, t)$. This strategy can ease the process of introducing source excitation and, more critically, avoid numerical difficulties that arise when subtracting two quantities with small differences (as in the case of Eq. (4.14)).

Notice that the direction from the origin to the small anomaly is not relevant, we can reduce the original three-dimensional problem to a two-dimensional axisymmetric formulation. The governing equations for $u_s(\mathbf{x}, q)$ and $v_s(\mathbf{x}, t)$ in cylindrical

coordinates (r, z) are

$$\frac{\partial^2 v_s(\mathbf{x},t)}{\partial r^2} + \frac{1}{r}\frac{\partial v_s(\mathbf{x},t)}{\partial r} + \frac{\partial^2 v_s(\mathbf{x},t)}{\partial z^2} - \frac{1}{c_0^2}\frac{\partial v_s(\mathbf{x},t)}{\partial t} = \frac{\chi(\mathbf{x})}{c_0^2} Q\left\{\partial_{qq} u(\mathbf{x}_0, q)\right\} \quad (4.29)$$

and

$$\frac{\partial^2 u_s(\mathbf{x},q)}{\partial r^2} + \frac{1}{r}\frac{\partial u_s(\mathbf{x},q)}{\partial r} + \frac{\partial^2 u_s(\mathbf{x},q)}{\partial z^2} - \frac{1}{c_0^2}\frac{\partial^2 u_s(\mathbf{x},q)}{\partial q^2} = \frac{\chi(\mathbf{x})}{c_0^2}\partial_{qq} u(\mathbf{x}_0, q), \quad (4.30)$$

respectively. In the above equations, $u_0(\mathbf{x}, q)$ is determined analytically using Eq. (4.19).

Additional simplification is achieved by setting the delay q_i of excitation signal to zero, which reduces the q domain excitation signal to:

$$f(q) = q^n H(q), \quad n = 1, 2 \quad (4.31)$$

and the time domain excitation signal to:

$$g(t) = \begin{cases} 1 & n = 1 \\ 4\sqrt{t/\pi} & n = 2 \end{cases}. \quad (4.32)$$

Other specifications include: the anomaly is a ball of radius $R = 0.1$ mm and the distance between its center and the origin of the coordinate system is $|\mathbf{x}_0|$=10 mm. The conductivity σ_0 of the surrounding material is 3.54×10^7S/m (copper) and the relative permeability is 1, which corresponds to a fictitious wave velocity of 0.15 $m/\sqrt{s}$. The anomaly has a conductivity of 2.655×10^7 S, which implies a contrast

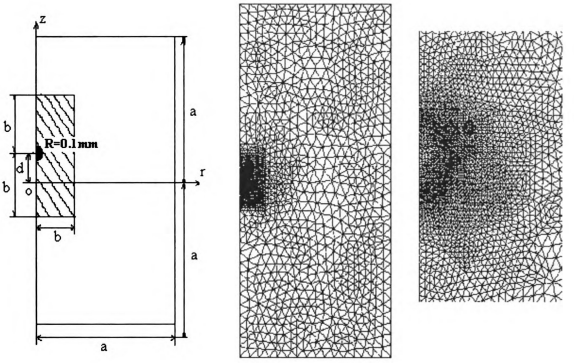

Figure 4.4: Left: A schematic of the geometry for the numerical simulation; Center: The finite element mesh generated by FEMLAB®; Right: Expanded view of the mesh in the region containing the anomaly.

$\chi = -0.25$ in $B_R(\mathbf{x}_0)$.

As shown in Figure 4.4 (left), the small dark area represents the anomaly (not in scale), which is considered the source region in a scattering problem formulation and its strength is specified by the r.h.s. of Eq. (4.15). A zero Neumann boundary condition is imposed on the left border of the solution domain to simulate the symmetry axis and a zero Dirichlet boundary condition is imposed on the other three borders to simulate the open boundaries of an infinite domain. The basic requirement for using a zero Dirichlet boundary condition is that the size of the solution domain must be large enough so that the boundary reflections are negligible. We also have an additional requirement that the duration of the excitation signal must be long enough so

that the peak of the scattered field (in time domain) is detectable. However, if the size of the solution domain is too large, the finite element mesh could be too coarse to obtain good numerical results considering the limitation of available computer resources. Thus, attention must be paid concerning the choice of the solution domain so that all these requirements can be satisfied. A trial and error approach, although cumbersome and time-consuming, is often best for optimizing the mesh design. Our final mesh includes 6517 nodes and 12778 triangular elements as shown in Figure 4.4 (Middle and Right). In addition, we employ a denser mesh and higher order elements (quadratic elements) in the vicinity of the anomaly (shadowed area) to enhance the accuracy of the solution. Using a PC equipped with a 2.2 GHz Pentium®IV CPU and 1 GB physical memory, the major computational burden is the huge memory consumption when the time-stepping algorithm is used.

4.2.2 Numerical Results

A comparison between the time domain scattered field $v_s(\mathbf{0}, t)$ and the fictitious time domain response $u_s(\mathbf{0}, t)$ was carried out for the $n = 2$ case to highlight the mapping property of the Q-transform. Figure 4.5 shows agreement between the (numerical) solution of the diffusion problem (Eq. (4.29)) and the numerically computed Q-transform of the (numerical) solution of the wave propagation problem (Eq. (4.30)). Moreover, the peak of the time domain response (the observable quantity $v_s(\mathbf{0}, t)$) is very close (within 2.3%) to the theoretical value of 0.009s predicted by Eq. (4.26). This confirms that $|\mathbf{x}_0|$ can be estimated using Eq. (4.28) once the peak position has been determined from the measured waveform $v_s(\mathbf{0}, t)$. The numerical solutions of

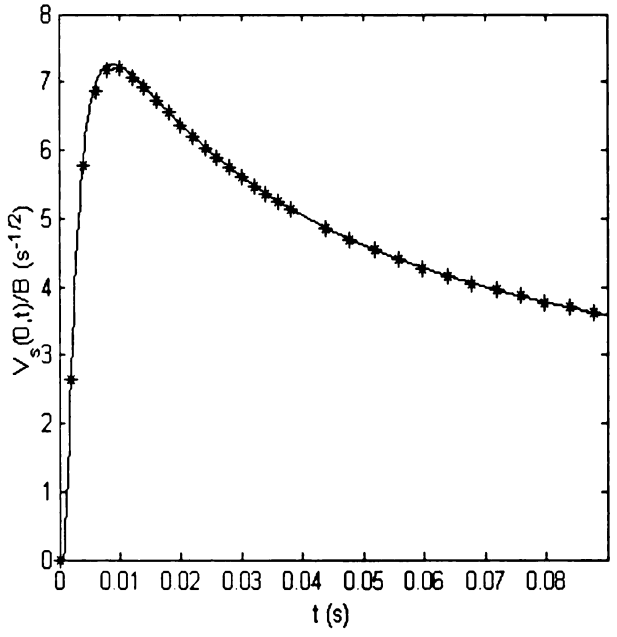

Figure 4.5: The plot of $v_s(\mathbf{0}, t)$ (solid) together with the plot of $Q\{u_s(\mathbf{0}, t)\}$ (*). The predicted peak position is at $t = 0.009\ s$

diffusion equation problem are presented together with the corresponding analytical solutions (see Eq. (4.25)) for cases $n = 1$ and $n = 2$ in Figure 4.6 - 4.7, respectively.

Two major sources of error are of concern. One is caused by the finite duration of the excitation signal while the other results from the Born approximation.

We know that the duration τ of an excitation signal cannot be infinite long in numerical simulation. Hence, we need to determine the minimum value (τ_{min}) of τ such that the error caused by truncation of the signal is negligible. Since the Q-transform is a linear operation, the scattered field $v_s'(\mathbf{0}, t)$ resulting from a truncated excitation signal is (for $n = 1$) (see Eq. (4.25) in section 4.1.3)

$$\begin{aligned} v_s'(\mathbf{0}, t)/B &= \frac{q_f}{2\sqrt{\pi t^3}} \exp\left(-\frac{q_f^2}{4t}\right) - \frac{(1+\lambda)\, q_f}{2\sqrt{\pi t^3}} \exp\left(-\frac{(1+\lambda)^2 q_f^2}{4t}\right) \\ &= \frac{q_f}{2\sqrt{\pi t^3}} \exp\left(-\frac{q_f^2}{4t}\right) \left[1 - (1+\lambda) \exp\left(-\frac{(2\lambda+\lambda^2)\, q_f^2}{4t}\right)\right], \end{aligned} \quad (4.33)$$

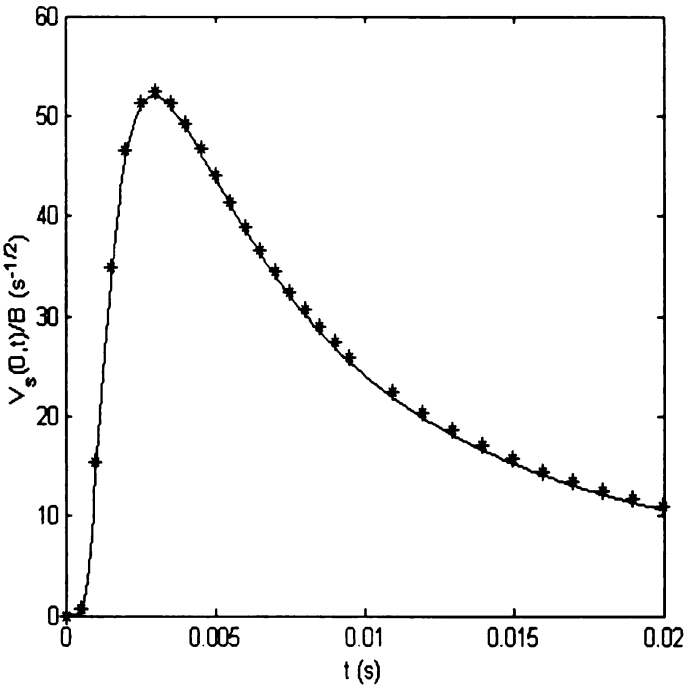

Figure 4.6: The plot of $v_s(\mathbf{0}, t)$ (*) together with the plot of the approximate response (solid). case $n = 1$

where λ is defined as the truncation constant:

$$\lambda \hat{=} \tau / q_f. \tag{4.34}$$

It can be show that, at the point $t = t_{max} = q_f^2/6$, the ratio of $v_s'(\mathbf{0}, t_{max})$ and $v_s(\mathbf{0}, t_{max})$ is

$$1 - \zeta_1 = v_s'(\mathbf{0}, t_{max}) / v_s(\mathbf{0}, t_{max}) = 1 - (1 + \lambda) \exp\left(-\frac{3\lambda^2 + 6\lambda}{2}\right). \tag{4.35}$$

Accordingly, we can show that the relative error ζ_1 with respect to the peak value is less than 1% if the truncation constant $\lambda \geq 1.14$, which yields $\tau_{min} = 1.14 q_f$.

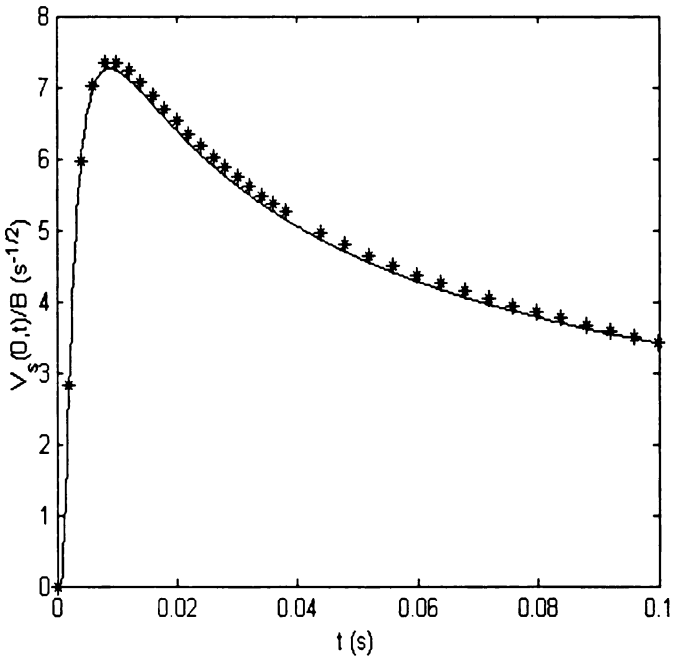

Figure 4.7: The plot of $v_s(\mathbf{0}, t)$ (*) together with the plot of the approximate response (solid). case $n = 2$

Similarly, for $n = 2$, we have

$$\begin{aligned} v_s'(\mathbf{0}, t)/B &= \frac{2}{\sqrt{\pi t}} \exp\left(-\frac{q_f^2}{4t}\right) - \frac{2}{\sqrt{\pi t}} \exp\left(-\frac{(1+\lambda)^2 q_f^2}{4t}\right) \\ &= \frac{2}{\sqrt{\pi t}} \exp\left(-\frac{q_f^2}{4t}\right) \left[1 - \exp\left(-\frac{(2\lambda + \lambda^2) q_f^2}{4t}\right)\right] \end{aligned} \tag{4.36}$$

$$1 - \zeta_2 = v_s'(\mathbf{0}, t_{max}) / v_s(\mathbf{0}, t_{max}) = 1 - \exp\left(-\frac{\lambda^2 + 2\lambda}{2}\right) \tag{4.37}$$

and the relative error ζ_2 with respect to the peak value is less than 1% if $\lambda \geq 2.20$, or $\tau_{min} = 2.20 q_f$. The effect of the truncation of the excitation signal is shown in Figure 4.8 and the relative errors with respect to the peak value are plotted in Figure 4.9 (Left). The error with respect to peak position has been calculated numerically and presented in Figure 4.9 (Right). We notice that the relative errors with respect to

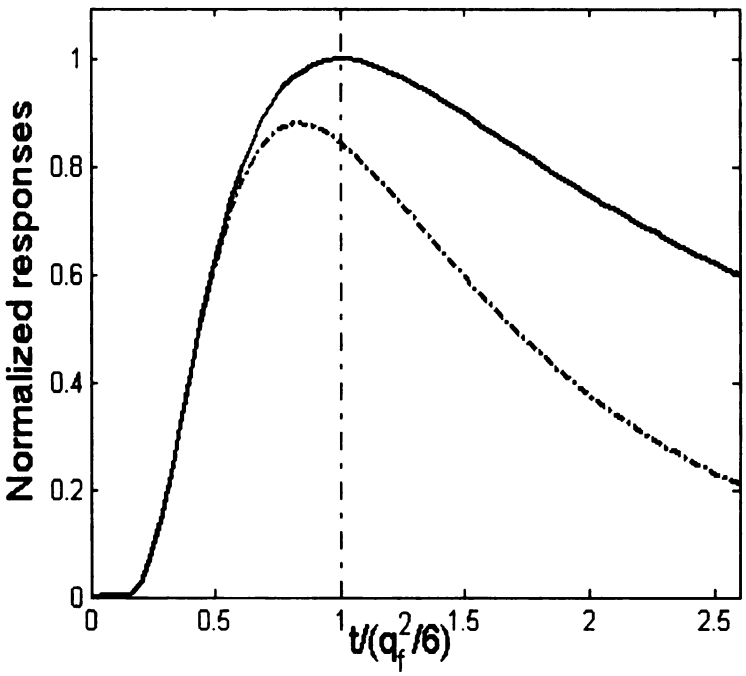

Figure 4.8: Shifting effect of truncation on excitation signal, $q_f = 0.15$. Both ideal response $v_s(\mathbf{0}, t)$ (solid) and shifted response $v_s'(\mathbf{0}, t)$ (dashed) are normalized.

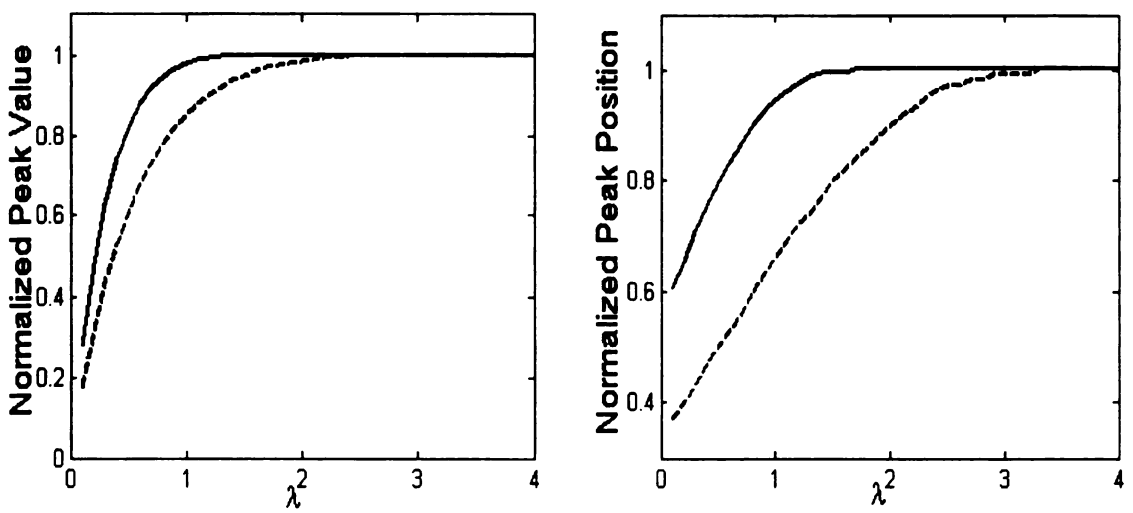

Figure 4.9: Truncation error. Left: Relative error with respect to peak value, $n = 1$ (solid line) and $n = 2$ (dashed line); Right: Relative error with respect to peak position, $n = 1$ (solid line) and $n = 2$ (dashed line)

both the peak value and peak position decrease with increasing λ.

The Born approximation was invoked to obtain Eq. (4.16) and the related inversion formula (4.28). We notice that, if $q_i = 0$, the relative error caused by Born approximation depends only on two dimensionless parameters: $\gamma \hat{=} R/d$ and the contrast χ. In Figure 4.10 and Figure 4.11, we show numerically calculated relative errors with respect to peak value and peak positions using dimensionless coordinates $\mathbf{x}'$ and t' defined by $\mathbf{x}' = \mathbf{x}/|\mathbf{x}_0|$ and $t' = t/T$, where $T \hat{=} (|\mathbf{x}_0|/c_0)^2$, respectively. The value of contrast used in Figure 4.10 is $\chi = -0.25$ while that of Figure 4.11 is $\chi = -0.99$. These values of contrast have been chosen because they are representative of the range of interest, which is the interval from -1 (perfectly insulating anomaly) to 0 (no anomaly). Our results show that the error in the estimate given by Eq. (4.28) is very small for $\gamma \leq 0.1$ and the relative error grows faster than a linear rate for larger values of γ. Also, the relative errors on both peak value and peak position are larger for higher contrast.

4.3 A Vector Diffusion Equation Problem

Most of ECT problems are governed by the vector diffusion equations. The treatment for vector diffusion problem has been developed in [32]. Numerical validation results and additional analysis can be found in [35].

Let us consider the reference problem solved in sections 4.1-4.2. Keeping the same material properties, the electromagnetic field generated, under quasi-magnetostatic

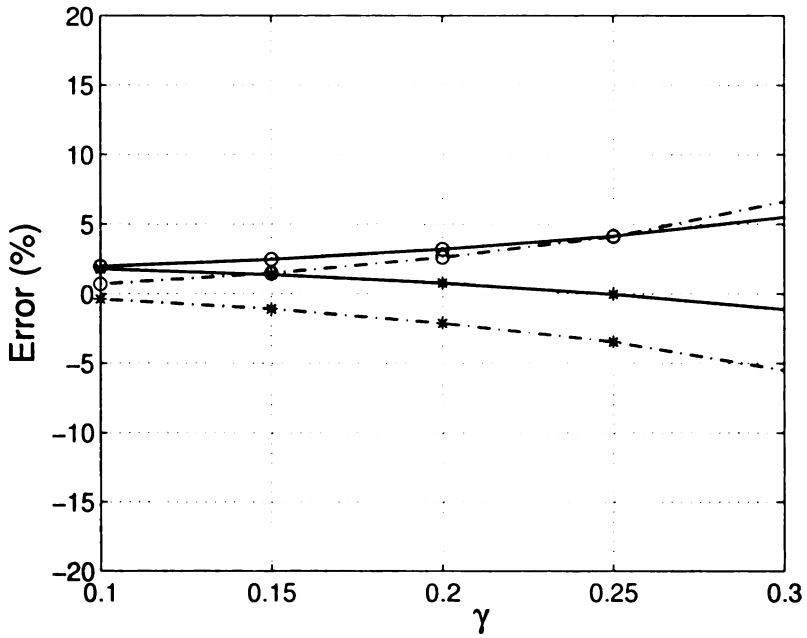

Figure 4.10: Error in the predicted position (*) and amplitude (o) of the peak as function of γ for $n = 1$ (dashed line) and $n = 2$ (solid line), respectively. Case $\chi = -0.25$.

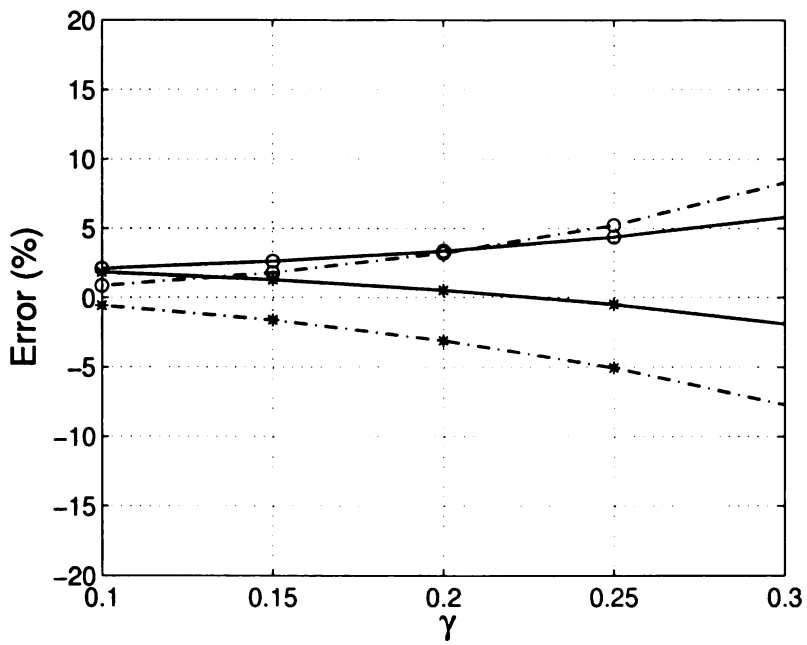

Figure 4.11: Error in the predicted position (*) and amplitude (o) of the peak as function of γ for $n = 1$ (dashed line) and $n = 2$ (solid line), respectively. Case $\chi = -0.99$.

approximation, in the form of the Maxwell's equations, is given by:

$$\nabla \times \mathbf{E} = -\mu \partial_t \mathbf{H} \quad \text{in } \Omega \tag{4.38}$$

$$\nabla \times \mathbf{H} = \mathbf{J}_0 + \sigma \mathbf{E} \quad \text{in } \Omega \tag{4.39}$$

$$\mathbf{H}(\mathbf{x}, t = 0) = \mathbf{0} \quad \text{in } \Omega \tag{4.40}$$

$$\mathbf{E}(|\mathbf{x}| \to \infty, t) = \mathbf{0} \tag{4.41}$$

where the domain $\Omega = \Re^3$ is enclosed by surface $\partial\Omega$ and $\hat{\mathbf{n}}$ is the outward normal on surface $\partial\Omega$. Additionally, the boundary condition (4.41) is equivalent to the radiation condition at infinity. Accordingly, a fictitious wave problem

$$\nabla \times \mathbf{e} = -\mu \partial_q \mathbf{h} \quad \text{in } \Omega \tag{4.42}$$

$$\nabla \times \mathbf{h} = \mathbf{j}_0 + \sigma \partial_q \mathbf{e} \quad \text{in } \Omega \tag{4.43}$$

$$\mathbf{h}(\mathbf{x}, q = 0) = \mathbf{0} \quad \text{in } \Omega \tag{4.44}$$

$$\mathbf{e}(\mathbf{x}, q = 0) = \mathbf{0} \quad \text{in } \Omega \tag{4.45}$$

$$\mathbf{e}(|\mathbf{x}| \to \infty, q) = \mathbf{0} \tag{4.46}$$

can be established to fulfill

$$\mathbf{E}(\mathbf{x}, t) = Q\{\partial_q \mathbf{e}(\mathbf{x}, q)\}(t) \tag{4.47}$$

$$\mathbf{H}(\mathbf{x}, t) = Q\{\mathbf{h}(\mathbf{x}, q)\}(t) \tag{4.48}$$

if the source terms satisfy

$$\mathbf{J}_0(\mathbf{x},t) = Q\{\mathbf{j}_0(\mathbf{x},q)\}(t). \tag{4.49}$$

For our fictitious time domain problem (Eq. (4.42)-(4.46)), we assume for a point source, a magnetic dipole $m(q)$, placed at the origin of the coordinate system and oriented along the z-direction. Again, we choose our measurable quantity for this problem as the scattered field evaluated at the origin. The governing equations for the scattered fields are given by:

$$\nabla \times \mathbf{e}_s = -\mu \partial_q \mathbf{h}_s \quad \text{in } \Omega \tag{4.50}$$

$$\nabla \times \mathbf{h}_s = \mathbf{j}_s + \sigma_0 \partial_q \mathbf{e}_s \quad \text{in } \Omega \tag{4.51}$$

$$\mathbf{h}_s(\mathbf{x}, q=0) = \mathbf{0} \quad \text{in } \Omega \tag{4.52}$$

$$\mathbf{e}_s(\mathbf{x}, q=0) = \mathbf{0} \quad \text{in } \Omega \tag{4.53}$$

$$\mathbf{e}_s(|\mathbf{x}| \to \infty, q) = \mathbf{0} \tag{4.54}$$

where

$$\mathbf{j}_s = \sigma_0 \chi \partial_q \mathbf{e} \tag{4.55}$$

is the source term. By using the linear Born approximation for a small anomaly, the source $\mathbf{j}_s$ can be treated as an electric dipole located at $\mathbf{x}_0$. Note that $\mathbf{e}$ in Eqs. (4.55) is replaced by $\mathbf{e}_0$ and

$$\mathbf{e}_0(\mathbf{x}_0, q) = -\frac{\mu \sin\theta}{4\pi}\left[\frac{m''(q - d/c_0)}{c_0 d} + \frac{m'(q - d/c_0)}{d^2}\right]\mathbf{i}_\phi \tag{4.56}$$

is the solution of Eq. (4.42)-(4.46) in case of $\sigma = \sigma_0$ and $\mathbf{i}_\phi$ is a direction vector pointed in the circumferential direction with respect to the direction of the magnetic dipole in spherical coordinates (r, θ, ϕ) [38]. We can denote the approximate source as

$$\widetilde{\mathbf{j}}_s = \sigma_0 K \partial_q \mathbf{e}_0 (\mathbf{x}_0, q) . \tag{4.57}$$

Then, we have the scattered field

$$\mathbf{h}_s (\mathbf{0}, q) = \frac{l \sin\theta'}{4\pi} \left[\frac{\widetilde{j}_s' (q - d/c_0)}{c_0 d} + \frac{\widetilde{j}_s (q - d/c_0)}{d^2} \right] \mathbf{i}_{\phi'}, \tag{4.58}$$

where l is the distance between two electric charge and a new spherical coordinate system (r', ϕ', θ') is established with its origin located at $\mathbf{x}_0$. Then, by substituting Eq. (4.57) into Eq. (4.58), we have

$$\mathbf{h}_s (\mathbf{0}, q) = -\frac{\mu_0 \sigma_0 K l \sin\theta \sin\theta'}{(4\pi)^2} \left[\frac{m'''' (q - q_f)}{(c_0 d)^2} + \frac{2m''' (q - q_f)}{c_0 d^3} + \frac{m'' (q - q_f)}{d^4} \right] \mathbf{i}_{\phi'}. \tag{4.59}$$

where $q_f = 2d/c_0$.

Now, we need to determine a suitable choice for $m(q)$ so that the last two terms in the bracket of Eq. (4.59) can be neglected. As proposed in [32], by choosing $m(q)$ proportional to q^4, Eq. (4.59) can be reduced to

$$\mathbf{h}_s (\mathbf{0}, q) = -\frac{\mathbf{i}_{\phi'} \mu_0 \sigma_0 K l \sin\theta \sin\theta'}{(4 c_0 d \pi)^2} H (q - 2d/c_0) . \tag{4.60}$$

Applying the Q-transform to the above equation, we obtain

$$\mathbf{H}_s(\mathbf{0},t) = -\frac{\mathbf{i}_{\phi'}\mu_0\sigma_0 K l \sin\theta \sin\theta'}{(4c_0 d\pi)^2}\frac{1}{\pi t}\exp\left(-\frac{q_f^2}{4t}\right), \tag{4.61}$$

whose maximum value $(2d/c_0)$ is located at $t = q_f^2/2$.

In this chapter, an inversion method based on time-of-flight for diffusive phenomenon has been shown to be effective for detecting anomalies in conductive materials. The design of the excitation waveform is critical in order to estimate the time-of-flight properly. Numerical modeling has made it possible to investigate the limits of validity of the inversion method.

CHAPTER 5

TIME-OF-FLIGHT EXTRACTION FOR HARMONIC DIFFUSIVE FIELDS

Q-transform based time-of-flight extraction techniques can be implemented not only for transient diffusive fields, but also for harmonic cases. In this chapter, in contrast to the inversion methods discussed in chapter 4, the time-of-flight information is estimated from nonlocal measurements first. The TOF extraction scheme is based on a novel approach that involves the removal of the material interface. Apart from 5.2.1, the methods presented in this chapter have been proposed in [36] and numerically validated in [37].

5.1 Time-of-Flight in Harmonic Propagative Fields

In the time domain, time-of-flight for the fictitious field appears as a delay in the measured field at a given field position (local quantity). In the frequency domain, the time-of-flight appears in terms of the factor e^{-jkr}, where $k = \omega/c$ is wave number at frequency ω, c is the wave velocity and r represents distance. Alternatively, the time-of-flight information can also be extracted from the Fourier coefficients (nonlocal measurements) [36]. To introduce this concept, we begin by investigating, in a full electrodynamics sense, the canonical problem of radiation from an infinite current-carrying line embedded in an unbounded homogeneous medium.

Let the current-carrying line be parallel to the z axis and z invariant. We know

that the electric field radiated by the line is given by

$$\mathbf{E}(\mathbf{x}; j\omega) = -\frac{\mu_0 \omega \mathbf{i}_0}{4} H_0^{(2)}(kR), \tag{5.1}$$

where $\mathbf{i}_0 = i_0 \hat{\mathbf{i}}_z$ is the strength of the electric current, $H_0^{(2)}(\cdot)$ is the Hankel function of second kind of zero order and R is the distance from a point $\mathbf{x}$ to the current-carrying line [57]. Since this field is independent of z, the field is given by $\mathbf{E}(\mathbf{x}; j\omega) = \hat{\mathbf{i}}_z E_z(r, \theta; j\omega)$, where the subscript denotes the z component of the field. Also, we denote the projection of current-carrying line on the xy plane as $\mathbf{x}_0(r_0, \theta_0)$. Then, the electric field can be expanded in a Fourier series, which is (the subscript is dropped)

$$E(r, \theta; j\omega) = \sum_{n=-\infty}^{+\infty} E_n(r; j\omega) e^{jn\theta} \tag{5.2}$$

$$E_n(r; j\omega) = -\frac{\mu_0 \omega}{4} H_{|n|}^{(2)}(kr) \left[i_0 J_{|n|}(kr_0) e^{-jn\theta_0} \right], \tag{5.3}$$

where $J_n(\cdot)$ is the nth order Bessel function of the first kind [58].

Using the asymptotic approximations of $H_n^{(2)}(kr)$ and $J_n(kr_0)$ for large arguments ($kr \gg 1, kr_0 \gg 1$), we have [54, 60]

$$H_n^{(2)}(x) = \sqrt{\frac{2}{\pi x}} \exp\left[-j\left(x - n\pi/2 - \pi/4\right)\right] + \mathcal{O}\left(1/\sqrt{x^3}\right) \tag{5.4}$$

$$J_n(x) = \sqrt{\frac{2}{\pi x}} \cos\left(x - n\pi/2 - \pi/4\right) + \mathcal{O}\left(1/\sqrt{x^3}\right). \tag{5.5}$$

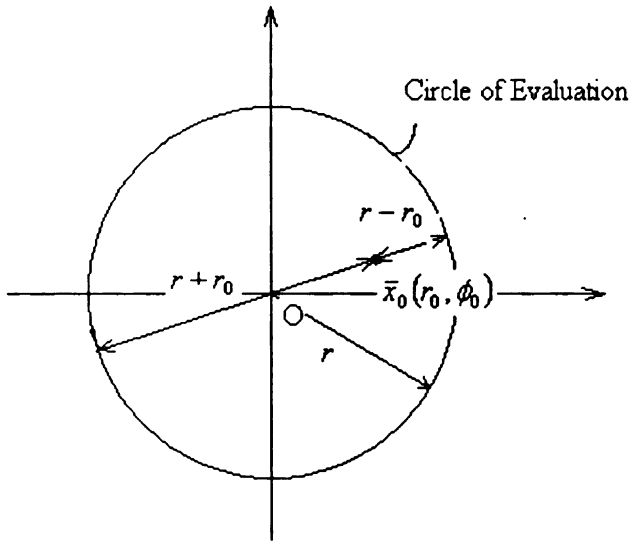

Figure 5.1: Two time-of-flight terms included in the Fourier coefficients

Then, the coefficient $E_n(r; j\omega)$ can be expressed as:

$$\begin{aligned} E_n(r; j\omega) &\cong -\frac{\mu_0 c i_0}{2\pi\sqrt{r r_0}} e^{-j(kr-|n|\pi/2-\pi/4)} \cos(kr_0 - |n|\pi/2 - \pi/4)\, e^{-jn\theta_0} \\ &= -\frac{\mu_0 c i_0}{2\pi\sqrt{r r_0}} \left\{ e^{-jk(r-r_0)} + (-1)^{|n|} j e^{-jk(r+r_0)} \right\} e^{-jn\theta_0}. \end{aligned} \tag{5.6}$$

As shown in Eq. (5.6), the time-of-flight e^{-jkr} found in local measurements is split into two separate terms. One term, $e^{-jk(r-r_0)}$, represents the time-of-flight from the source position $\mathbf{x}_0(r_0, \theta_0)$ to the closest point of the evaluation circle while the other term, $e^{-jk(r+r_0)}$, represents the time-of-flight from the source to the most distant point on the evaluation circle (Figure 5.1).

5.2 A Cylindrical Configuration

In order to illustrate our time-of-flight extraction strategy for harmonic eddy current fields, we take the cylindrical structure shown in Figure 5.2 as our reference

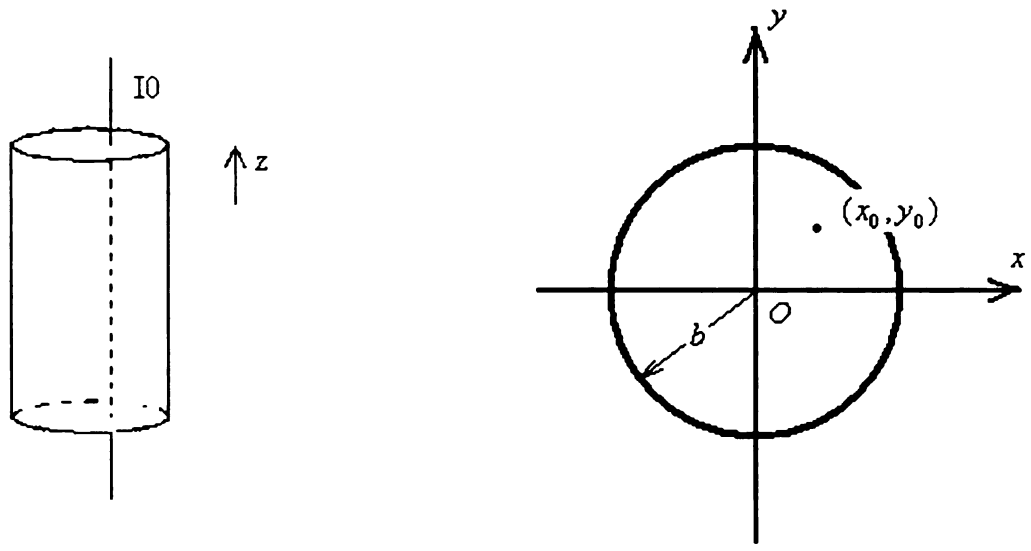

Figure 5.2: Geometry for the reference problem. Left: 3D View; Right: 2D Cross-section at $z = z_0$

problem throughout this chapter. Such cylindrical geometries have been investigated extensively in a variety of disciplines [59, 61].

In this problem, a long conducting cylinder is placed in an unbounded homogeneous non-conducting space. A long current-carrying wire of current intensity I_0 is embedded inside the cylinder. The axes of both the cylinder and the wire are parallel with the z-axis.

We assume that all materials involved are linear, isotropic, non-dispersive and nonmagnetic. Since the displacement current is negligible, the electric field $\mathbf{E}$ satisfies

$$\nabla \times \nabla \times \mathbf{E}(\mathbf{x}; j\omega) + j\omega\mu_0\sigma\mathbf{E}(\mathbf{x}; j\omega) = -j\omega\mu_0\mathbf{J}_0(\mathbf{x}; j\omega), \tag{5.7}$$

where $\mathbf{x} = x\hat{\mathbf{i}}_x + y\hat{\mathbf{i}}_y$ is the position of a point.

Obviously, at the central part of the cylinder, the excited diffusive fields have no z dependency. Thus, we can simplify this three-dimensional problem into a two-

dimensional problem on a cross-section of the cylinder, such as $z = 0$. At this cross-section, the projection of the current-carrying wire is located at (x_0, y_0). The conductivity of the cylinder is $\sigma_0 = 3.57 \times 10^7 S/m$ (pure aluminum).

Now, with $\mathbf{J}_0(\mathbf{x}; j\omega) = J_{0z}(\mathbf{x}; j\omega)\,\hat{\mathbf{i}}_z$ and $\mathbf{E}(\mathbf{x}; j\omega) = E_z(\mathbf{x}; j\omega)\,\hat{\mathbf{i}}_z$, Eq. (5.7) can be reduced to a scalar equation in the form of

$$\nabla^2 E_z(\mathbf{x}; j\omega) - j\omega\mu_0\sigma(\mathbf{x})\,E_z(\mathbf{x}; j\omega) = j\omega\mu_0 J_{0z}(\mathbf{x}; j\omega), \tag{5.8}$$

where $J_{0z}(\mathbf{x}; j\omega) = I_{0z}(\omega)\,\delta(x - x_0)\,\delta(y - y_0)$ and $I_0(\omega)$ is the strength of the imposed current. Furthermore, we can drop the z subscript for simplicity and define the contrast function as $\chi(\mathbf{x}) \equiv \sigma(\mathbf{x})/\sigma_0 - 1$ to obtain:

$$\nabla^2 E(\mathbf{x}; j\omega) - j\omega\mu_0\sigma_0[1 + \chi(\mathbf{x})]\,E(\mathbf{x}; j\omega) = j\omega\mu_0 I_0(\omega)\,\delta(x - x_0)\,\delta(y - y_0). \tag{5.9}$$

As stated in Chapter 2, the boundary conditions on the outer surface of the cylinder are:

$$\hat{\mathbf{n}} \times \mathbf{E}(b^-, \theta; j\omega) = \hat{\mathbf{n}} \times \mathbf{E}(b^+, \theta; j\omega) \tag{5.10}$$

$$\hat{\mathbf{n}} \times \mathbf{H}(b^-, \theta; j\omega) = \hat{\mathbf{n}} \times \mathbf{H}(b^+, \theta; j\omega), \tag{5.11}$$

where $\hat{\mathbf{n}}$ is the outward normal on that surface, superscripts $'-'$ and $'+'$ denote the medium outside and inside the cylinder, respectively. In the cylindrical coordinate

system, the above boundary conditions can be reduced to

$$\partial E\left(b^{-},\theta;j\omega\right)/\partial r = \partial E\left(b^{+},\theta;j\omega\right)/\partial r \tag{5.12}$$

$$E\left(b^{-},\theta;j\omega\right) = E\left(b^{+},\theta;j\omega\right). \tag{5.13}$$

To establish a corresponding fictitious wave equation problem in the frequency domain, let $\widetilde{\omega}$ denote the fictitious frequency domain dependency, we have $E\left(r,\theta;j\omega\right) = Q\left\{\widetilde{E}\left(r,\theta;j\widetilde{\omega}\right)\right\}$. The Q-transform relation in the frequency domain is

$$E\left(r,\theta;j\omega\right) = \widetilde{E}\left(r,\theta;\sqrt{j\widetilde{\omega}}\right), \tag{5.14}$$

which follows from the Laplace transform relation given by Eq. (3.72) in section 3.4.

5.2.1 Solution of the Radiation Problem

In order to understand the relation between fields inside and outside the cylinder, we will solve this radiation problem analytically in the fictitious frequency domain using the method of separation of variables.

The model of this radiation problem is shown in Figure 5.3, where the conductive cylinder ($r \leq b$) and the free space outside the cylinder ($r > b$) is denoted as domain I and II, respectively. The conductivity σ_1 is equal to zero and $\sigma_0 = 3.57 \times 10^7 S/m$. To further simplify the problem, the point source is placed on the x-axis at a distance (relative to the origin) of $r_0 = \sqrt{x_0^2 + y_0^2}$ without loss of generality.

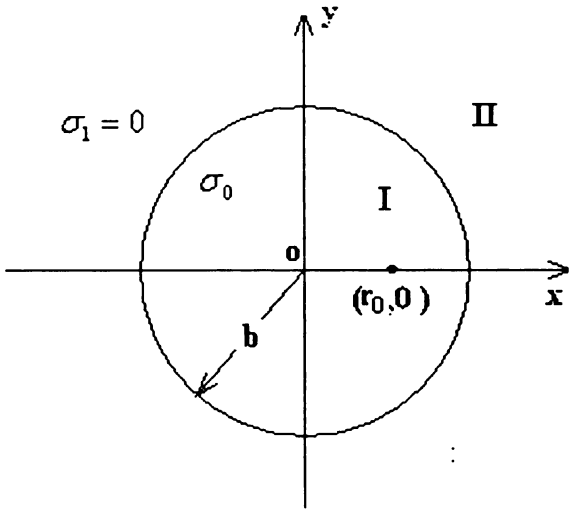

Figure 5.3: Geometry for the Radiation Problem

The governing equations can be written as:

$$\nabla^2 \widetilde{E}(\mathbf{x}; j\widetilde{\omega}) + \widetilde{k}_0^2 \widetilde{E}(\mathbf{x}; j\widetilde{\omega}) = j\widetilde{\omega}\mu_0 \widetilde{J}_i(j\widetilde{\omega}) \quad for \ 0 \le r < b \tag{5.15}$$

$$\nabla^2 \widetilde{E}(\mathbf{x}; j\widetilde{\omega}) = 0 \quad for \ b < r \tag{5.16}$$

$$\partial \widetilde{E}(b^-, \theta; j\widetilde{\omega}) / \partial r = \partial \widetilde{E}(b^+, \theta; j\widetilde{\omega}) / \partial r \tag{5.17}$$

$$\widetilde{E}(b^-, \theta; j\widetilde{\omega}) = \widetilde{E}(b^+, \theta; j\widetilde{\omega}) \tag{5.18}$$

$$\lim_{r \to +\infty} \widetilde{E}(r, \theta; j\widetilde{\omega}) = 0, \tag{5.19}$$

where $\widetilde{J}_i(j\widetilde{\omega}) \equiv \widetilde{I}_0(j\widetilde{\omega})\,\delta(x - x_0)\,\delta(y - y_0)$.

The general solutions of Eqs. (5.15)-(5.19) at an arbitrary evaluation point $\mathbf{x} = (r, \theta)$ are of the form [58]:

$$\widetilde{E}(r, \theta; j\widetilde{\omega}) = \begin{cases} -\dfrac{\mu\widetilde{\omega}\widetilde{I}_i}{4} H_0^{(2)}\left(\widetilde{k}_0 r'\right) + \displaystyle\sum_{n=0}^{+\infty} C_{1,n} \cos(n\theta)\, J_n\left(\widetilde{k}_0 r\right) & r \le b \\ \displaystyle\sum_{n=1}^{+\infty} C_{2,n} \cos(n\theta)\, r^{-n} & r > b \end{cases}, \tag{5.20}$$

where $r' = |\mathbf{x} - \mathbf{x}_0|$, $r = |\mathbf{x}|$, $C_{1,n}$ and $C_{2,n}$ are coefficients of the solutions in domain I and II, respectively.

By incorporating the interface conditions (Eqs. (5.17)-(5.18)) on the circle $r = b$ and using the identity [58],

$$H_0^{(2)}\left(\widetilde{k}_0 r'\right) = \sum_{n=0}^{+\infty} T(n)\, H_n^{(2)}\left(\widetilde{k}_0 r\right) J_n\left(\widetilde{k}_0 r\right) \cos(n\theta), \tag{5.21}$$

with

$$T(n) \equiv \begin{cases} 1 & , n = 0 \\ 2 & , n > 0 \end{cases}. \tag{5.22}$$

The system of equations for $C_{1,n}$ and $C_{2,n}$ is

$$J_n\left(\widetilde{k}_0 b\right) C_{1,n} - b^{-n} C_{2,n} = \frac{\mu_0 \widetilde{\omega} \widetilde{I}_i T(n)}{4} H_n^{(2)}\left(\widetilde{k}_0 b\right) J_n\left(\widetilde{k}_0 a\right) \tag{5.23}$$

$$\dot{J}_n\left(\widetilde{k}_0 b\right) C_{1,n} + \frac{n}{bk} b^{-n} C_{2,n} = \frac{\mu_0 \widetilde{\omega} \widetilde{I}_i T(n)}{4} \dot{H}_n^{(2)}\left(\widetilde{k}_0 b\right) J_n\left(\widetilde{k}_0 a\right). \tag{5.24}$$

The solutions of this system are

$$C_{1,n} = \frac{\mu_0 \widetilde{\omega} T(n)\, \widetilde{I}_i}{4} J_n\left(\widetilde{k}_0 a\right) H_{n-1}^{(2)}\left(\widetilde{k}_0 b\right) / J_{n-1}\left(\widetilde{k}_0 b\right) \quad , n = 0, 1, 2, \ldots \tag{5.25}$$

$$C_{2,n} = -j \frac{T(n)\, \widetilde{I}_i}{2\pi b} \sqrt{\frac{\mu_0}{\sigma_0}} b^n J_n\left(\widetilde{k}_0 a\right) / J_{n-1}\left(\widetilde{k}_0 b\right) \quad , n = 1, 2, \ldots. \tag{5.26}$$

Embedding Eqs. (5.25)-(5.26) into Eq. (5.20), the complete solution can be shown

to be:

$$\widetilde{E}(r,\theta;j\widetilde{\omega}) = \begin{cases} \dfrac{\mu_0\widetilde{\omega}\widetilde{I}_i}{4}\left[-H_0^{(2)}\left(\widetilde{k}_0 r'\right) + \displaystyle\sum_{n=0}^{+\infty} T(n)\,\frac{J_n\left(\widetilde{k}_0 a\right) H_{n-1}^{(2)}\left(\widetilde{k}_0 b\right) J_n\left(\widetilde{k}_0 r\right)}{J_{n-1}\left(\widetilde{k}_0 b\right)}\cos(n\theta)\right] & , r \le b \\ -j\dfrac{\widetilde{I}_i}{2\pi b}\sqrt{\mu_0/\sigma_0}\displaystyle\sum_{n=1}^{+\infty} T(n)\left(\frac{b}{r}\right)^n \frac{J_n\left(\widetilde{k}_0 a\right)}{J_{n-1}\left(\widetilde{k}_0 b\right)}\cos(n\theta) & , r > b \end{cases} \tag{5.27}$$

Identities used to manipulate the Bessel functions are [54]

$$\dot{Z}_n(z) = \frac{1}{2}\left[Z_{n-1}(z) - Z_{n+1}(z)\right],$$

$$Z_{-n}(z) = (-1)^n Z_n(z),$$

$$\dot{Z}_0(z) = -Z_1(z),$$

$$\dot{Z}_n(z) = Z_{n-1}(z) - \frac{n}{z}Z_n(z),$$

$$J_n(z)\,\dot{H}_n^{(2)}(z) - \dot{J}_n(z)\,H_n^{(2)}(z) = -\frac{2i}{\pi z},$$

where $Z_n(z)$ can be any of the Bessel functions $J_n(z)$, $Y_n(z)$, $H_n^{(1)}(z)$ and $H_n^{(2)}(z)$.

The analytical solution given by Eq. (5.27) can be obtained in another way. Let us consider a generalized case of a nonzero conductivity σ_1 in the region outside the conductive cylinder. In this situation, the general solution in domain II satisfies the Helmholtz equation instead of the Laplace equation since the radiated field exists in

that domain. The general solution then has the form:

$$\widetilde{E}(r,\theta;j\widetilde{\omega}) = \begin{cases} -\frac{\mu\widetilde{\omega}\widetilde{I}_i}{4}H_0^{(2)}\left(\widetilde{k}_0 r'\right) + \sum_{n=0}^{+\infty} C_{1,n}\cos(n\theta)\,J_n\left(\widetilde{k}_0 r\right) & r \le b \\ \sum_{n=1}^{+\infty} C_{2,n}\cos(n\theta)\,H_0^{(2)}\left(\widetilde{k}_1 r\right) & r > b \end{cases}, \quad (5.28)$$

where $\widetilde{k}_1 = \widetilde{\omega}\sqrt{\mu_0\sigma_1}$. Imposing the same interface conditions (Eqs. (5.17)-(5.18)) as previously, the equations for solving the coefficients are

$$J_n\left(\widetilde{k}_0 b\right)C_{1,n} - b^{-n}C_{2,n} = \frac{\mu_0\widetilde{\omega}T(n)\,\widetilde{I}_i}{4}H_n^{(2)}\left(\widetilde{k}_0 b\right)J_n\left(\widetilde{k}_0 a\right) \quad (5.29)$$

$$\dot{J}_n\left(\widetilde{k}_0 b\right)C_{1,n} + \frac{n}{bk}b^{-n}C_{2,n} = \frac{\mu_0\widetilde{\omega}T(n)\,\widetilde{I}_i}{4}\dot{H}_n^{(2)}\left(\widetilde{k}_0 b\right)J_n\left(\widetilde{k}_0 a\right). \quad (5.30)$$

The coefficients are obtained as

$$C_{1,n} = \frac{j\mu_0\widetilde{\omega}J_n\left(\widetilde{k}_0 a\right)T(n)\,\widetilde{I}_i}{4}\frac{\widetilde{k}_1 H_n^{(2)}\left(\widetilde{k}_0 b\right)H_{n-1}^{(2)}\left(\widetilde{k}_1 b\right) - \widetilde{k}_0 H_{n-1}^{(2)}\left(\widetilde{k}_0 b\right)H_n^{(2)}\left(\widetilde{k}_1 b\right)}{\widetilde{k}_1 J_n\left(\widetilde{k}_0 b\right)H_{n-1}^{(2)}\left(\widetilde{k}_1 b\right) - \widetilde{k}_0 J_{n-1}\left(\widetilde{k}_0 b\right)H_n^{(2)}\left(\widetilde{k}_1 b\right)} \quad (5.31)$$

$$C_{2,n} = \frac{j\mu_0\widetilde{\omega}J_n\left(\widetilde{k}_0 a\right)T(n)\,\widetilde{I}_i}{2\pi b}\frac{1}{\widetilde{k}_1 J_n\left(\widetilde{k}_0 b\right)H_{n-1}^{(2)}\left(\widetilde{k}_1 b\right) - \widetilde{k}_0 J_{n-1}\left(\widetilde{k}_0 b\right)H_n^{(2)}\left(\widetilde{k}_1 b\right)} \quad (5.32)$$

If conductivity σ_1 goes to zero, the combination of the coefficients $C_{1,n}$ and $C_{2,n}$ with Eq. (5.28) is shown to be identical with Eq. (5.27). The result makes use of following asymptotic relations:

$$H_n^{(2)}(x) \xrightarrow{x\to 0} j\left(\frac{2}{x}\right)^n \frac{\Gamma(n)}{\pi} \quad , n > 0 \quad (5.33)$$

$$H_n^{(2)}(x) \xrightarrow{x\to 0} j\left(\frac{2}{\pi}\right)\ln\frac{2}{x} \quad , n = 0 \quad (5.34)$$

and the formulas

$$\frac{H_n^{(2)}\left(\widetilde{k}_1 r\right)}{H_n^{(2)}\left(\widetilde{k}_1 b\right)} \xrightarrow{\widetilde{k}_1 \to 0} \left[j\left(\frac{2}{\widetilde{k}_1 r}\right)^n \frac{\Gamma(n)}{\pi}\right] / \left[j\left(\frac{2}{\widetilde{k}_1 b}\right)^n \frac{\Gamma(n)}{\pi}\right] = \left(\frac{b}{r}\right)^n \quad , n > 0 \quad (5.35)$$

$$\frac{H_0^{(2)}\left(\widetilde{k}_1 r\right)}{H_0^{(2)}\left(\widetilde{k}_1 b\right)} \xrightarrow{\widetilde{k}_1 \to 0} \left[j\left(\frac{2}{\pi}\right) \ln \frac{2}{\widetilde{k}_1 r}\right] / \left[j\left(\frac{2}{\pi}\right) \ln \frac{2}{\widetilde{k}_1 b}\right] = 1 = \left(\frac{b}{r}\right)^0 \quad , n = 0. \quad (5.36)$$

5.2.2 Time-of-Flight and the Solution of the Radiation Problem

In order to understand how the time-of-flight information is embedded in the solution of the radiation problem, we modify Eq. (5.27) slightly, to introduce the source at position $\mathbf{x} = (r_0, \theta_0)$ and replace $\cos(\cdot)$ function with an exponential function. Thus, the solution of the radiation problem can be rewritten in the form of:

$$\widetilde{E}(r, \theta; j\widetilde{\omega}) = \begin{cases} -\frac{\mu_0 \widetilde{\omega} \widetilde{I}_i}{4} H_0^{(2)}\left(\widetilde{k}_0 r'\right) + \sum_{n=-\infty}^{+\infty} \widetilde{E}_n^s(r; j\widetilde{\omega})\, e^{jn\theta} & , r \le b \\ \sum_{n=-\infty, n\neq 0}^{+\infty} \widetilde{E}_n(r; j\widetilde{\omega})\, e^{jn\theta} & , r \ge b \end{cases}, \quad (5.37)$$

where the angular Fourier coefficients $\widetilde{E}_n(r; j\widetilde{\omega})$ and $\widetilde{E}_n^s(r; j\widetilde{\omega})$ are

$$\widetilde{E}_n^s(r; j\widetilde{\omega}) = \frac{\mu_0 \widetilde{\omega}}{4}\left[\widetilde{I}_i J_{|n|}\left(\widetilde{k}_0 r_0\right) e^{-jn\theta_0}\right] J_{|n|}\left(\widetilde{k}_0 r\right) \frac{H_{|n|-1}^{(2)}\left(\widetilde{k}_0 b\right)}{J_{|n|-1}\left(\widetilde{k}_0 b\right)} \quad (5.38)$$

$$\widetilde{E}_n(r; j\widetilde{\omega}) = -j\frac{\mu_0 c_0}{2\pi b}\left(\frac{b}{r}\right)^{|n|}\left[\widetilde{I}_i J_{|n|}\left(\widetilde{k}_0 r_0\right) e^{-jn\theta_0}\right] \frac{1}{J_{|n|-1}\left(\widetilde{k}_0 b\right)}. \quad (5.39)$$

If the evaluation circle is coincident with the surface of the cylinder, i.e. $r = b$,

the coefficients can be expressed as:

$$\widetilde{E}_n^s(b;j\widetilde{\omega}) = \frac{\mu_0\widetilde{\omega}\widetilde{I}_i}{4} D_n(j\widetilde{\omega})\, F_n(j\widetilde{\omega})\, e^{-jn\theta_0} \tag{5.40}$$

$$\widetilde{E}_n(b;j\widetilde{\omega}) = -j\frac{\mu_0 c_0 \widetilde{I}_i}{2\pi b}\left(\frac{b}{r}\right)^{|n|} G_n(j\widetilde{\omega})\, e^{-jn\theta_0}, \tag{5.41}$$

where

$$D_n(j\widetilde{\omega}) = J_{|n|}\left(\widetilde{k}_0 r_0\right) H^{(2)}_{|n|-1}\left(\widetilde{k}_0 b\right) \tag{5.42}$$

$$F_n(j\widetilde{\omega}) = J_{|n|}\left(\widetilde{k}_0 b\right) / J_{|n|-1}\left(\widetilde{k}_0 b\right) \tag{5.43}$$

$$G_n(j\widetilde{\omega}) = J_{|n|}\left(\widetilde{k}_0 r_0\right) / J_{|n|-1}\left(\widetilde{k}_0 b\right). \tag{5.44}$$

As proposed by Tamburrino [36], we can apply Eqs. (5.4) and (5.5) to Eqs. (5.42)-(5.44) to show

$$D_n(j\widetilde{\omega}) = \frac{1}{\pi\widetilde{k}_0\sqrt{br_0}}\left[e^{-j\widetilde{k}_0(b-r_0)} + (-1)^{|n|} j e^{-j\widetilde{k}_0(b+r_0)}\right] e^{-jn\theta_0} \tag{5.45}$$

$$F_n(j\widetilde{\omega}) = -j\sqrt{\frac{b}{r_0}}\frac{1+e^{-2j\left(\widetilde{k}_0 r_0 - |n|\pi/2 - \pi/4\right)}}{1+e^{-2j\left(\widetilde{k}_0 r_0 - |n|\pi/2 + \pi/4\right)}} e^{-j\widetilde{k}_0(b-r_0)} \tag{5.46}$$

$$G_n(j\widetilde{\omega}) = -j\sqrt{\frac{b}{r_0}}\frac{1+e^{-2j\left(\widetilde{k}_0 r_0 - |n|\pi/2 - \pi/4\right)}}{1+e^{-2j\left(\widetilde{k}_0 r_0 - |n|\pi/2 + \pi/4\right)}}. \tag{5.47}$$

Notice that Eq. (5.45) is analogous to Eq. (5.6) that includes explicit time-of-flight terms and $F_n(j\widetilde{\omega})$, $G_n(j\widetilde{\omega})$ are periodic distributions of the frequency $\widetilde{\omega}$ that can be expanded in term of a Fourier series. Furthermore, it was shown that such an expansion reveals the existence of the time-of-flight term of type $(b - r_0 + 2mb)/c_0$ and $(b + r_0 + 2mb)/c_0$ in $F_n(j\widetilde{\omega})$, where m is a nonnegative integer. These kinds of

time-of-flight terms represents the multiple reflections of the fictitious waves on the interface $r = b$.

5.3 Interface Removal and Time-of-Flight Estimation

The time-of-flight terms identified in the solution of the radiation problem (Eqs. (5.37)-(5.39)) are complex due to the multiple reflections from the boundary of the conductive cylinder. In contrast, the fictitious field $\widetilde{V}(\mathbf{x}; j\widetilde{\omega})$ radiated from a point source embedded in an unbounded homogeneous medium given by,

$$\widetilde{V}(\mathbf{x}; j\widetilde{\omega}) = -\frac{\mu_0 \widetilde{\omega} \widetilde{I}_i}{4} H_0^{(2)}\left(\widetilde{k}_0 |\mathbf{x} - \mathbf{x}_0|\right) \tag{5.48}$$

is related in a simple way to time-of-flight $|\mathbf{x} - \mathbf{x}_0| / c_0$, which is in turn related to the distance between the evaluation point $\mathbf{x} = \mathbf{x}(r, \theta)$ and the source location $\mathbf{x}_0 = \mathbf{x}(r_0, \theta_0)$. Therefore, we need a procedure for removing the effect of the material discontinuity and to cast the TOF extraction issue in terms of TOF estimation from a "simple" field given by Eq. 5.48 (see [36]).

5.3.1 Interface Removal Using Linear Filtering

To find the linkage between the fictitious field $\widetilde{V}(\mathbf{x}; j\widetilde{\omega})$ and $\widetilde{E}(\mathbf{x}; j\widetilde{\omega})$, we represent $\widetilde{V}(\mathbf{x}; j\widetilde{\omega})$ in a Fourier series

$$\widetilde{V}(r, \theta; j\widetilde{\omega}) = \sum_{n=-\infty}^{+\infty} \widetilde{V}_n(r; j\widetilde{\omega}) e^{jn\theta}, \tag{5.49}$$

$$\widetilde{V}_n(r;j\widetilde{\omega}) = -\frac{\mu_0\widetilde{\omega}}{4}H^{(2)}_{|n|}\left(\widetilde{k}_0 r\right)\left[\widetilde{I}_i J_{|n|}\left(\widetilde{k}_0 r_0\right)e^{-jn\theta_0}\right]. \tag{5.50}$$

Let us write Eq. (5.39) in form of

$$\widetilde{E}_n(r;j\widetilde{\omega}) = -j\frac{\mu_0 c_0}{2\pi b}\left(\frac{b}{r}\right)^{|n|}\frac{1}{J_{|n|-1}\left(\widetilde{k}_0 b\right)}\left[\widetilde{I}_i J_{|n|}\left(\widetilde{k}_0 r_0\right)e^{-jn\theta_0}\right], \quad r \geq b, \tag{5.51}$$

where an additional term for case of $n = 0$ is added to original equation for convenience of mathematical manipulations. Therefore, for $r \geq b$

$$\begin{aligned}\widetilde{V}_n(r;j\widetilde{\omega}) &= \left[-j\widetilde{k}_0\frac{\pi b}{2}\left(\frac{r}{b}\right)^{|n|}H^{(2)}_{|n|}\left(\widetilde{k}_0 r\right)J_{|n|-1}\left(\widetilde{k}_0 b\right)\right]\widetilde{E}_n(r;j\widetilde{\omega}) \\ &= \left[-j\widetilde{k}_0\frac{\pi b}{2}\left(\frac{r'}{b}\right)^{|n|}H^{(2)}_{|n|}\left(\widetilde{k}_0 r\right)J_{|n|-1}\left(\widetilde{k}_0 b\right)\right]\widetilde{E}_n(r';j\widetilde{\omega}),\end{aligned} \tag{5.52}$$

where $r' \geq b$ is the radius of the evaluation circle. Thus, by substituting Eq. (5.52) into Eq. (5.49) and invoking the following expression

$$\widetilde{E}_n(r';j\widetilde{\omega}) = \frac{1}{2\pi}\int_0^{2\pi}\widetilde{E}(r',\theta';j\widetilde{\omega})\,e^{-jn\theta'}d\theta', \tag{5.53}$$

we have

$$\begin{aligned}\widetilde{V}(r,\theta;j\widetilde{\omega}) &= -\frac{j\widetilde{k}_0 b}{4}\int_0^{2\pi}\left[\sum_{n=-\infty}^{+\infty}\left(\frac{r'}{b}\right)^{|n|}H^{(2)}_{|n|}\left(\widetilde{k}_0 r\right)J_{|n|-1}\left(\widetilde{k}_0 b\right)e^{jn(\theta-\theta')}\right] \\ &\quad\cdot\widetilde{E}(r',\theta';j\widetilde{\omega})\,d\theta'.\end{aligned} \tag{5.54}$$

The transform relation given above is a linear filtering process that maps the measurement $\widetilde{E}(r',\theta';j\widetilde{\omega})$ taken on a circle of radius r' onto the field $\widetilde{V}(r,\theta;j\widetilde{\omega})$ evaluated on a circle of radius r. The linear filter involved is stable for $r' > r$ [36]. By further

investigating the linearity of this transform, we can expand the field radiated from a point source to that of a line or a surface source. Therefore, this linear filtering method for interface removing could also be applied to more realistic defects of finite dimensions [37].

5.3.2 Time-of-Flight Estimation in the Frequency Domain

The corresponding linear filter for solutions of diffusion equation problems can be obtained using the Q-transform. If $E = Q\left\{\widetilde{E}\right\}$ and $V = Q\left\{\widetilde{V}\right\}$, we have

$$E(\mathbf{x}; j\omega) = \widetilde{E}\left(\mathbf{x}, \sqrt{j\omega}\right), \tag{5.55}$$

which is equivalent to replacing $\widetilde{\omega}$ in solutions of fictitious wave equations with $\sqrt{\omega/j}$ in solutions of diffusion equations. Thus, we obtain

$$\begin{aligned} V(r,\theta; j\omega) &= -\frac{b\sqrt{j\omega}}{4c_0}\int_0^{2\pi}\left[\sum_{n=-\infty}^{+\infty}\left(\frac{r'}{b}\right)^{|n|} H_{|n|}^{(2)}\left(\frac{\sqrt{\omega}}{\sqrt{j}c_0}r\right) J_{|n|-1}\left(\frac{\sqrt{\omega}}{\sqrt{j}c_0}b\right) e^{jn(\theta-\theta')}\right] \\ &\quad \cdot E(r',\theta'; j\omega)\, d\theta'. \end{aligned} \tag{5.56}$$

Also, from Eq. (5.48), we have

$$V(r,\theta; j\omega) = -\frac{\mu_0\sqrt{\omega} I_i(j\omega)}{4\sqrt{j}} H_0^{(2)}\left(\sqrt{\frac{\omega}{j}}\frac{|\mathbf{x}-\mathbf{x}_0|}{c_0}\right) \tag{5.57}$$

and in case of $k_0|\mathbf{x}-\mathbf{x}_0| \gg 1$,

$$V(r,\theta; j\omega) \cong -\frac{\mu_0 \sqrt[4]{j\omega} I_i(j\omega)}{4}\sqrt{\frac{c_0}{\pi|\mathbf{x}-\mathbf{x}_0|}}\exp\left(-\frac{\sqrt{j\omega}|\mathbf{x}-\mathbf{x}_0|}{c_0}\right). \tag{5.58}$$

In practical situations, we have noisy measurements $E_{meas} = E + \Delta E$, where ΔE is the noise term. The associated noisy field $V_{meas} = V + \Delta V$ can be obtained with Eq. (5.56). The estimation of the time-of-flight term $q_{TOF} = |\mathbf{x} - \mathbf{x}_0| / c_0$ can be achieved by solving the one parameter minimization problem:

$$q_{TOF} = \underset{q^*}{\operatorname{argmin}} \left| -\frac{\mu_0 \sqrt{\omega} I_i}{4\sqrt{j}} H_0^{(2)} \left(\sqrt{\frac{\omega}{j}} q \right) - V_{meas}(r^*, \theta^*; j\omega) \right|, \tag{5.59}$$

where (r^*, θ^*) is a given observation point and q^* is the estimate of q_{TOF}.

The estimation scheme can be summarized as follows:

1. Measure the data $E_{meas}(r', \theta'; j\omega)$ for a fixed r' and $0 \leq \theta' < 2\pi$;

2. Convert $E_{meas}(r', \theta'; j\omega)$ into $V_{meas}(r_k, \theta_k; j\omega)$, where (r_k, θ_k) is the k-th observation point. Repeat this step for $k = 1, \ldots, N_T$, where N_T is the number of observation points;

3. Estimate q_k^* by solving the minimization problem (Eq. (5.59)) for $(r^*, \theta^*) = (r_k, \theta_k)$, Repeat for $k = 1, \ldots, N_T$;

4. Calculate the distance $d_k = c_0 q_k^*$ from the observation point (r_k, θ_k) to locate the source

It is worth pointing out that the evaluation of filter coefficient through Eq. (5.56) can be expedited using the Fast Fourier transform (FFT) if the sampling points (r', θ') are uniformly distributed on the circle $r = r'$, which means $\theta'_k = 2\pi k / N_T$ for $k = 0, \ldots, N_T - 1$. On the other hand, the one parameter minimization problem is formulated under the assumption that the source strength $I_i(j\omega)$ is known. Other-

wise, we need to consider the value of $I_i(j\omega)$ as an additional unknown in Eq. (5.59) to make it a two parameter minimization problem [37].

5.3.3 Numerical Simulations

To validate the inversion method based on the interface removing technique, we present a numerical example with reference to Figure 5.3. In this simulation, we choose the radius of the cylinder to be $b = 30mm$. The position of the point source is $(r_0, \theta_0) = (10mm, 0^o)$ and conductivity of the cylinder is $\sigma_0 = 3.57 \times 10^7$S/m. The radius of the circle where $E(r', \theta'; j\omega)$ is measured is $r' = 32mm$ and the radius of the circle where $V(r, \theta; j\omega)$ is calculated is $r = 35mm$. The excitation frequency is 75Hz which provides a reasonable skin depth of $9.8mm$ for possible detection of the electric field and also satisfies the high frequency requirements of Eq. (5.58). Also, the excitation strength is set to be $I_i(j\omega) = 1$ for simplicity.

The simulation of the two-dimensional electric field $E(r, \theta; j\omega)$ has been conducted using the commercial finite element package FEMLAB®. A circular solution domain of radius $1000mm$ is combined with a Dirichlet boundary condition on its outer border to simulate an unbounded space. To achieve best accuracy, we employ a high mesh density around the boundary of the conductive cylinder and the source by adding artificial boundaries (the automatic mesh generator produces a mesh that is dense around all boundaries). The final mesh (see Figure 5.4) employs 24497 nodes and 48800 triangular elements of the Lagrange Quadratic type. The mesh size is as high as we can possibly handle on our Pentium®IV PC equipped with 1GB physical memory.

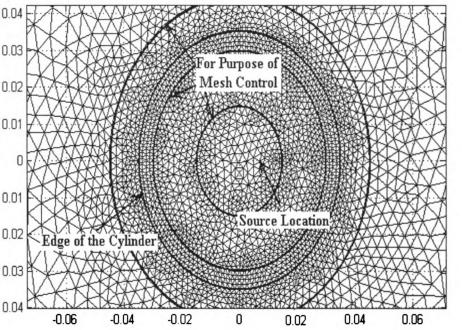

Figure 5.4: Finite element mesh in a neighborhood of the cylinder. Additional artificial boundaries have been enforced to adjust the mesh density

To utilize the Fast Fourier Transform, we sample the circle $r = r'$ uniformly at 64 points to get $E(r', \theta'_k = 2\pi k/64; j\omega)$. The numerically calculated $V(r, \theta; j\omega)$ is compared with the analytical value given by Eq. (5.57) and its high frequency approximation (5.58) is shown in Figure 5.5. The results agree very well.

If only one observation point ($N_T = 1$) is used to determine the source location, the estimation error in the distance between the point source and the observation point (r, θ_4) is 0.16 percent in the noise free case and 1.36 percent for the 10 percent additive noise case [37].

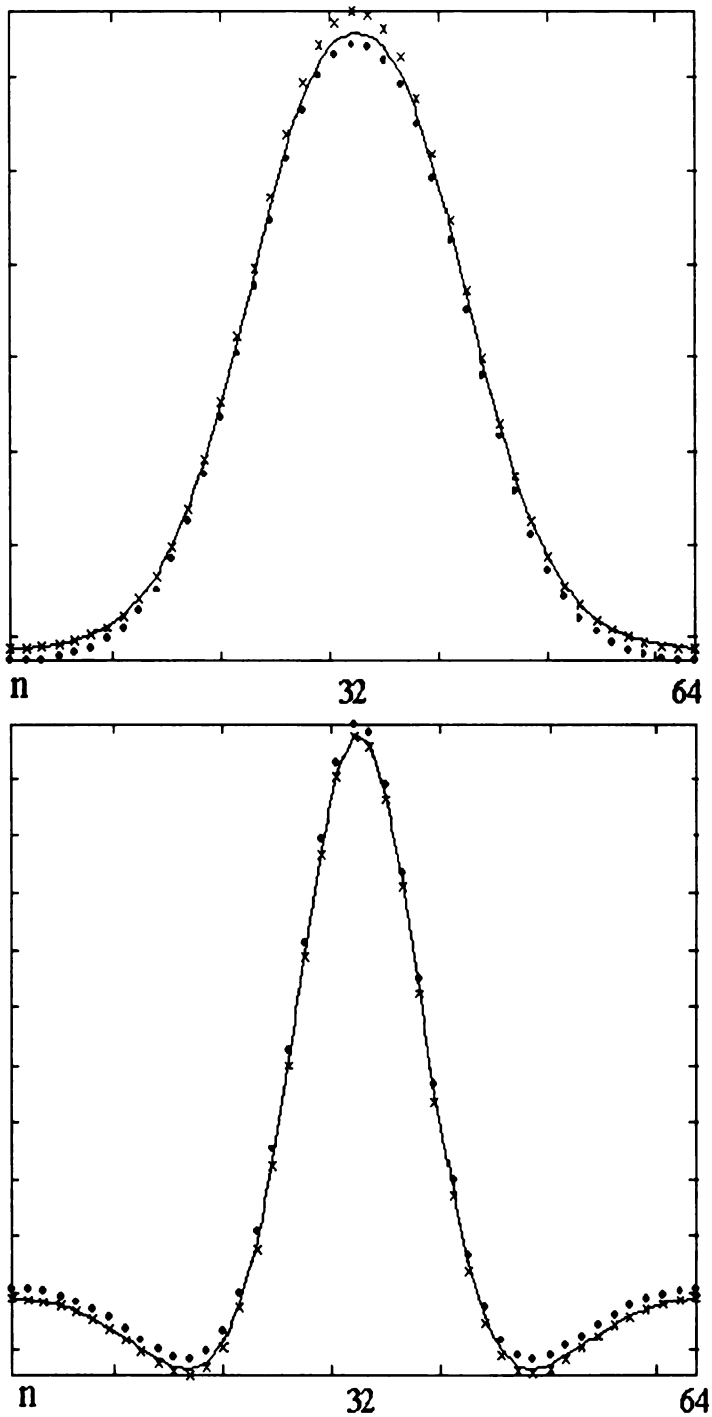

Figure 5.5: $V(r, \theta_n; j\omega)$, Upper: real part; Lower: imaginary part. (Solid line: analytical solution given by Eq. (5.57); '×': High frequency approximation given by Eq. (5.58); '•': Numerical solution constructed with Eq. (5.56).

CHAPTER 6

EXPERIMENTAL VERIFICATIONS

The interface removal algorithm discussed in Chapter 5 can be easily adapted to a planar configuration. In such a configuration, line-type current sources are placed under an infinite conducting plate. The interfaces between the plate and the background medium can be removed with a linear filtering process. Then, a localization algorithm is developed to recover the position of the sources. The advantage of the planar configuration lies in the fact that it is easier to be implemented in a laboratory.

6.1 Interface Removal for a Planar Configuration

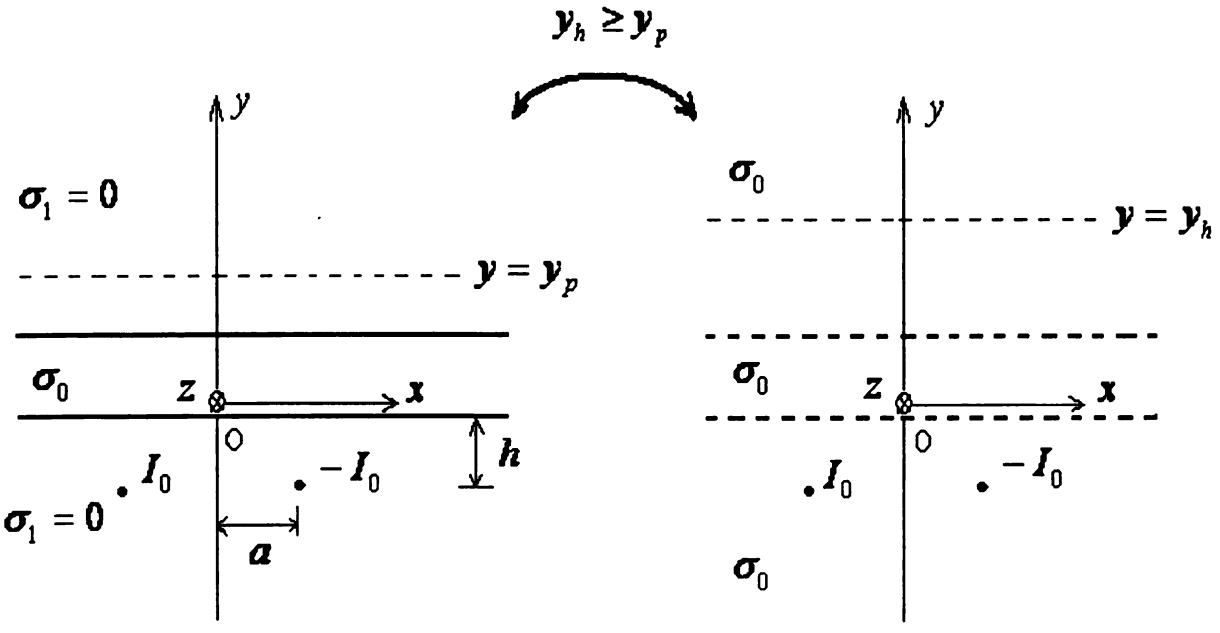

Figure 6.1: Geometry of the planar configuration for interface removal. Left: in presence of the plate; Right: inside an unbounded homogeneous medium

Figure 6.1 shows cross-section of the plane configuration, where an infinite con-

ducting plate is placed on the XZ plane. Sinusoidal current sources are located on the line $y = -h$ and extended along the z direction to infinity. The thickness of the plate is d. The conductivity of the plate and the background medium is $\sigma_0 = 2.59 \times 10^7$ (S/m) (Aluminum alloy 3003, temper H14) and $\sigma_1 = 0$ (air), respectively.

In this configuration, the magnetic field has no z dependency, allowing us to represent $\mathbf{B} = B_x(x,y)\,\hat{\mathbf{i}}_x + B_y(x,y)\,\hat{\mathbf{i}}_y$. In addition, the derivative of the field with respect to the z direction will be zero. Let $\overline{B}(k_x,y) = F_x\{B(x,y)\}$, where F_x denotes the spatial Fourier transform with respect to x, k_x is a spatial Fourier domain wavenumber and an overbar indicates the variable is in the spatial Fourier domain. Then, $\overline{B}_{yp}$ indicates the y component of magnetic flux density field excited in presence of the plate while $\overline{B}_{yh}$ indicates the field resulting from the same source excitations but with homogeneous background media of σ_0. The linear relation between $\overline{B}_{yh}$ and $\overline{B}_{yp}$ is given by [62]:

$$\frac{\overline{B}_{yp}(k_x,y_p)}{\overline{B}_{yh}(k_x,y_h)} = \frac{4\exp\left[j\lambda_0(y_h+h)\right]\exp\left[-|k_x|(y_p-h-d)\right]}{(1-j|k_x|/\lambda_0)^2 exp(j\lambda_0 d) + (1+j|k_x|/\lambda_0)^2 exp(-j\lambda_0 d)}, \tag{6.1}$$

where $\lambda_0^2 \equiv -j\omega\mu_0\sigma_0 - k_x^2$, y_h and y_p is the position of the line of measurement for the homogeneous media problem and for the planar problem, respectively. The interface removal filter (6.1) is independent of the form of source excitations, which allows us to use arbitrary source excitations located on the $y = -h$ plane. The stability condition of the filter is $y_h \geq y_p$ [62].

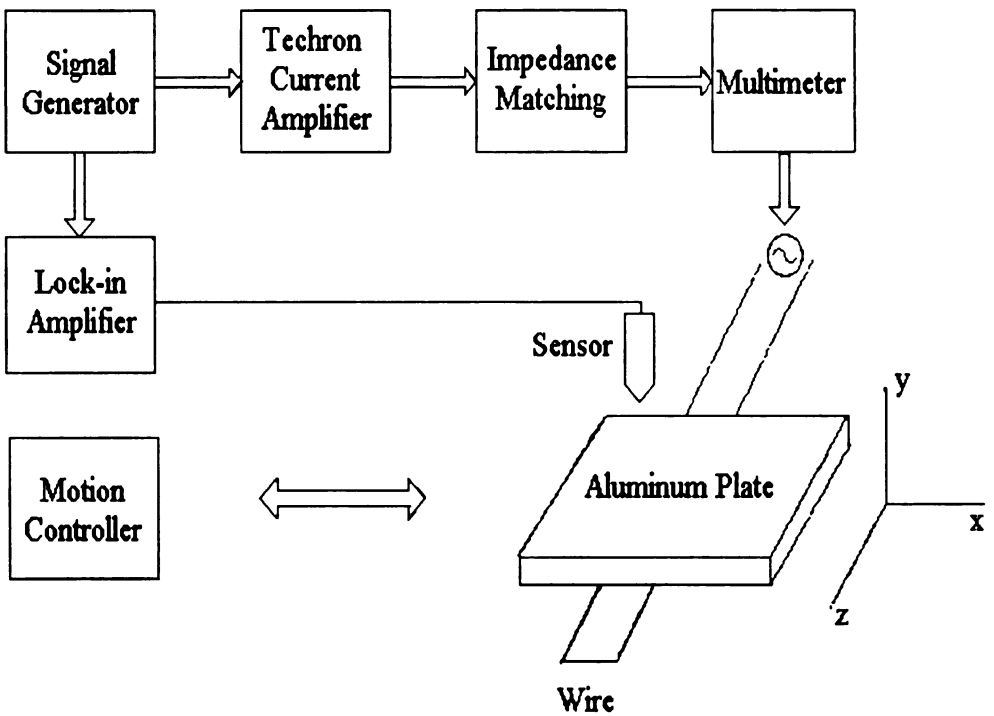

Figure 6.2: Experimental Set-up

6.2 Experimental Set-up

The current source used in this experiment is a two-wire system. These two wires are parallel to each other and carry alternating current in opposite directions. A 304.8mm × 304.8 mm (12 inch by 12 inch) aluminum plate of thickness 2.54 mm (0.1 inch) is placed 4.96 mm above the plane of the two-wire system. The length of the parallel segment of the wires is 635 mm (25 inch). The wires are twisted together rest of the length and connected in series with a impedance matching circuit (0.5Ω plus 0.5 mH) to a Techron 8604 current amplifier (GE). A motion controller is used to move a magnetic field sensor (oriented to detect the y component of the magnetic field) along a line of measurement above the plate and perpendicular to the wires.

The outputs of the magnetic field sensor is measured using a lock-in amplifier.

This configuration can be described with a two dimensional model. In such a model, the parallel wires acts as two point sources. A two-wire system was adopted instead of a simpler system consisting only one infinite wire along the z direction for practical reasons. A two-wire system is less sensitive to the environmental noises. Also, it generates a stronger magnetic field, which is important for maintaining a high signal to noise ratio.

The magnetic fields generated above the plate is in the range of zero to 0.15 Gauss (magnitude) when the excitating frequency lies between 100 and 6000 Hz. Two magnetic field sensors are used: an inductive coil and a GMR (Giant magnetoresistive) magnetic field sensor (NVE corporation, AAH-002-02 model).

The inductive coil used in this experiment includes 106 turns of wires. The diameter and thickness of the coil is 3 mm and 1 mm, respectively. The relation between its output voltage and the applied magnetic field can be expressed as:

$$H_{coil} = k_c \frac{V_{coil}}{f} \times 10^4, \tag{6.2}$$

where V_{coil} is the output voltage in Volts and H_{coil} is the applied magnetic field in Gauss (both in rms values), f is the excitation frequency in Hz and $k_c = 554.48$ is a calibration constant determined experimentally using a well-calibrated inductive coil. The GMR sensor is sealed inside a standard SOIC8 package of size 3.91 by 4.9 mm. The dimensions of its active area is about $100\mu m$ by $200\mu m$ and is located in the middle of the package. The sensor generates a 10 mV output at 0.25 Gauss with a 4.96 V DC supply. It offers 96% linearity from 10% to 70% of full scale with excel-

lent directivity characteristic. The GMR sensor is also characterized with omnipolar outputs, which means it provides positive outputs for both directional positive and negative applied fields. In order to obtain bipolar output, the GMR sensor was biased with a small permenant magnet during the experiment. Unfortunately, the offset DC fields generated inside the sensor could not be controlled very well due to memory properties of the sensor. The field is determined using

$$H_{GMR} = k_n V_{GMR}, \tag{6.3}$$

where V_{GMR} is the output voltage in mV and H_{GMR} is the applied magnetic field in Gauss and $k_n = 1/42.73$ is the calibration constant.

Due to their small dimensions, both the GMR sensor and the inductive coil can be approximated as point sensors. The inductive coil is quite simple to use and is characterized by high linearity. However, it is costly and less sensitive for low frequency fields. The GMR sensor is inexpensive and provides high sensitivity without significant frequency dependency. Both sensors were employed and the repeatability of their performance has been tested.

Several aspects of this experimental set-up have been investigated to reduce possible error sources. (1) The transverse dimension of the conducting plate is sufficiently large so that the effect of the finite dimensions of the plate is negligible; (2) The output signals of both magnetic field sensor were measured with a lock-in amplifier in the differential mode to exploit its high common mode noise rejection capability (up to 100 dB); (3) The environmental noise was reduced; (4) The current fluctuations were reduced to a minimum by using constant current mode of the Techron current

amplifier. The magnitude of the current was recorded and used to account for the effect of current fluctuations; (5) Efforts were made to reduce positioning errors.

6.3 Experiment Results

We used 100 Hz and 6 kHz as the excitation frequency in case of the GMR sensor and the inductive coil, respectively. The lift-off is 3.81 mm (0.15 inch) for the GMR sensor and 1.8 mm for the inductive coil. The magnitude/phase pair or real/imaginary components of the field B_y was recorded at each measuring point. To set a reference for recorded phase information, the field at center between two wires ($x = 0$) was measured experimentally and the phase at this point is set to π.

In an effort to check accuracy of the experimental data, a two-dimensional numerical model was developed using a commercial finite element analysis package FEMLAB®. The agreement between experimental data and results of numerical simulations is very good.

In case of the GMR sensor, three data sets were obtained. The first data set, 'GMR I', recorded measurements in the form of magnitude/phase pairs while other two sets, i.e. 'GMR II' and 'GMR III', recorded measurements in the form of real/imaginary component pairs. Data sets 'GMR I' and 'GMR II' were obtained using the same magnetic bias level while 'GMR III' use a different bias level. The numerical simulation results and experimental data are shown in Figure 6.3 through 6.7. The 'GMR III' data shows better match with the numerical results suggesting that the bias level is better suited.

In case of the inductive coil measurements, two data sets were obtained, called

'Coil I' and 'Coil II', respectively. Both data sets were recorded in form of magnitude/phase pairs and shown in Figure 6.8 through 6.12. We notice that mismatch in phase which arises when the magnitude of the fields are lower than 0.002 Gauss (which corresponds to 20 μV output of the inductive coil).

The experimental results obtained can be used as inputs to the linear filtering process expressed by equation (6.1). By selecting $y_h \geq y_p$, the fields of homogeneous media $B_{yh}(x, y_h)$ are obtained and compared with analytical solutions (Figures 6.13 through 6.18). Based on knowledge of the excitation fields in homogeneous media, it is much easier to solve for the locations of the current sources. Figure 6.19 through 6.22 show the error functions in the localization of the current source for recovering the source location $(\pm a, -h)$. Assume h is known, the relative positioning error is 3.28% using the GMR sensor data and 0.13% using the inductive coil data, respectively. The expected value of a is 0.01582 m.

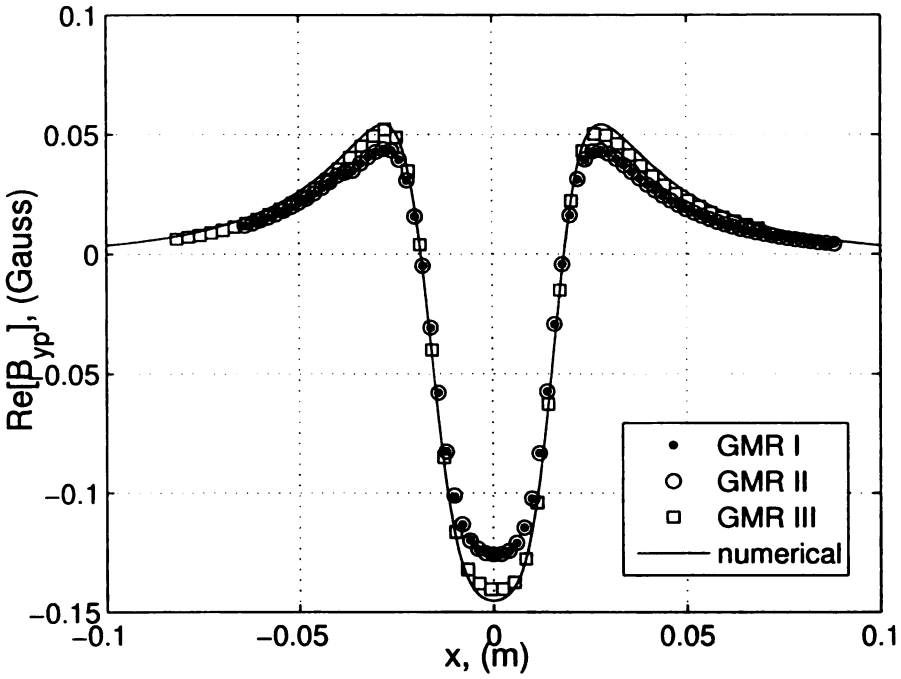

Figure 6.3: Real part of B_{yp} (GMR sensor)

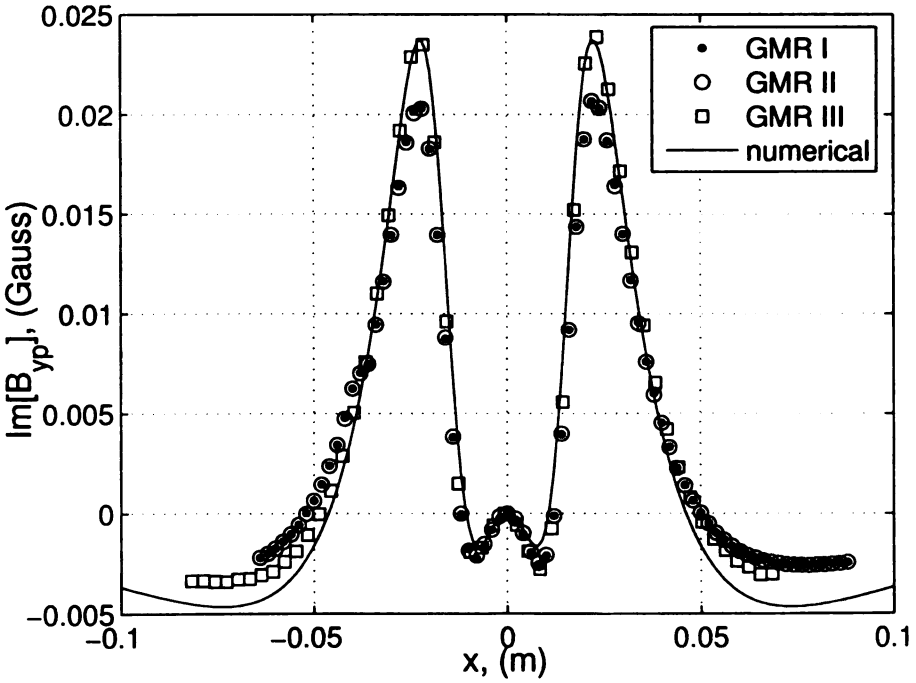

Figure 6.4: Imaginary part of B_{yp} (GMR sensor)

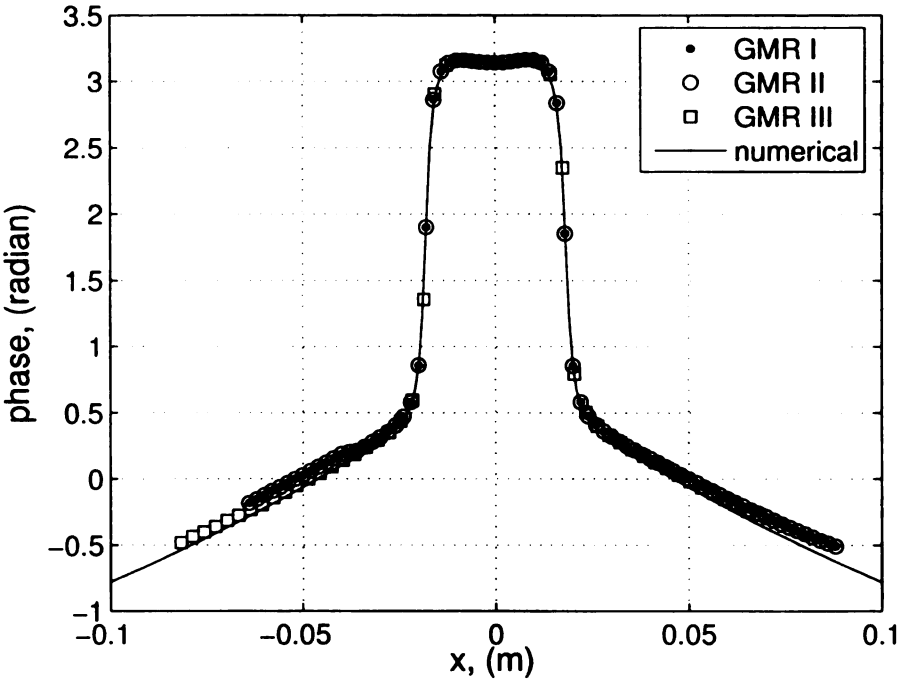

Figure 6.5: Phase of B_{yp} (GMR sensor)

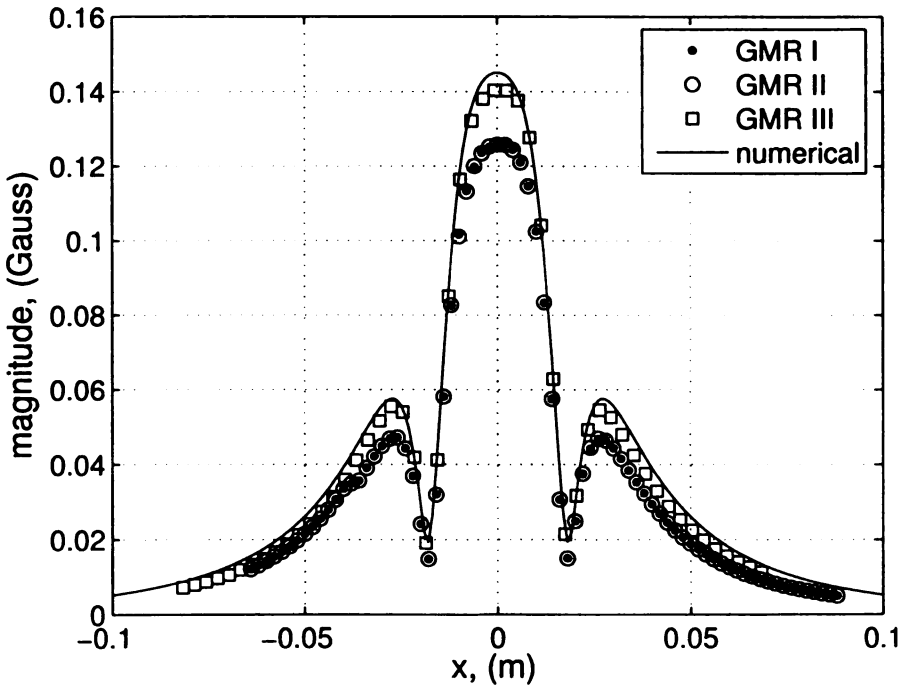

Figure 6.6: Magnitude of B_{yp} (GMR sensor)

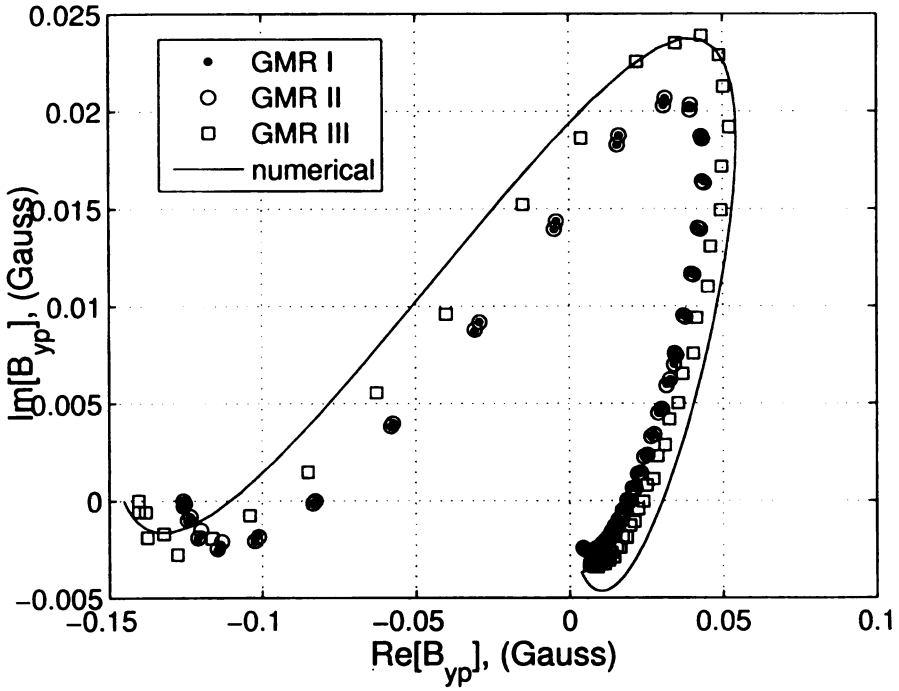

Figure 6.7: Complex plane plot of B_{yp} (GMR sensor)

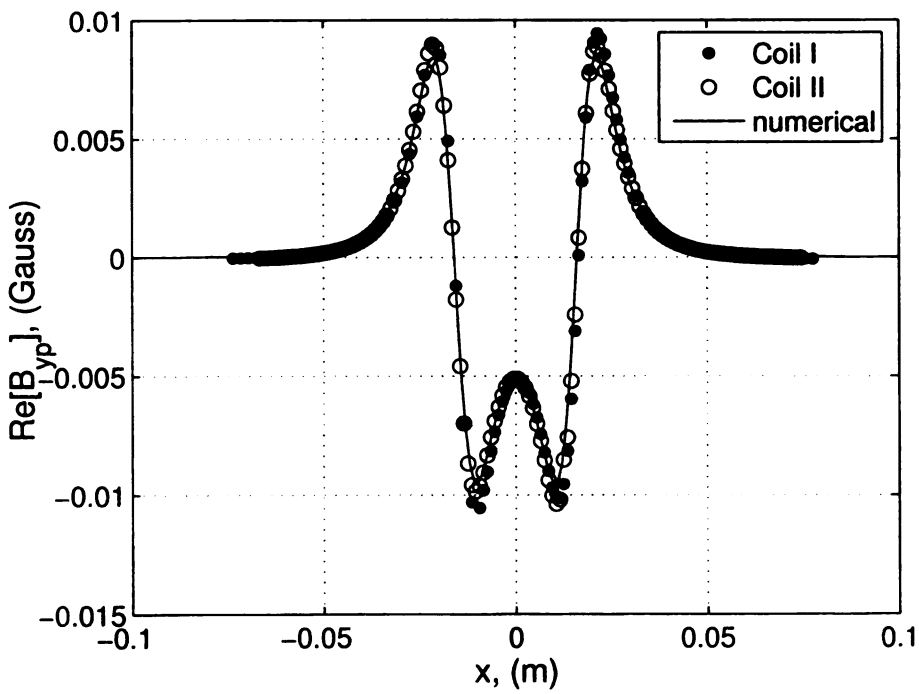

Figure 6.8: Real part of B_{yp} (Inductive coil)

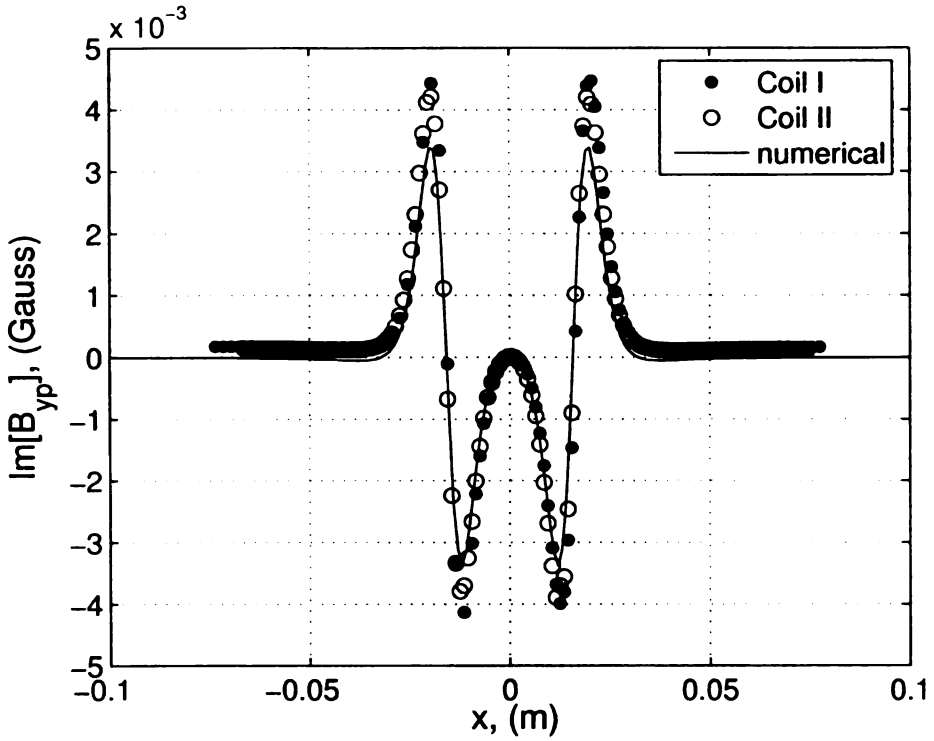

Figure 6.9: Imaginary part of B_{yp} (Inductive coil)

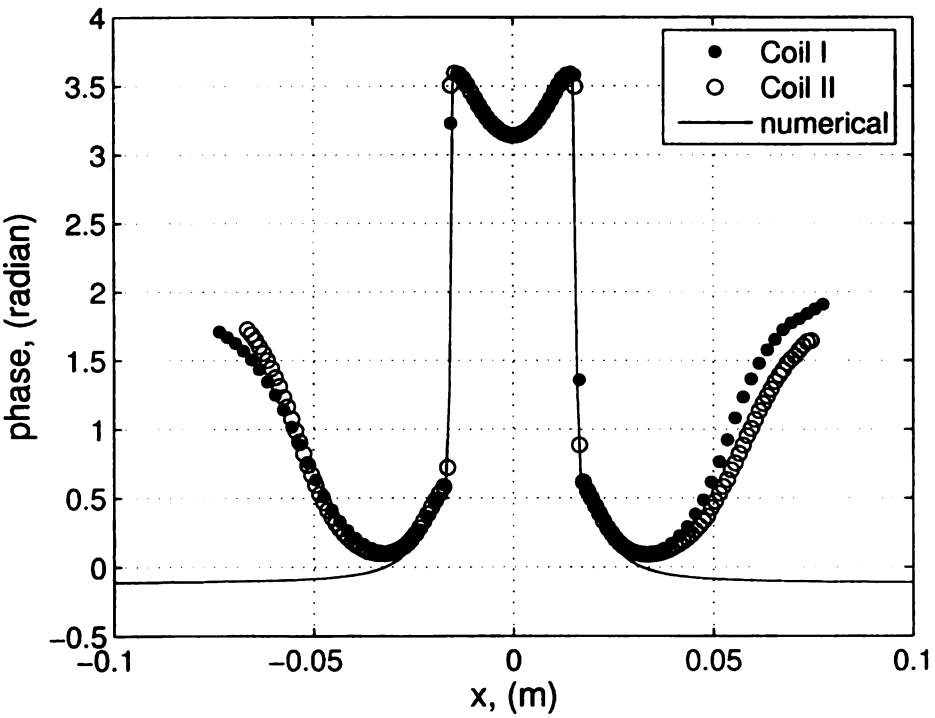

Figure 6.10: Phase of B_{yp} (Inductive coil)

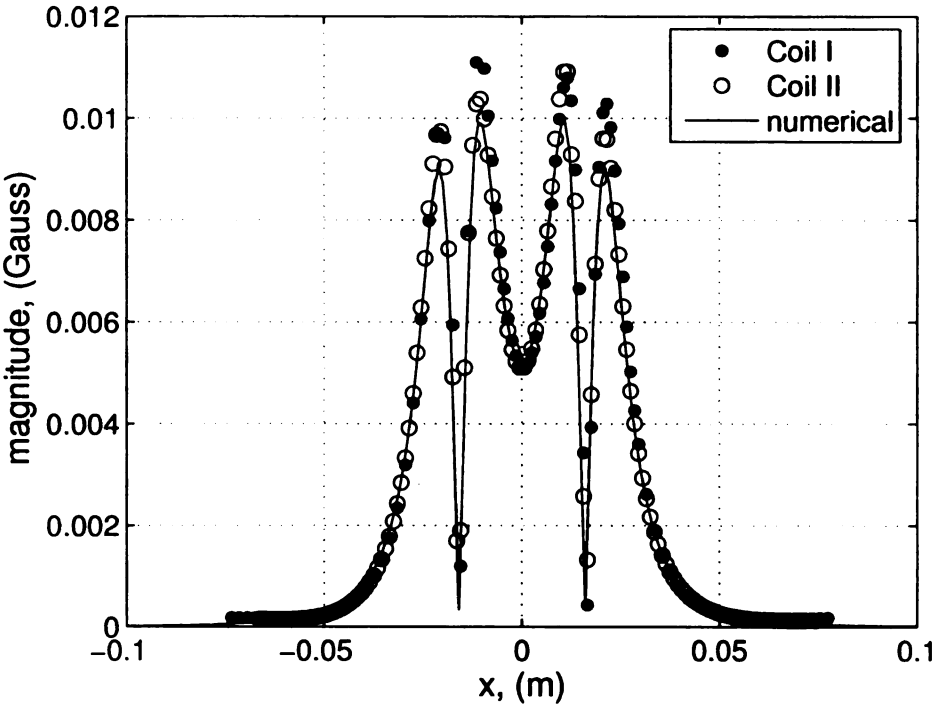

Figure 6.11: Magnitude of B_{yp} (Inductive coil)

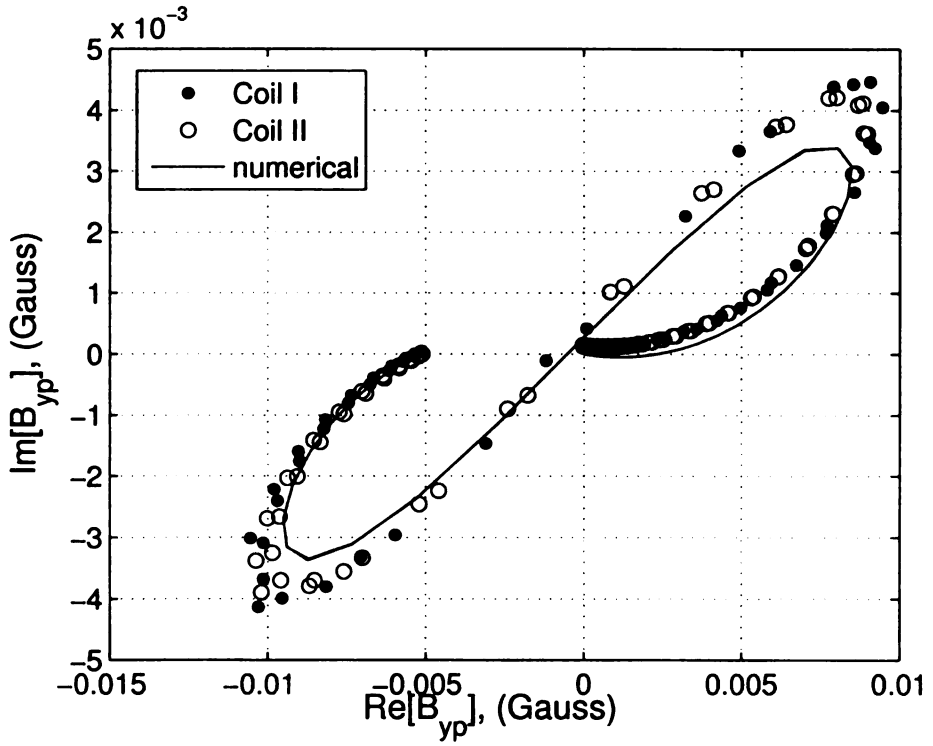

Figure 6.12: Complex plane plot of B_{yp} (Inductive coil)

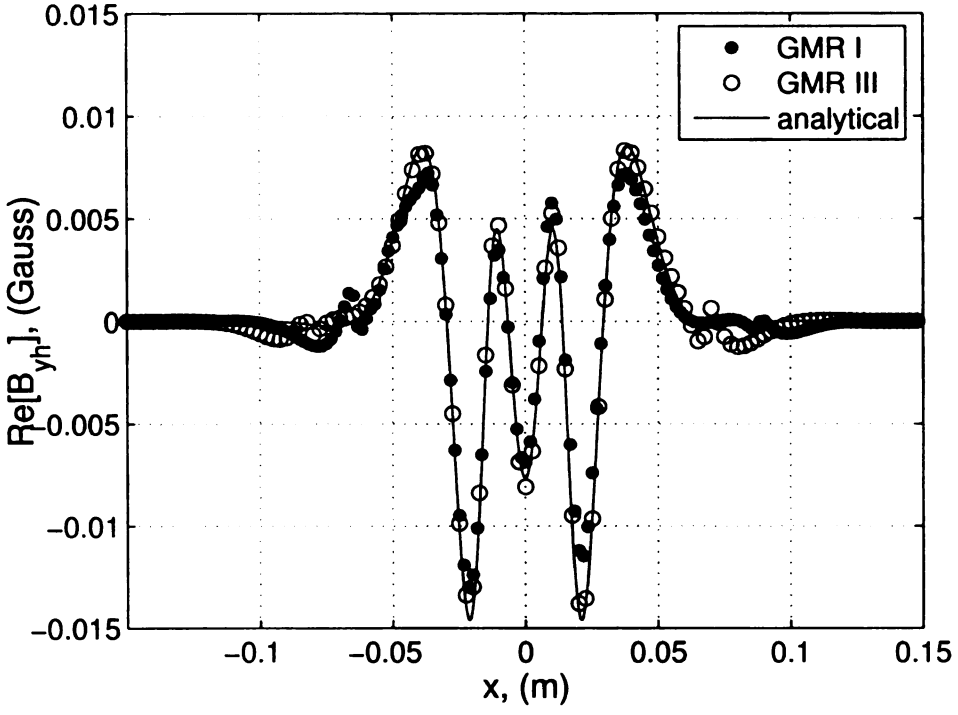

Figure 6.13: Real part of $B_{yh}(x, y_h)$ (filtered from GMR data)

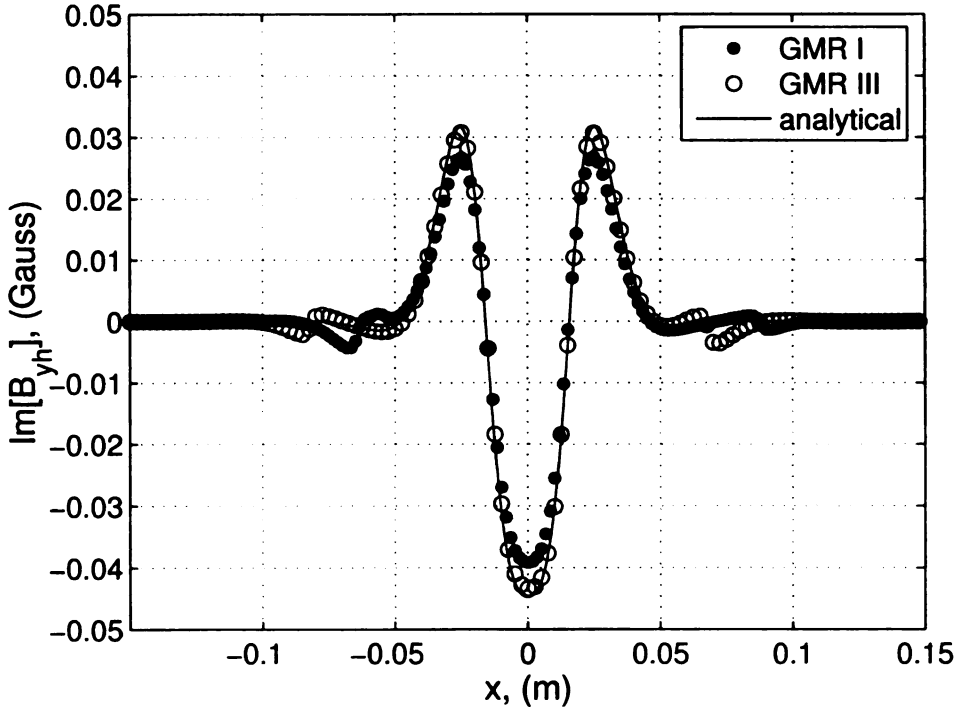

Figure 6.14: Imaginary part of $B_{yh}(x, y_h)$ (filtered from GMR data)

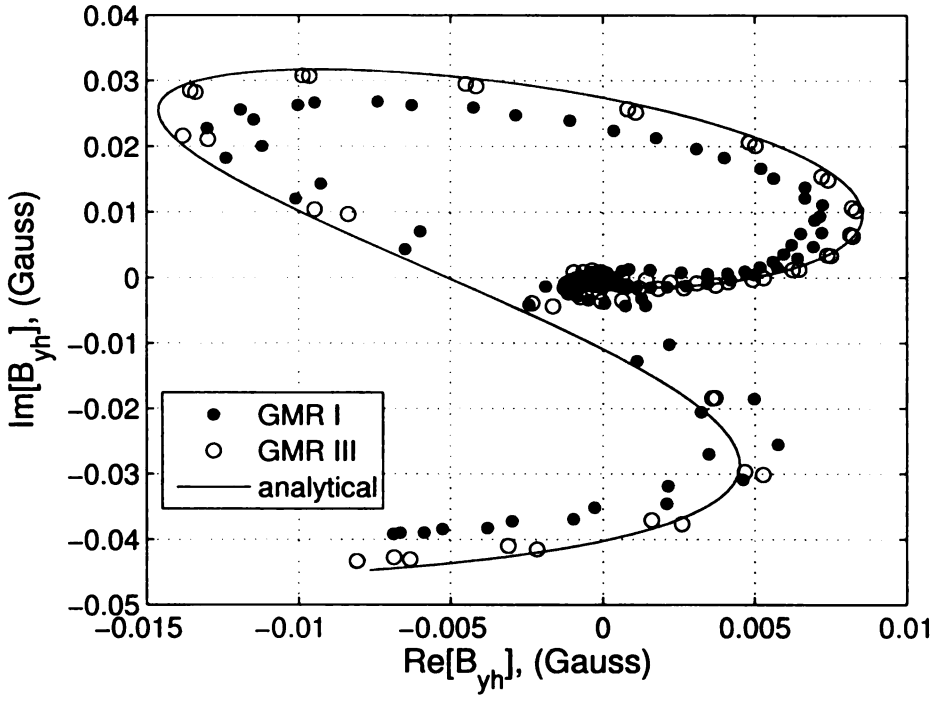

Figure 6.15: Complex plane plot of $B_{yh}(x, y_h)$ (filtered from GMR data)

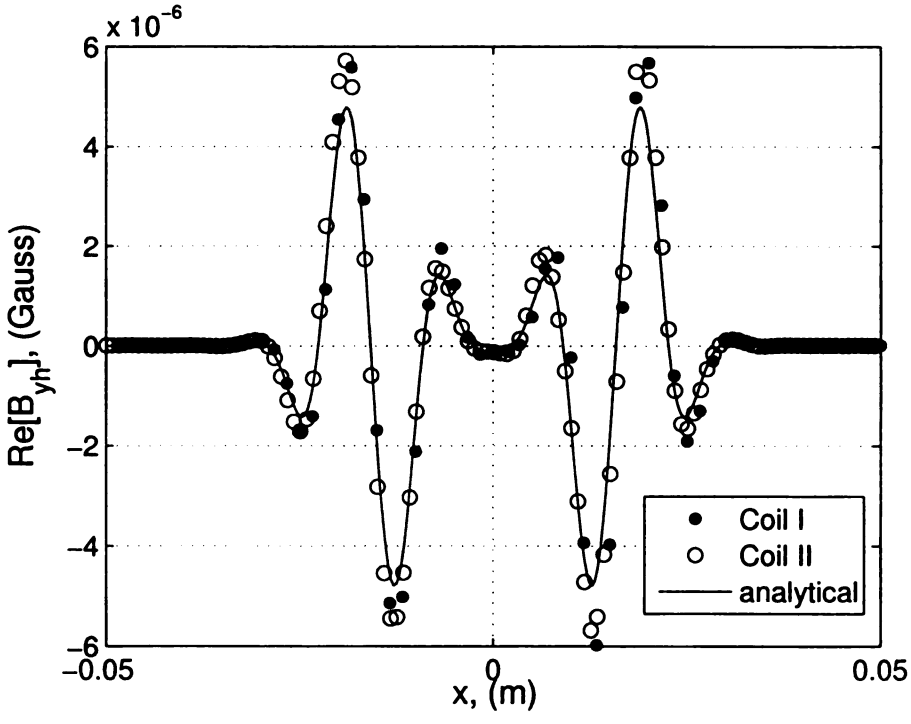

Figure 6.16: Real part of $B_{yh}(x, y_h)$(filtered from inductive coil data)

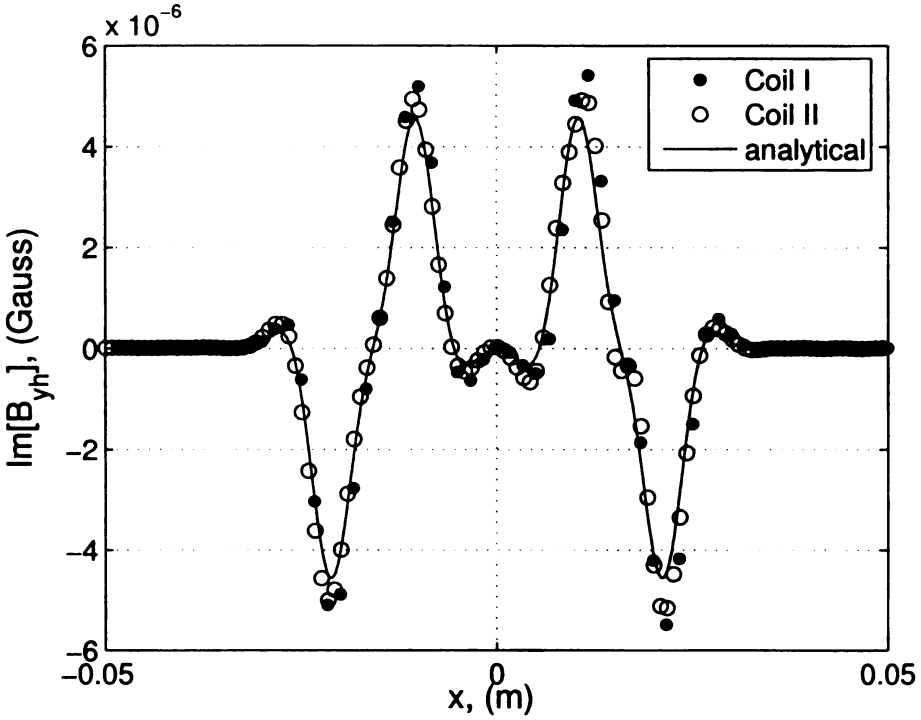

Figure 6.17: Imaginary part of $B_{yh}(x, y_h)$ (filtered from inductive coil data)

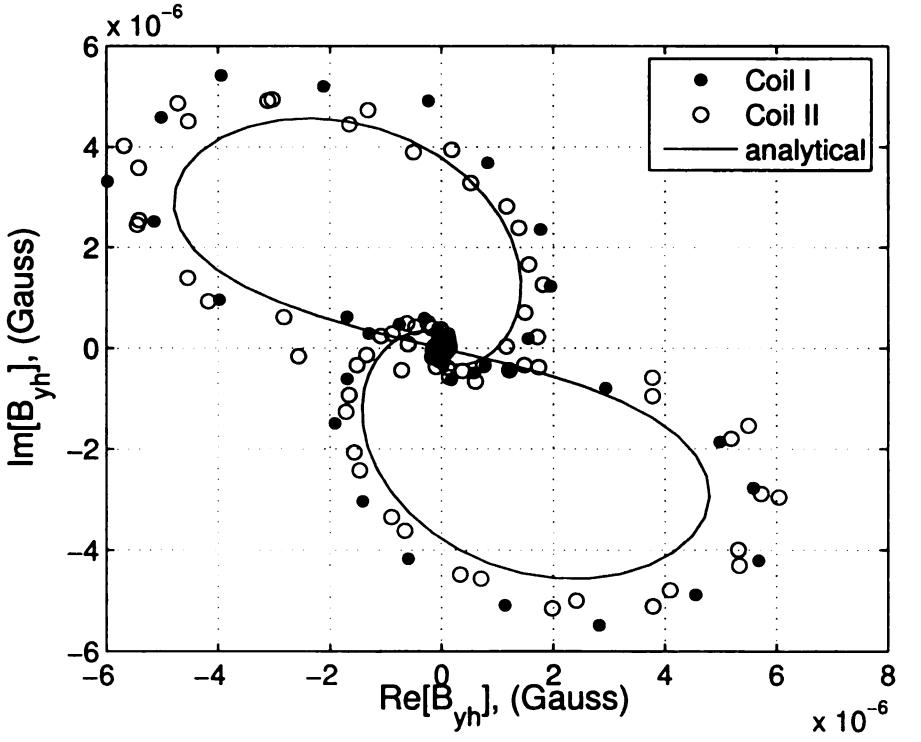

Figure 6.18: Complex plane plot of $B_{yh}(x, y_h)$ (filtered from inductive coil data)

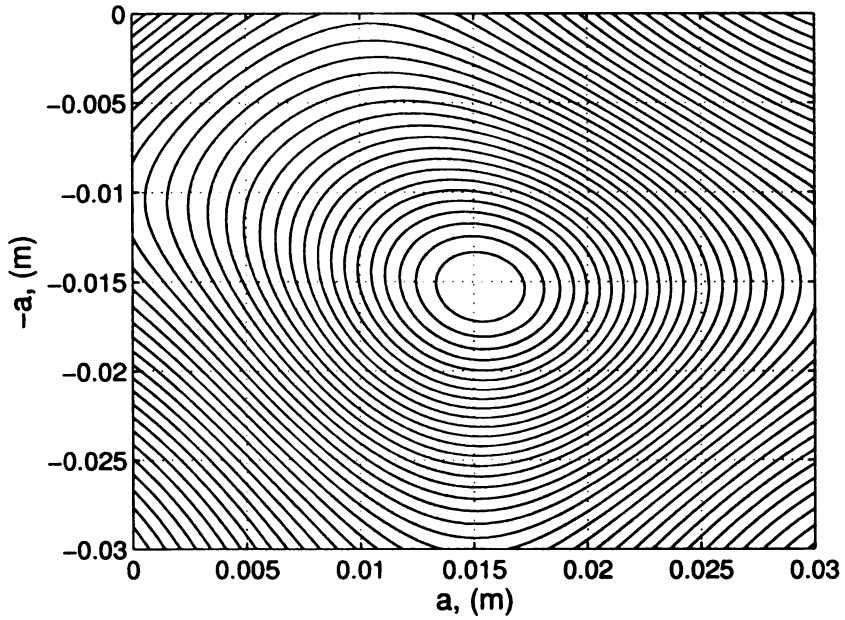

Figure 6.19: Error function used for recovering the source location $(-a, a)$, unit: m, (contour plot, 'GMR I')

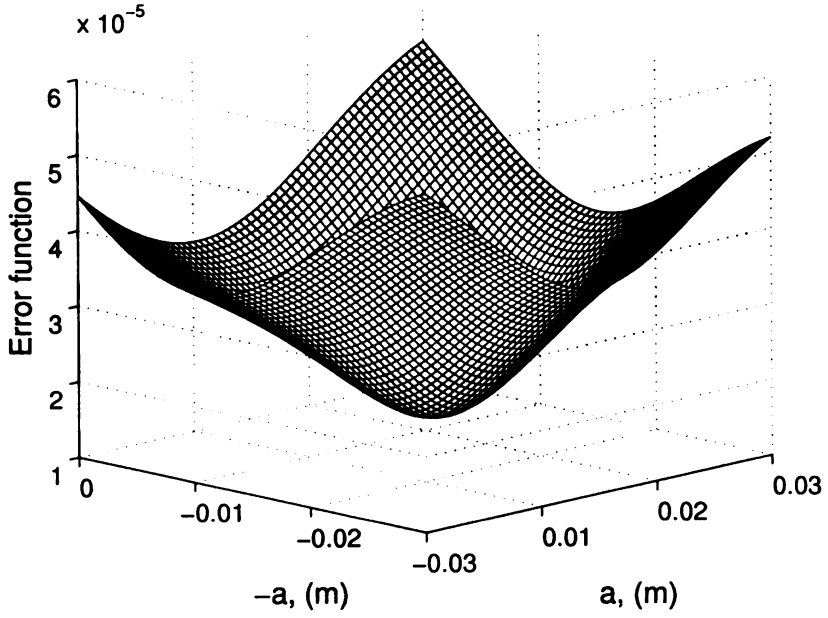

Figure 6.20: Error function used for recovering the source location $(-a, a)$, unit: m, (mesh plot, 'GMR I')

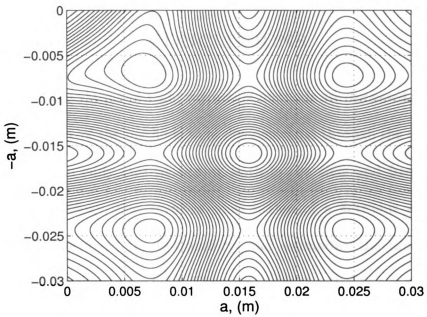

Figure 6.21: Error function used for recovering the source location $(-a, a)$, unit: m, (contour plot, 'Coil I')

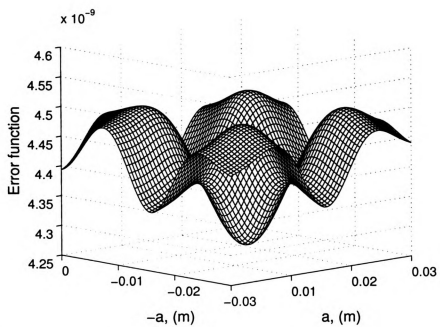

Figure 6.22: Error function used for recovering the source location $(-a, a)$, unit: m, (mesh plot, 'Coil I')

CHAPTER 7

CONCLUSIONS

Q-transform based time-of-flight extraction methods are discussed in this dissertation. The feasibility of the methods were demonstrated through the use of canonical inverse problems in eddy current testing both in the time and frequency domain. The basic methodology used involves construction of a fictitious wave field from ECT measurements using the Q-transform and estimating the time-of-flight from the constructed fictitious wave field. The time-of-flight estimate can then be used for source/defect localization and potentially be fused with time-of-flight measurements obtained from the wave field directly. Numerical simulations based on the finite element method were implemented for validating the concept. Experimental results validating the concepts were also obtained.

- In the time domain, time-of-flight associated with (fictitious) wave front can be determined using carefully designed excitation signals. The approach was illustrated by studying the scattering from a small anomaly embedded in an infinite homogeneous medium. The position of the anomaly was estimated using measurements of diffusion domain responses with both scalar and vector formulations.

- In the harmonic domain, the existence of the time-of-flight information in non-local measurements of the Fourier coefficients was proved. A linear filtering method was developed to remove the material discontinuities for an long conductive cylinder embedded in an unbounded homogeneous space and the po-

sition of a long cylindrical hole inside the conductor was estimated through measured time-of-flight information.

- In the experimental work, two current carrying wires are placed under a conducting plate. Measurements of the magnetic flux density field (component perpendicular to the plate) was obtained using a GMR sensor as well as an inductive coil. These experimental measurements agree with theoretical predictions very well. The effectiveness of the interface removal algorithm is then demonstrated using experimental measurements. The experimental data was also employed to recover the location of the source currents.

This work summarizes the progresses made using Q-transform based methods in recent years. The approach presennted herein, we believe, is the first phenomenological approach to extracting time-of-flight information from diffusion based NDE techniques.

This research has presented a useful paradigm for exploring the time-of-flight extraction approach for potential NDE applications. Several canonical problems have been systematically studied, and more importantly, basic methodologies and strategies for solving these problems have been established and summarized. Capitalizing on this attractive paradigm, it will be beneficial to explore new applications of practical interest. This study prompts future work to identify and study other NDE problems. Possible future work may include:

- Identifying TOF information from 3D complex structures based on real industrial applications;

- Localizing the positions of sources/defects, or mapping material parameters,

through advanced imaging technique developed for wave propagation applications;

- Fusing retrieved TOF information with measurements obtained from wave propagation based NDE techniques.

APPENDIX A

Q-TRANSFORM PAIRS AND THE $\widetilde{Q}$-TRANSFORM

A.1 Q-transform Pairs

Here we give a concise list of some useful Q-transforms pairs. Detailed derivations of Eqs. (A.1)-(A.7) were presented in [6, 7, 16, 32].

$$\mathcal{Q}\left\{\delta\left(q\right)\right\}\left(t\right) = \delta\left(t\right) \tag{A.1}$$

$$\mathcal{Q}\left\{\sin\left(\omega q\right)\right\}\left(t\right) = \omega \exp\left(-\omega^2 t\right) \tag{A.2}$$

$$\mathcal{Q}\left\{\cos\left(\omega q\right)\right\}\left(t\right) = \frac{1}{\pi t}\left[1 - 2\omega^2 t \Phi\left(1; \frac{3}{2}; -\omega^2 t\right)\right] \tag{A.3}$$

$$\mathcal{Q}\left\{\frac{q^{2n+1}}{(2n+1)!}\right\}\left(t\right) = \frac{t^n}{n!} \tag{A.4}$$

$$\mathcal{Q}\left\{\frac{1}{2\omega^2}\left[\sin\left(\omega q\right)\cosh\left(\omega q\right) - \cos\left(\omega q\right)\sinh\left(\omega q\right)\right]\right\}\left(t\right) = \sin\left(2\omega^2 t\right) \tag{A.5}$$

$$\mathcal{Q}\left\{\frac{1}{2\omega^2}\left[\cos\left(\omega q\right)\sinh\left(\omega q\right) + \sin\left(\omega q\right)\cosh\left(\omega q\right)\right]\right\}\left(t\right) = \cos\left(2\omega^2 t\right) \tag{A.6}$$

$$\mathcal{Q}\left\{H\left(q - q_0\right)\right\}\left(t\right) = \frac{1}{\sqrt{\pi t}} \exp\left(-\frac{q_0^2}{4t}\right) \tag{A.7}$$

$$\mathcal{Q}\left\{qH\left(q - q_0\right)\right\}\left(t\right) = \frac{q_0}{\sqrt{\pi t}} \exp\left(-\frac{q_0^2}{4t}\right) + \operatorname{erfc}\left(\frac{q_0}{2\sqrt{t}}\right) \tag{A.8}$$

$$\mathcal{Q}\left\{\left(q - q_0\right) H\left(q - q_0\right)\right\}\left(t\right) = \operatorname{erfc}\left(\frac{q_0}{2\sqrt{t}}\right) \tag{A.9}$$

$$\mathcal{Q}\left\{q^2 H\left(q - q_0\right)\right\}\left(t\right) = \frac{q_0^2 + 4t}{\sqrt{\pi t}} \exp\left(-\frac{q_0^2}{4t}\right) \tag{A.10}$$

$$\mathcal{Q}\left\{(q-q_0)^2 H(q-q_0)\right\}(t) = -2q_0\mathrm{erfc}\left(\frac{q_0}{2\sqrt{t}}\right) + 4\sqrt{\frac{t}{\pi}}\exp\left(-\frac{q_0^2}{4t}\right) \tag{A.11}$$

$$\mathcal{Q}\left\{q^3 H(q-q_0)\right\}(t) = 6t\mathrm{erfc}\left(\frac{q_0}{2\sqrt{t}}\right) + \frac{q_0^3+6q_0t}{\sqrt{\pi t}}\exp\left(-\frac{q_0^2}{4t}\right) \tag{A.12}$$

$$\mathcal{Q}\left\{(q-q_0)^3 H(q-q_0)\right\}(t) = \left(6t+3q_0^2\right)\mathrm{erfc}\left(\frac{q_0}{2\sqrt{t}}\right) - 6q_0\sqrt{\frac{t}{\pi}}\exp\left(-\frac{q_0^2}{4t}\right) \tag{A.13}$$

Note that q_0 is a nonnegative constant in Eqs. (A.7) through Eq. (A.13) and $\mathrm{erfc}(\cdot)$ is the complementary error function [54].

A.2 The $\widetilde{Q}$-transform

$\widetilde{Q}$-transform is also an invertible mapping between solutions of parabolic equations and those of hyperbolic equations, which is slightly different with Q-transform [14, 10]. Consider partial differential equations (PDEs) of the parabolic type

$$\partial_t v(\mathbf{x},t) = \mathcal{L}v(\mathbf{x},t) + f(\mathbf{x},t) \tag{A.14}$$

$$v(\mathbf{x},0) = \phi(\mathbf{x}) \tag{A.15}$$

$$\partial_n v(\mathbf{x},t) = \psi(\mathbf{x},t) \text{ on } S \tag{A.16}$$

and of the hyperbolic type

$$\partial_{qq} u(\mathbf{x},q) = \mathcal{L}u(\mathbf{x},q) + g(\mathbf{x},q) \tag{A.17}$$

$$u(\mathbf{x},0) = \phi(\mathbf{x}) \tag{A.18}$$

$$\partial_q u(\mathbf{x},0) = 0 \tag{A.19}$$

$$\partial_n u(\mathbf{x},q) = \varphi(\mathbf{x},q) \text{ on } S, \tag{A.20}$$

respectively. Here $\mathcal{L}$ is a uniformly elliptical operator with continuous coefficients depending only on the variable $\mathbf{x}$, n is a conformal to S. $g(\mathbf{x}, q)$ and $\varphi(\mathbf{x}, q)$ are smooth functions of their arguments and grow not faster that $Ce^{\alpha q}$ at $q \to \infty$. Assume that conditions

$$f(\mathbf{x}, t) = \frac{1}{\sqrt{\pi t}} \int_0^\infty g(\mathbf{x}, q) \exp\left(-\frac{q^2}{4t}\right) dq \tag{A.21}$$

and

$$\psi(\mathbf{x}, t) = \frac{1}{\sqrt{\pi t}} \int_0^\infty \varphi(\mathbf{x}, q) \exp\left(-\frac{q^2}{4t}\right) dq \tag{A.22}$$

are satisfied. The solutions of Eqs. (A.14)-(A.16) and Eqs. (A.17)-(A.20) are related with the $\widetilde{Q}$-transform, which is defined as

$$\widetilde{v}(t) = \widetilde{\mathcal{Q}}\{u(q)\}(t) \equiv \frac{1}{\sqrt{\pi t}} \int_0^\infty u(q) \exp\left(-\frac{q^2}{4t}\right) dq. \tag{A.23}$$

We notice that function

$$G(t, q) = \frac{1}{\sqrt{\pi t}} \exp\left(-\frac{q^2}{4t}\right) \tag{A.24}$$

is the solution of the equation of heat conductivity $G_t = G_{qq}$ and

$$\widetilde{v}(t) = \widetilde{\mathcal{Q}}\{u(q)\}(t) = \frac{1}{2t} \mathcal{Q}\left\{\frac{u(q)}{q}\right\}(t). \tag{A.25}$$

As an alternative to the Q-transform, $\widetilde{Q}$-transform could be useful for data fusion tasks once its mathematical properties are fully explored.

Corresponding to formulas presented in section 3.2 and A.1 for the Q-transform, important mathematical properties of the $\widetilde{Q}$-transform are derived and listed below for reference. Similarities between Q-transform and $\widetilde{Q}$-transform can be easily identified

(see Eqs. (A.2)-(A.3) and (A.32)-(A.33)).

$$\widetilde{\mathcal{Q}}\{\delta(q)\} = \frac{1}{\sqrt{\pi t}} \tag{A.26}$$

$$\widetilde{\mathcal{Q}}\{\alpha u(q)\} = \alpha \widetilde{\mathcal{Q}}\{u(q)\} \tag{A.27}$$

$$\widetilde{\mathcal{Q}}\{H(q-q_0)\} = \operatorname{erfc}\left(\frac{q_0}{2\sqrt{t}}\right) \tag{A.28}$$

$$\widetilde{\mathcal{Q}}\{u(\alpha q)\} = \widetilde{\mathcal{Q}}\{u(q)\}\left(\alpha^2 t\right) \tag{A.29}$$

$$\frac{d\widetilde{\mathcal{Q}}\{u(q)\}(t)}{dt} = \frac{1}{4t^2}\widetilde{\mathcal{Q}}\{q^2 u(q)\} - \frac{5}{2t}\widetilde{\mathcal{Q}}\{u(q)\} \tag{A.30}$$

$$\widetilde{\mathcal{Q}}\{u'(q)\} = -\frac{u(q_{0+})}{\sqrt{\pi t}} + \mathcal{Q}\{u(q)\} \tag{A.31}$$

$$\widetilde{\mathcal{Q}}\{\sin(\omega q)\} = \frac{2\omega t}{\sqrt{\pi t}}\Phi\left(1;\frac{3}{2};-\omega^2 t\right) = -\frac{1}{\omega}\mathcal{Q}\{\cos(\omega q)\} + \frac{1}{\omega\sqrt{\pi t}} \tag{A.32}$$

$$\widetilde{\mathcal{Q}}\{\cos(\omega q)\} = \exp\left(-\omega^2 t\right) \tag{A.33}$$

$$\widetilde{\mathcal{Q}}\{q^n\} = \mathcal{Q}\left\{\frac{q^{n+1}}{n+1}\right\} \tag{A.34}$$

$$\widetilde{\mathcal{Q}}\left\{q^{2n}\right\} = \frac{(2n)!}{n!}t^n \qquad n \geq 0, n \in Z \tag{A.35}$$

$$\widetilde{\mathcal{Q}}\left\{q^{2n+1}\right\} = \frac{n!}{2\sqrt{\pi t}}(4t)^{n+1} \qquad n \geq 0, n \in Z \tag{A.36}$$

BIBLIOGRAPHY

[1] Cartz, L., *Nondestructive Testing*, ASM International, 1995.

[2] Gros, X. E., *NDT Data Fusion*, Arnold, 1997.

[3] Chan, S. C., Udpa, L. and Udpa, S., "Design of an NDE Integrated Data Acquisition System (NIDAS)", in *Review of Progress in Quantitative Nondestructive Evaluation*, Edited by Thompson, D. O. and Chimenti, D. E., New York: Plenum Press, **vol. 22**, pp.585-592, 2002.

[4] Udpa, L. and Lord, W., "Diffusion, Waves, Phase and Eddy Current Imaging", in *Review of Progress in Quantitative Nondestructive Evaluation*, Edited by Thompson, D. O. and Chimenti, D. E., New York: Plenum Press, **vol. 4**, pp.499-506, 1985.

[5] Lee, K. H. and Xie, G., "A New Approach to Imaging with Low Frequency Electromagnetic Fields", *Geophysics*, **vol. 58**, pp.786-796, 1993.

[6] Lee, K. H., Liu, G. and Morrison, H. F., "A New Approach to Modeling the Electromagnetic Response of Conductive Media", *Geophysics*, **vol. 54**, pp.1180-1192, 1989.

[7] Ross, S., Lusk, M., and Lord, W., "Application of a Diffusion-to-Wave Transformation for Inverting Eddy Current Nondestructive Evaluation Data", *IEEE Trans. on Magnetics*, **vol. 32**, pp.535-546, 1996.

[8] Bragg, L. R. and Dettman, J. W., "Related Partial Differential Equations and Their Applications", *SIAM J. Appl. Math.*, **vol. 16**, pp.459-467, 1968.

[9] Bragg, L. R. and Dettman, J. W., "Related Problems in Partial Differential Equations", *Bulletin of America Society of Mathematics*, **vol. 74**, pp.375-378, 1968.

[10] Romanov, V. G., *Inverse problems of mathematical physics*, translated by Yuzina, L. Ya., Utrecht, The Netherlands: VNU Science Press BV, 1987.

[11] Lee, K. H., Xie, G., Habashy, T. M. and Torres-Verdin, C., "Wave Field Transform of Electromagnetic Fields", presented in *64th Ann. Internat. Mtg., Soc. Expl. Geophys.*, Expanded Abstracts, pp633-635, 1994.

[12] Bragg, L. R. and Dettman, J. W., "An Operator Calculus for Related Partial Differential Equations", *J. Math. Analysis and Applic.*, **vol. 22**, pp.261-271, 1968.

[13] Bragg, L. R. and Dettman, J. W., "A Class of Related Dirichlet and Initial Value Problems", *Proc. Amer. Math. Soc.*, **vol. 21**, pp.50-56, 1969.

[14] Reznitskaya, K. G., "The Connection Between Solutions of the Cauchy Problem for Equation of Different Types and Inverse Problems", *Mat. Problemy Geofiz. Vyp.*, **vol. 5**, Part 1, pp.55-62, 1974. (in Russian)

[15] Lavrent'ev, M. M., Romanov, V. G. and Shishatskii, S. P., *Ill-Posed Problems of Mathematical Physics and Analysis*, America Mathematical Society, Providence, RI, 1986. (translated)

[16] Sun, K., Udpa, S., Udpa, L., Xue, T., and Lord, W., "Registration Issue in the Fusion of Eddy Current and Ultrasound NDE Data Using Q-transform", in *Review of Progress in Quantitative Nondestructive Evaluation*, Edited by Thompson, D. O. and Chimenti, D. E., New York: Plenum Press, **vol. 15**, pp.813-820, 1996.

[17] Hildebrand, B. P. and Fitzpatrick, G. L., "Inversion of Eddy Current Data Using Holographic Principles", in *Review of Progress in Quantitative Nondestructive Evaluation*, Edited by Thompson, D. O. and Chimenti, D. E., New York: Plenum Press, **vol. 4**, pp.507-515, 1984.

[18] Bohbot, R. de. O., Lesselier, D. and Duchene, B., "A Diffraction Tomograohic Algorithm for Eddy Current Imaging from Anomalous Fields as Fictitious Imaginary Frequencies", *Inverse Problems*, **vol. 10**, pp109-127, 1994.

[19] Devaney, A. J., "Linearised Inverse Scattering in Attenuating Media", *Inverse Problem*, **vol. 3**, pp389-397, 1987.

[20] Zorgati, R., Duchene, B., Lesselier D. and Pons, F., "Eddy Current Testing of Anomalies in Conductive Materials, Part I: Qualitative Imaging via Diffraction Tomography Techniques", *IEEE Transactions on Magnetics*, **vol. 27**, pp.4416-4437, 1991.

[21] Zorgati, R., Lesselier D., Duchene, B. and Pons, F., "Eddy Current Testing of Anomalies in Conductive Materials, Part II: Qualitative Imaging via Deterministic and Scochastic Inversion Techniques", *IEEE Transactions on Magnetics*, **vol. 28**, pp.1850-1862, 1992.

[22] Pierce, A., "Wave Methods for an Inverse Problem in Diffusion", *Inverse Problem*, **vol. 2**, pp.205-217, 1986.

[23] Kunetz, G., "Processing and Interpretation of Magnetotelluric Soundings", *Geophysics*, **vol. 37**, pp.1005-1021, 1972.

[24] Levy, S., Oldenburg, D., and Wang, J., "Subsurface Imaging Using Magnetotelluric Data", *Geophysics*, **vol. 53**, pp.104-117, 1988.

[25] McWhirter, J. G. and Pike, E. R., "On the Numerical Inversion of the Laplace Transform and Similar Fredholm Integral Equations of the First Kind", *Journal of Physics A*, **vol. 11**, pp.1729-1745, 1978.

[26] Gibert, D., Tournerie, B. and Virieux, J., "High-resolution Electromagnetic Imaging of the Conductive Earth Interior", *Inverse Problems*, **vol. 10**, pp.341-351, 1994.

[27] Gershenson, M. "Simple Interpretation of Time Domain Electromagnetic Sounding Using Similarities Between Wave and Diffusion Propagation", *93 SEG Annual Convention Extended Abstract*, pp.1342-1345, 1993, SS2.34.

[28] Gershenson, M., "Simple Interpretation of Time Domain Electromagnetic Sounding Using Similarities Between Wave and Diffusion Propagation", *Geophysics*, **vol. 62**, pp.763-774, 1997.

[29] Das, K., Becker, A. and Lee, K. H., "Experimental Validation of the Wavefield Transform of Electromagnetic Fields", *Geophysical Prospecting*, **vol. 50**, pp.441-451, 2002.

[30] Levy, S. and Fullagar, P. K., "Reconstruction of a Sparse Spike Train from a Portion of its Spectrum and Application to High-Resolution Deconvolution", *Geophysics*, **vol. 46**, pp.1235-1243, 1981.

[31] Lee, T. J., Suh, J. H., Kim, H. J., Song, Y. and Lee, K. H., "Electromagnetic Traveltime Tomography Using an Approximate Wavefield Transform", *Geophysics*, **vol. 67**, pp.68-76, 2002.

[32] Tamburrino, A., Udpa, S. S., "On the Q-transform for Solving Inverse Problems for the Diffusion Equation", Internal Report, Department of Electrical and Computer Engineering, Michigan State University, 2001.

[33] Tamburrino, A. and Udpa, S. S., "Solution of Inverse Problems for Scalar Parabolic Equations Using a Hyperbolic to Parabolic Transformation: Time-of-Flight Analysis", submitted for publish.

[34] Tian, Y., Tamburrino, A., Udpa, S. S. and Udpa, L., "Time-of-Flight Measurements from Eddy Current Tests", in *Review of Progress in Quantitative Nondestructive Evaluation*, Edited by Thompson, D. O. and Chimenti, D. E., New York: Plenum Press, **vol. 22**, pp.593-600, 2002.

[35] Tamburrino, A., Fresa, R., Udpa, S. S. and Tian, Y., "Three-Dimensional Defect Localization from Time-of-Flight/Eddy Current Testing Data", *IEEE Trans. on Magnetics*, **vol. 40**, pp.1148-1151, March 2004.

[36] Tamburrino, A., "TOF in the Presence of Material Interfaces: A Scalar Axisymmetric Geometry", Internal Report, Department of Electrical and Computer Engineering, Michigan State University, 2003.

[37] Tamburrino, A., Tian, Y. and Udpa, S. S., "Eddy Current Testing of Conductive Materials Using Time-of-Flight Measurements", in E'NDE, Electromagnetic Non-Destructive Evaluation (VIII), T. Sollier et al. (Eds.), pp. 104-111, IOS Press, 2004.

[38] Haus, Hermann A, Melcher, James R., *Electromagnetic Fields and Energy*, New Jersey: Prentice Hall, 1989.

[39] Jin, Jianming, *The Finite Element Method in Electromagnetics*, New York: Wiley, 2002.

[40] Demarest, K. R., *Engineering Electromagnetics*, New Jersey: Prentice Hall, 1998.

[41] Guru, B. S. and Hiziroglu, H. R., *Electromagnetic Field Theory Fundamentals*, Boston: PWS Publishing, 1998.

[42] Ida, N. and Bastos, J. P. A., *Electromagnetics and Calculation of Fields*, New York: Springer, 1997.

[43] Csendes, Z. J., Weiss, J. and Hoole, S. R. H., "Alternative Vector Potential Formulations of 3-D Magnetostatic Field Problems", *IEEE Trans. on Magnetics*, **vol. MAG-18**, pp.367-372, 1982.

[44] Biro, O., Preis, K. and Richter, K. R., "Various FEM Formulations for the Calculations of Transient 3D Eddy Currents in Nonlinear Media", *IEEE Trans. on Magnetics*, **vol. 31**, pp.1307-1312, 1995.

[45] Biro, O. and Preis, K., "On the Use of the Magnetic Vector Potential in the Finite Element Analysis of 3-D Eddy Currents", *IEEE Trans. on Magnetics*, **vol. 25**, pp.3145-3159, 1989.

[46] Bryant, C. F., Emson, C. R. I. and Trowbridge, C. W., "A Comparison of Lorentz Gauge Formulations in Eddy Current Computations", *IEEE Trans. on Magnetics*, **vol. 26**, pp.430-433, 1990.

[47] Morisue, T., "A New Formulation of the Magnetic Vector Potential Method in 3-D Multiply Connected Regions", *IEEE Trans. on Magnetics*, **vol. 24**, pp.110-113, 1988.

[48] Morisue, T., "Magnetic Vector Potential and Electric Scalar Potential in Three-Dimensional Eddy Current Problems", *IEEE Trans. on Magnetics*, **vol. MAG-18**, pp.531-535, 1982.

[49] George, A. and Liu, J., *Computer Solution of Large Sparse Definite Systems*, New Jersey: Prentice Hall, 1981.

[50] Kraus, J. D. and Fleisch, D. A., *Electromagnetics with Applications*, New York: McGraw-Hill, 1999.

[51] Zhou, Pei-bai, *Numerical Analysis of Electromagnetic Fields*, Berlin, Germany: Springer-Verlag, 1993.

[52] Li, Y., *Edge Based Finite Element Simulation Of Eddy Current Phenomenon and its Application to 3D Defect Characterization*, Ph'D thesis, Iowa State University, 2002.

[53] Wait, R. and Mitchell, A. R., *Finite Element Analysis and Applications*, New York: John Wiley & Sons, 1985.

[54] Abramowitz, M. and Stegun, I. A. (Eds.), *Handbook of Mathematical Functions with Formulas, Graphs, and Mathematical Tables*, 9^{th} printing. New York: Dover, 1972.

[55] Tikhonov, A. N., *Solutions of Ill-Posed Problems*, New York: Wiley, 1977.

[56] Corless, R. M., Gonnet, G. H., Harc, D. E. G., Jeffrey, D. J. and Knuth, D. E., "On the Lambert W Function", *Advances in Computational Mathematics*, **vol. 5**, pp.329-359, 1996.

[57] Richmond, J. H., "Scattering by a Dielectric Cylinder of Arbitrary Cross Section Shape", *IEEE Trans. on Antennas and Propagation*, **vol. 13**, pp.334-341, 1965.

[58] Harrington, R. F., *Time-Harmonic Electromagnetic Fields*, New Jersey: IEEE Press, 2001.

[59] Kishk, A. A., Parrikar, R. P. and Elsherbeni, A. Z., "Electromagnetic Scattering from an Eccentric Multilayered Circular Cylinder", *IEEE Trans. on Antennas and Propagation*, **vol. 40**, pp.295-303, 1992.

[60] Schwart, L., *Mathematics for the Physical Sciences*, Paris: Hermann, 1966.

[61] Parrikar, R. P., Kishk, A. A. and Elsherbeni, A. Z., "Scattering from an Impedance Cylinder Embedded in a Nonconcentric Dielectric Cylinder", *IEE Proceedings-H*, **vol. 138**, pp169-172, 1991.

[62] Tamburrino, A. and Nair, N., "Interface removal algorithm for a planar problem", Private communication, 2005.